A Total Cross Section and Y Distribution Measurement for Muon Type Neutrinos and Antineutrinos on Iron

Thesis by

Robert Eugene Blair

In Partial Fulfillment of the Requirements

for the Degree of

Doctor of Philosophy

California Institute of Technology

Pasadena, California

1982

(Submitted April 1, 1982)

Acknowledgments

The measurements described here would have been impossible without the help of a number of people. In particular I want to thank Taka Kondo, Kieth Jenkins, Dave MacFarlane, Milind Purohit and Petros Rapidis for assistance in the data analysis, Bob Messner and Mike Shaevitz for guidance, and Frank Sciulli for help in understanding and doing just about everything. I want to thank Tere, my wife, for aid in assembling the graphics for the thesis and for typing help. Also, I want to thank Stuart Stampke who, despite the fact that he was struggling to get his own thesis done, took time out to act as my surrogate at Caltech while I was in New York. I owe a great deal to numerous members of the Caltech and Fermi National Laboratory staff who have done most of the real work necessary to perform our experiment.

Abstract

The measurement of the total charged current cross section for neutrinos and antineutrinos on iron is described. The data consist of 55,000 neutrino and 17,000 antinuetrino events taken in the N30 Dichromatic train at Fermi National Laboratory. The events cover the energy range 30-230 GeV. The slope of the cross section is consistent with flat over this energy range but favors a rise with energy. The results of fits to the y distribution of the form $\beta((1-\alpha)+\alpha(1-y)^2-\frac{Ry^2}{2(1+R)})$ for neutrinos and $\beta((1-\alpha)(1-y)^2+\alpha-\frac{Ry^2}{2(1+R)})$ for antineutrinos (with $R=.1$) are reported. A comparison is made between the measured cross sections and the level of $e\ d$ and $\mu\ Fe$ scattering cross sections. The effect of a W propagator, QCD and neutrino oscillations on the cross section is described. The level of effects allowed by the data for oscillations and a propagator are estimated.

Table of Contents

1. Introduction 1

1.1 Very Brief History of Neutrino Physics

1.2 Experiments by the CFRR Collaboration

1.3 E616

Comparison of E616 with Other Recent Neutrino Experiments

2. Beam 7

2.1 Principles of the Dichromatic Neutrino Beam

2.2 FNAL Layout

Fermilab Neutrino Area

Secondary Beam Properties

2.3 Total Secondary Flux Measurement

Secondary and Primary Monitors

Ion Chamber Calibration

2.4 Cherenkov Counter Pressure Curves

Background Subtraction

Alignment Correction

Electron and Muon Content of the Beam

Particle Fractions

Evaluation of the Gas Constant

Average Momentum

3. Lab E Apparatus. 45

3.1 Target Statistics and Layout

3.2 Spark Chambers

Muon Momentum Resolution

3.3 Scintillation Counters

Analog Information Recorded

Counter Maps

Hadron Energy Calibration and Resolution

3.4 Trigger electronics

Muon Trigger

Penetration Trigger

4. Event and Monitor Analysis. 66

4.1 Cuts on Events

Unanalyzable Events

Events with Improper Track Reconstruction

Scan Results

4.2 Monitor Cuts (applied to monitors and events)

4.3 Ion Chamber Selection

5. Expectations Versus Results. 72

5.1 Cross Sections

Method of Event Counting

5.2 Y Distributions

Method of Construction

Differential Cross Section at y=0

Average y

5.3 The Standard Theory and Beyond

The Quark Parton Model and Scaling

QCD and Deviations from Exact Scaling

Limits on the W Boson Mass

Comparison with Electron and Muon Scattering

Neutrino Oscillations

Appendix 1: The Evaluation of Measurement Errors. 120

Bibliography. 142

1. Introduction

1.1. Very Brief History of Neutrino Physics

Since 1931 when Pauli first postulated the existence of a neutral particle emitted in beta decay, our picture of the neutrino and the weak interactions has come more clearly into focus. Pauli was motivated by the fact that the beta particles produced in nuclear decays were not monoenergetic, as they would be if beta decay were a two body decay ($z \rightarrow z \pm 1, e^{\mp}$). He recognized that a third particle must be produced to save energy, momentum conservation.

Two years later a quantitative description of the weak interaction was put forward by Fermi [FE34]. Fermi's theory closely paralleled the theory of quantum electrodynamics (Q.E.D.). The concept of current was generalized to include the change of particle identity characteristic of beta decay ($e \rightarrow \nu, p \rightarrow n$). The interaction was made pointlike by letting the "weak" potential act at a point rather than falling off as $\frac{1}{r}$ like the Coulomb potential. For the processes to be covered in this thesis; $\nu + N \rightarrow \mu + anything$, this theory, modified to include parity violation (see below), is indistinguishable experimentally from the modern weak interaction theory. These processes are termed charged current (CC) neutrino interactions.

In 1956 the first CC interaction was observed [RE59]. The source of neutrinos (actually antineutrinos) was a reactor at Savannah River. For the first time, the inverse of the beta decay process was observed in which an antineutrino was absorbed by a nucleus with the subsequent emission of a positron. This confirmed the existence of the neutrino through "direct" observation. In 1957 a long cherished assumption about the weak interaction was questioned and found to be incorrect. Lee and Yang proposed that parity might be violated in weak processes [LE56]. It was subsequently found experimentally by C.S. Wu and

others that weak beta decays did violate parity [WU57]. This established the mysterious connection between an internal quantum number (lepton number) and a space time symmetry (helicity) which remains unexplained today. The neutrino has helicity -1 and lepton number 1; the antineutrino has helicity 1 and lepton number -1. The modifications in the theory required by the observation of parity violation were made by Gell-Mann and Feynman in 1958 [FE58].

No major changes occurred in the theory until about a decade later. Experimental verification of lepton number conservation was carried out in 1960 and the first accelerator neutrino experiment was performed at Brookhaven in 1962. The relationship between strangeness and the weak force was clarified in 1963 by Cabibbo. The big step forward occurred in 1967 when Salam and Weinberg put forward a theory which managed to avoid the problem of nonrenormalizability inherent in the Gell-Mann, Feynman theory [WE67]. The new theory was unique in that it intertwined the weak and electromagnetic forces. It did not unify the two forces, in the sense that they both stemmed from one underlying force with a single coupling strength. It described them as a commingling of two independent forces, which after spontaneous symmetry breaking become inextricably combined to form a new pair of interactions, the weak and electromagnetic forces. Glashow, Illiopolus and Maini later showed how, with the addition of a new quark (the c quark), this theory could avoid disagreement with experimental limits on strangeness changing neutral currents [GL70]. The $SU_L(2)xU(1)$ gauge theory of weak interactions proved successful in hinting at two major experimental events, the discovery of neutral currents in 1973 and of the ψ in 1974 [HA73,BE74,AU74a-b]. For measurements described here, there is no observable difference between the $SU_L(2)xU(1)$ theory and that proposed by Gell-Mann and Feynman in 1958. The neutral current phenomena, however, were very successfully parameterized by the one free parameter, $\sin^2\Theta_w$, in the

Salam, Weinberg theory.

As the picture of the weak interaction became more consistent experimentally and theoretically, the emphasis in many neutrino experiments shifted from testing the weak interaction theory to using neutrinos as a probe for investigating nucleon structure. This trend may be reversing; recent results from a reactor experiment by Reines [RE80] and an "end-point" experiment by Lubimov [LU80] have renewed interest in the question of neutrino mass. Does the neutrino have a small, heretofore unmeasured, rest mass? Many experiments are running and being built to address this issue.

1.2. Experiments by the CFRR collaboration

Since before Fermilab started accelerating protons, the Caltech, Fermilab, Rockefeller (CITFR) collaboration has been involved in the neutrino program there. From 1971 to 1975 the CITFR collaboration measured total charged and neutral current cross sections, dimuon production and the low y charged current cross section [BA75a-b,BA76,BA77a-d,BA78,ME78]. These measurements were performed with a detector built in the "Wonder" building.

In 1975, work was started on an upgrade. Rochester U. was added to the list of collaborators (CFRR). A new detector was built in Lab E (about 400 m. downstream of the "Wonder" building). The new detector has a larger tonnage and better track measuring capabilities. Improvements were also made in beam monitoring and the train. In the summer of 1978, an engineering run was done to check out the newly commissioned train and detector. The data from that run consisted of about 6500 events taken mostly at the highest available energy setting, 300 GeV. These data were analyzed to yield total charged current cross sections and differential cross sections with respect to x and y [LE81].

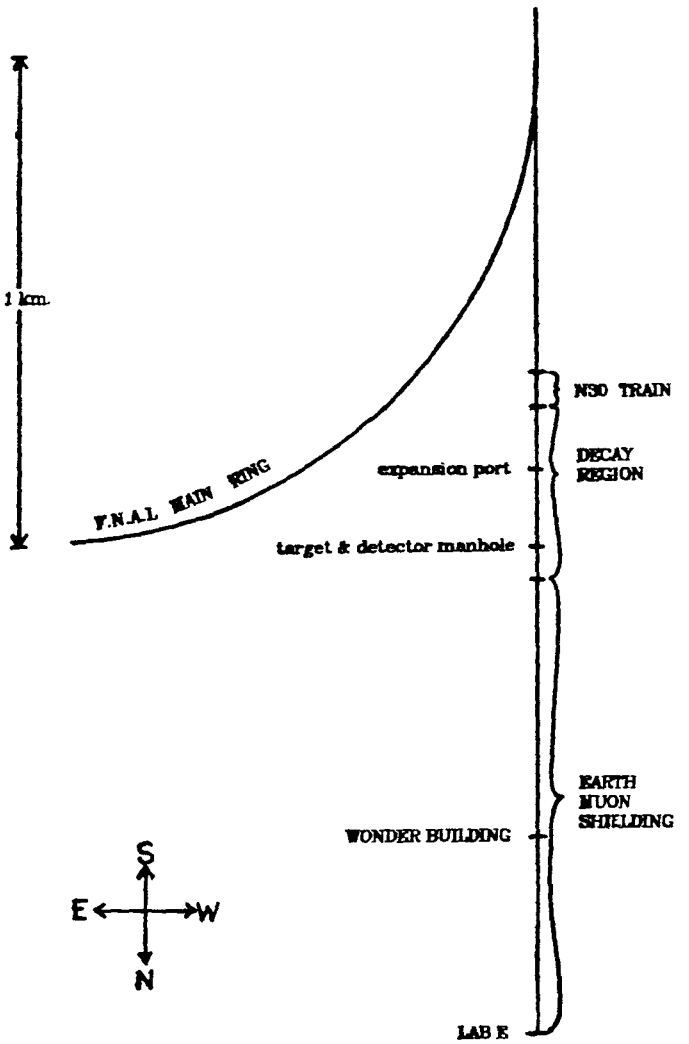

Figure 1-1: Fermi National Laboratory neutrino area, showing the relative locations of:
a) The N30 train for collimating and momentum selecting pions and kaons for the dichromatic neutrino beam
b) The decay region that provides an evacuated flight path allowing some pions and kaons to decay yielding neutrinos.
c) Lab E (location of this experiment's neutrino detector) and the Wonder building (where an earlier neutrino experiment was performed by this group)

1.3. E 616

After the engineering run, needed improvements were made to the dichromatic train and minor improvements were made to the beam monitor and detector. The data analyzed for this thesis were taken in continuous running from June 1979, to January 1980. During this period, we collected over 100,000 neutrino events and over 20,000 antineutrino events. The analysis discussed here will include only about one-half to one-third of the complete data set (restrictions on the fiducial volume and elimination of slow spill data account for the rest). The event total for this analysis is 55,000 neutrino and 17,000 antineutrino events. Table 1-1 summarizes some of the vital statistics for a number of recent neutrino experiments. It should be pointed out at the start that our group has made a major investment in running with the dichromatic train. The dichromatic beam, while compromising some on neutrino flux, allows direct observation of the number and energy of secondary pions and kaons. This advantage makes dichromatic running far superior to other types of neutrino beams for normalized measurements.

This thesis will include results from the first step of the analysis effort on these data. No discussion will be included of the x dependence of the structure functions. These results remain for the next generation of graduate students.

Table 1-1: Recent neutrino experiments

Ref.	Group	Beam*	No. Events	Target	E_ν
	CFRR (E616)	NBB	150k ν 23k $\bar{\nu}$	Fe electronic	30-230GeV.
LE81	CFRR (E356)	NBB	6.5k ν	Fe electronic	30-260GeV.
BA77	CFR (E21)	NBB	18k ν 12k $\bar{\nu}$	Fe electronic	45-205GeV.
AL80 BO77	BEBC	NBB WBB	517 ν 250 $\bar{\nu}$ 580 ν 2.3k $\bar{\nu}$	NeH_2 bubble ch. D_2 bubble ch.	20-200GeV. 10-200GeV.
MO81	GGM (SPS)	WBB	3k ν 3.8k $\bar{\nu}$	C_3H_8 bubble ch.	15-150GeV.
JO80	CHARM	NBB	9.2k ν 3.8k $\bar{\nu}$	Marble electronic	20-200GeV.
EI81	CDHS	NBB WBB	105k ν 25k $\bar{\nu}$ 60k ν 150k $\bar{\nu}$	Fe electronic	20-200GeV. 20-200GeV.

*NBB: narrow band or dichromatic / WBB: wideband beam

2. Beam

2.1. Principles of the Dichromatic Neutrino Beam

The dichromatic neutrino beam is a concept pioneered by Frank Sciulli, Vince Peterson, and others for the early Fermilab experiment, E21 [SC70,PE64]. By momentum selecting and collimating the neutrino parents, pions and kaons, it is possible to obtain a beam of neutrinos whose energy is related to where the neutrino strikes the target; this is the result of two body decay kinematics. If a parent particle of four momentum $\vec{P}_0$ and mass M_0 decays into a massless neutrino with four momentum $\vec{P}^{\nu}$ and a muon with four momentum $\vec{P}^{\mu}$ with mass μ we have:

$$\vec{P}_0 = \vec{P}^{\nu} + \vec{P}^{\mu}$$

$$M_0^2 - 2\vec{P}_0 \cdot \vec{P}^{\nu} = \mu^2$$

$$\frac{(M_0^2 - \mu^2)}{2E^{\nu}} \approx P_0\left(1 - \cos\Theta_{\nu} + \frac{\mu^2}{2P_0^2}\right)$$

$$E^{\nu} \approx (M_0^2 - \mu^2) \frac{1}{P_0\left(\Theta_{\nu}^2 + \frac{M_0^2}{P_0^2}\right)}$$

$$E^{\nu} \approx \frac{\alpha}{\frac{R^2}{L^2} + \frac{M_0^2}{P_0^2}}$$

$$\alpha \equiv \frac{(M_0^2 - \mu^2)}{P_0}$$

where R = radius of neutrinos at target

L = distance from decay to target

P_0 = momentum of the decaying particle

The type of neutrino beam (with momentum selected parent particles) is called dichromatic because a sign and momentum selected beam contains both pions

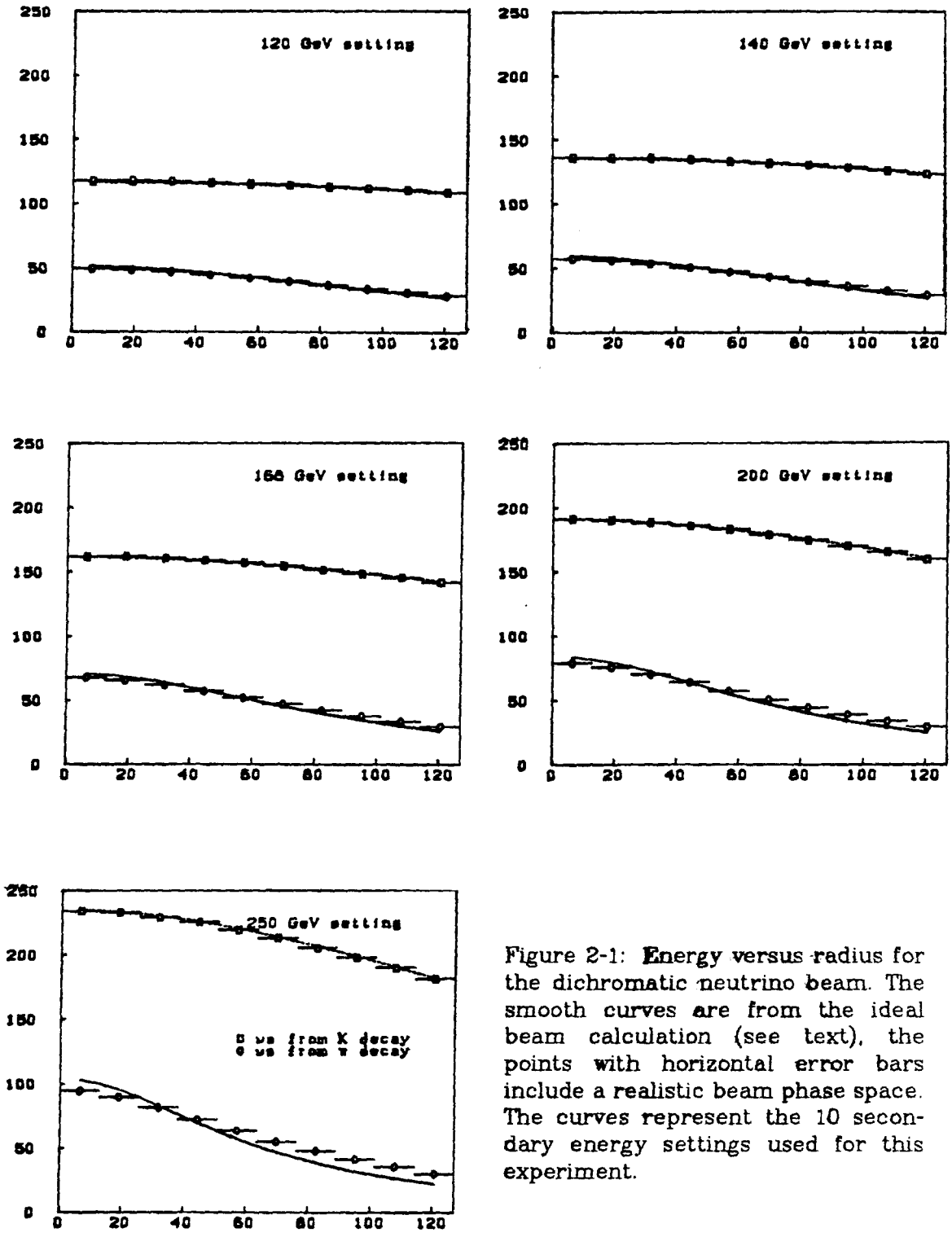

Figure 2-1: Energy versus radius for the dichromatic neutrino beam. The smooth curves are from the ideal beam calculation (see text), the points with horizontal error bars include a realistic beam phase space. The curves represent the 10 secondary energy settings used for this experiment.

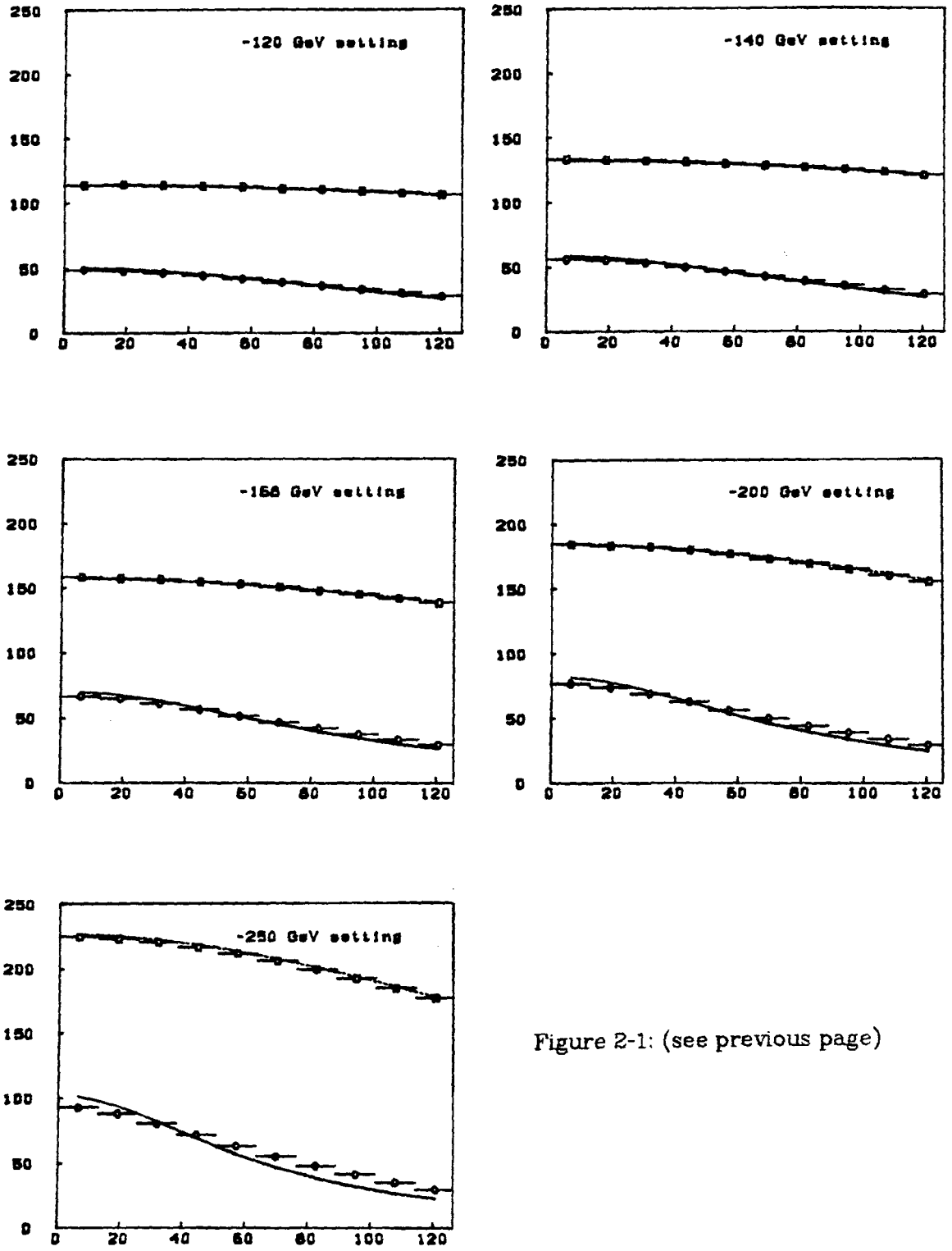

Figure 2-1: (see previous page)

and kaons, each of which produce neutrinos of different energies via two body decays. In any real dichromatic beam the parents will not be monoenergetic nor will they be perfectly collimated. To see how much of an effect these have on the energy versus radius relation, see figure 2-1 where a comparison is made between the above formula and a Monte Carlo calculation including these effects. For neutrinos from kaon decay the deviations from an ideal beam are extremely small; for neutrinos from pion decay deviations become significant at high energies where the value of $\frac{M_0}{P_0}$ becomes comparable to typical pion angles in the decay pipe.

The parent particles for a dichromatic beam are produced as secondaries from high energy proton interactions on some convenient production target. The production target acts as a focus for a point to parallel "optics" system. The secondaries produced in a small spatial region with a large angular spread are brought to nearly parallel in a larger spatial region by a set of magnets which are analogous to a simple lens used to collimate a point source of light in optics. The "train", as this set of magnets is called, also serves to select particles around some central momentum much as in optics we might use dispersion to select out a color band from white light. A simple optical model of the dichromatic train is shown in figure 2-2. In this figure the x and y views are shown separately since with magnets the focusing function is performed by quadrupoles which focus in one view and defocus in the other.

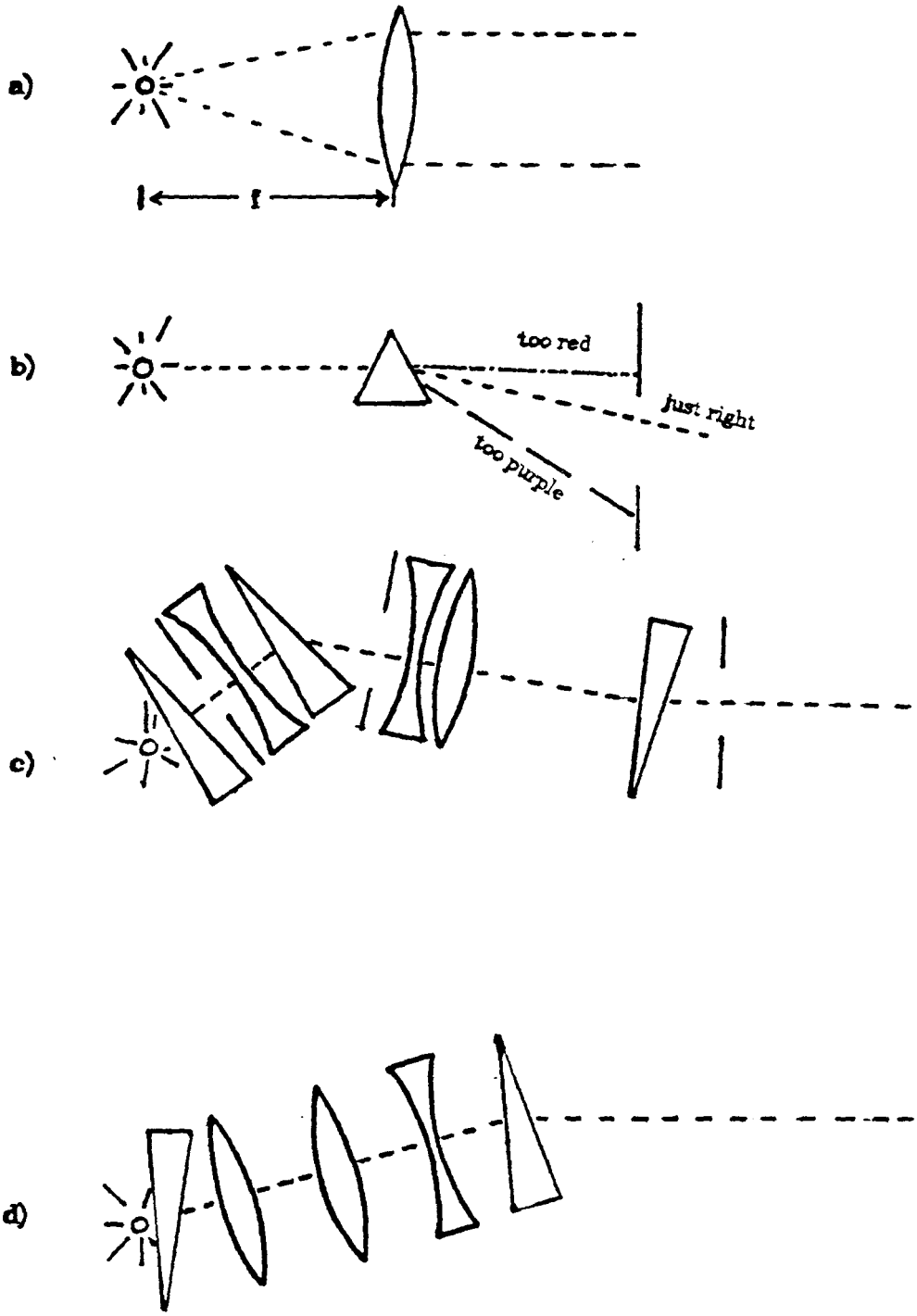

Figure 2-2 : A simplified optical model of the N30 dichromatic train. A point source of white light produces collimated light of a particular color after passing through a system of lenses, prisms and slits.
a) The simplest possible collimator.
b) A very simple system to pick out a color band.
c & d) Horizontal and vertical analogues of the N30 train.

2.2. FNAL Layout

This experiment used the Fermilab N30 dichromatic train (see figure 2-3). Secondaries were produced by interactions of 400 GeV protons on a BeO target 12 inches long.

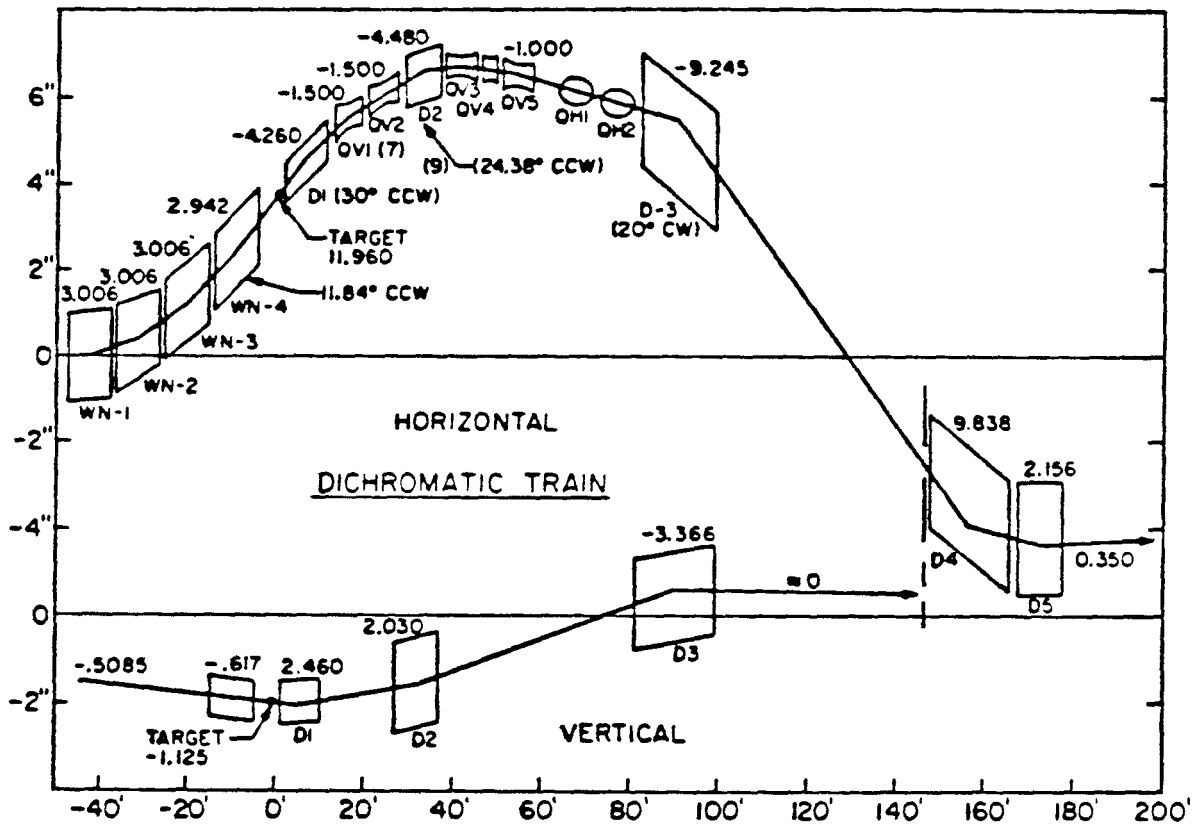

Figure 2-3: The N30 dichromatic train. The beam elements are depicted along with the central ray trajectory. Note the difference in horizontal and vertical scales.

Secondaries collimated by the train passed down a 350 meter long evacuated pipe to allow the pions and kaons to decay. At the end of the decay pipe there is a 20 foot steel and aluminum dump to stop the secondaries. The neutrino target is situated 930 meters from the end of the decay pipe and the intervening region is filled with steel and earth shielding to stop muons produced by the secondary decays.

2.3.Secondary Beam Properties

In order to obtain neutrino and antineutrino events uniformly in energy the dichromatic train was set to five different momenta for positive secondaries and negative secondaries. Evaluating the flux of neutrinos for each setting required knowledge of the mean secondary momentum, momentum spread and angular dispersion for each setting. Information about the angular spread comes from two segmented wire ion chambers (SWICs) positioned 154 meters apart in the decay pipe. The SWICs yielded x and y projections of the beam, which could be used to estimate the angular spread of the secondary beam (see appendix 1). The momentum and momentum spread were evaluated using the Cherenkov pressure curves (see sec 2.5). The mean momentum can also be estimated by observing the the total energy of the neutrinos from neutrino interactions in the Lab E detector. These measurements were redundant with a Monte Carlo calculation in which secondaries were traced through the train. The level of agreement between the Monte Carlo calculation and the measured quantities served to give us an idea of how well we understood the secondary beam. A summary of the beam properties appears in table 2-1 and a survey of how these properties were determined and what errors we can put on these values is given in Appendix 1.

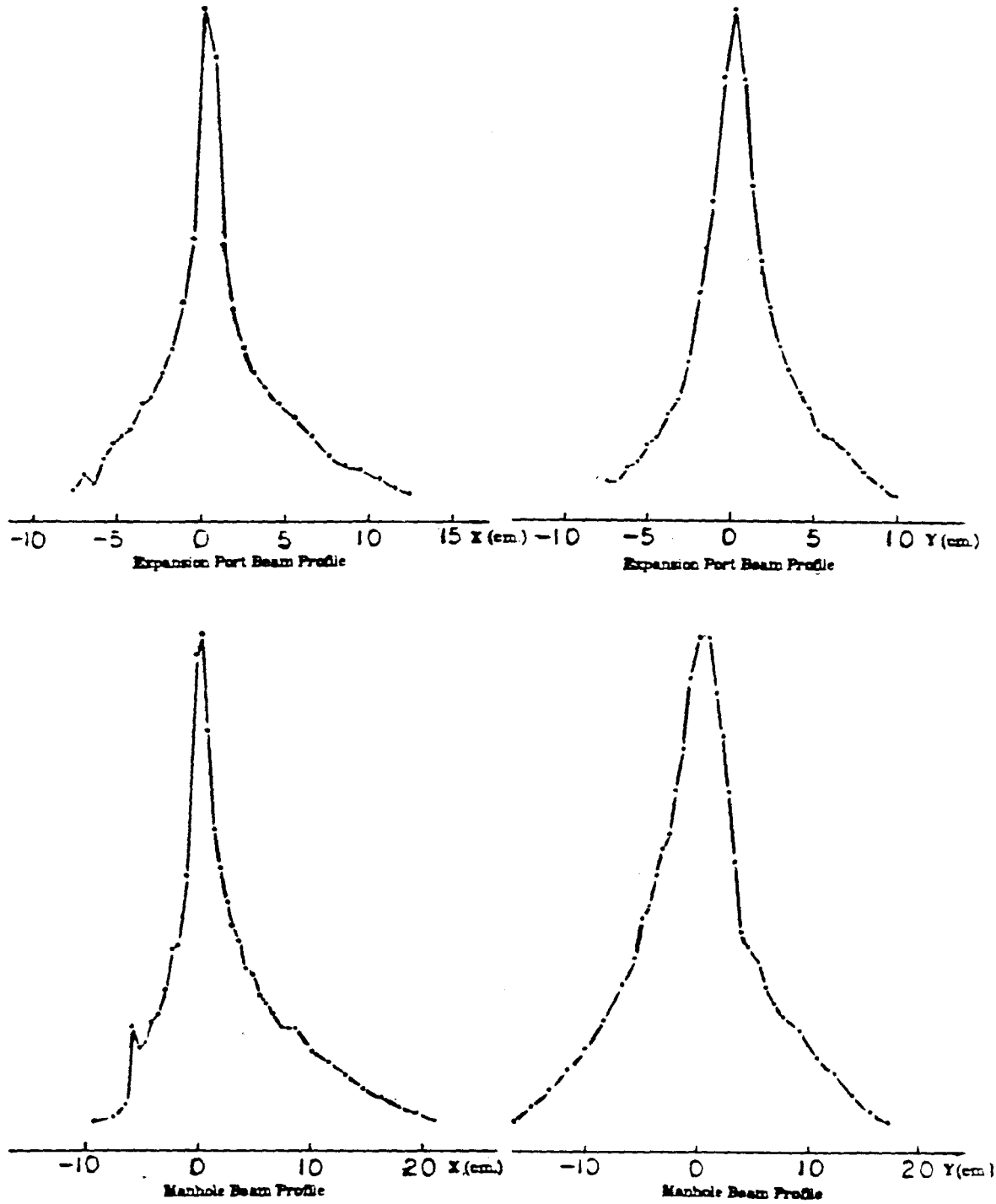

Figure 2-4:SWIC profiles. An example of the beam profiles obtained from the SWICs. These profiles were recorded while taking antineutrino data at 250 GeV.

Table 2-1: Secondary Beam Properties

Nominal Setting	Mean P_π	Mean P_k	R.M.S. Θ_x	R.M.S. Θ_y	$\frac{\sigma_p}{p}$
120	119.5GeV./c	122.4GeV./c	.16mr.	.23mr.	10.1%
-120	118.4 "	119.6 "	"	"	9.7%
140	139.2 "	142.2 "	.15mr.	.21mr.	9.9%
-140	137.8 "	138.9 "	"	"	9.4%
168	166.3 "	169.8 "	.13mr.	.20mr.	10.0%
-168	164.3 "	165.3 "	"	"	9.5%
200	197.0"	200.6"	.15mr.	.20mr.	9.6%
-200	194.0 "	194.6 "	"	"	9.2%
250	243.8 "	247.0 "	.16mr.	.20mr.	9.4%
-250	239.0 "	238.0 "	"	"	8.7%

2.4. Total Secondary Flux Measurement

The total number of protons on target was monitored by a toroid in front of the production target. The total number of secondary particles that pass down the decay pipe was measured by two ion chambers (one at the expansion port and another at the target manhole), see figure 2-5. In addition, when the Cherenkov counter was not in the beam an R.F.(radio frequency) cavity acted as a third beam monitor (the R.F. cavity and the Cherenkov counter rested on a movable table which allowed either to be in the beam, see figure 2-6). The ion chambers are simple reliable beam monitors and they served as the main monitors of beam intensity. Unfortunately, there is no reliable direct method of

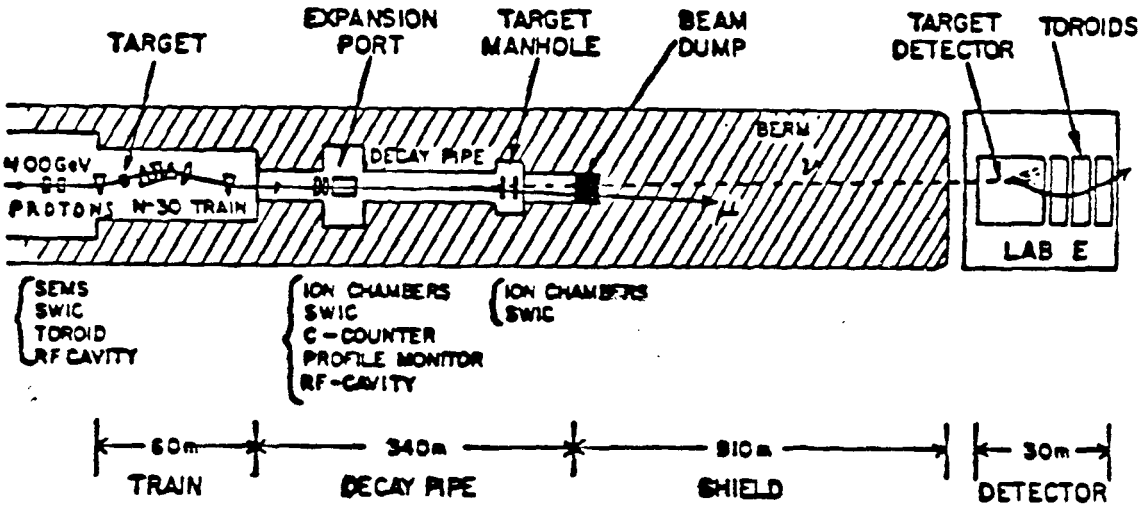

Figure 2-5: Layout of the neutrino beam line, including monitor locations. Note that this drawing is not to scale.

calibrating the ion chambers. It was necessary, in order to determine what their output was per incident particle, to compare them with other beam monitors to obtain a calibration. This was done on several occasions and with a number of different monitors and beams.

In the course of measuring the ion chamber response we found that the output of the chamber also depended on the beam composition. Interactions in the windows of the ion chamber (the electrodes) produce additional ionization in the ion chamber gas as a result of the production of low energy heavily ionizing particles (protons and alpha's). The amount of this additional ionization depends on the absorption cross section of the particles going through the chamber (40 mb for protons and 24 mb for pions and kaons). Using emulsion data to indicate how many slow collision products there are, this effect can be estimated to yield about a 5.5% difference between the ionization produced by pions and protons. When we average all of the ionization chamber calibration techniques together, we find the corresponding difference to be 4.5%.

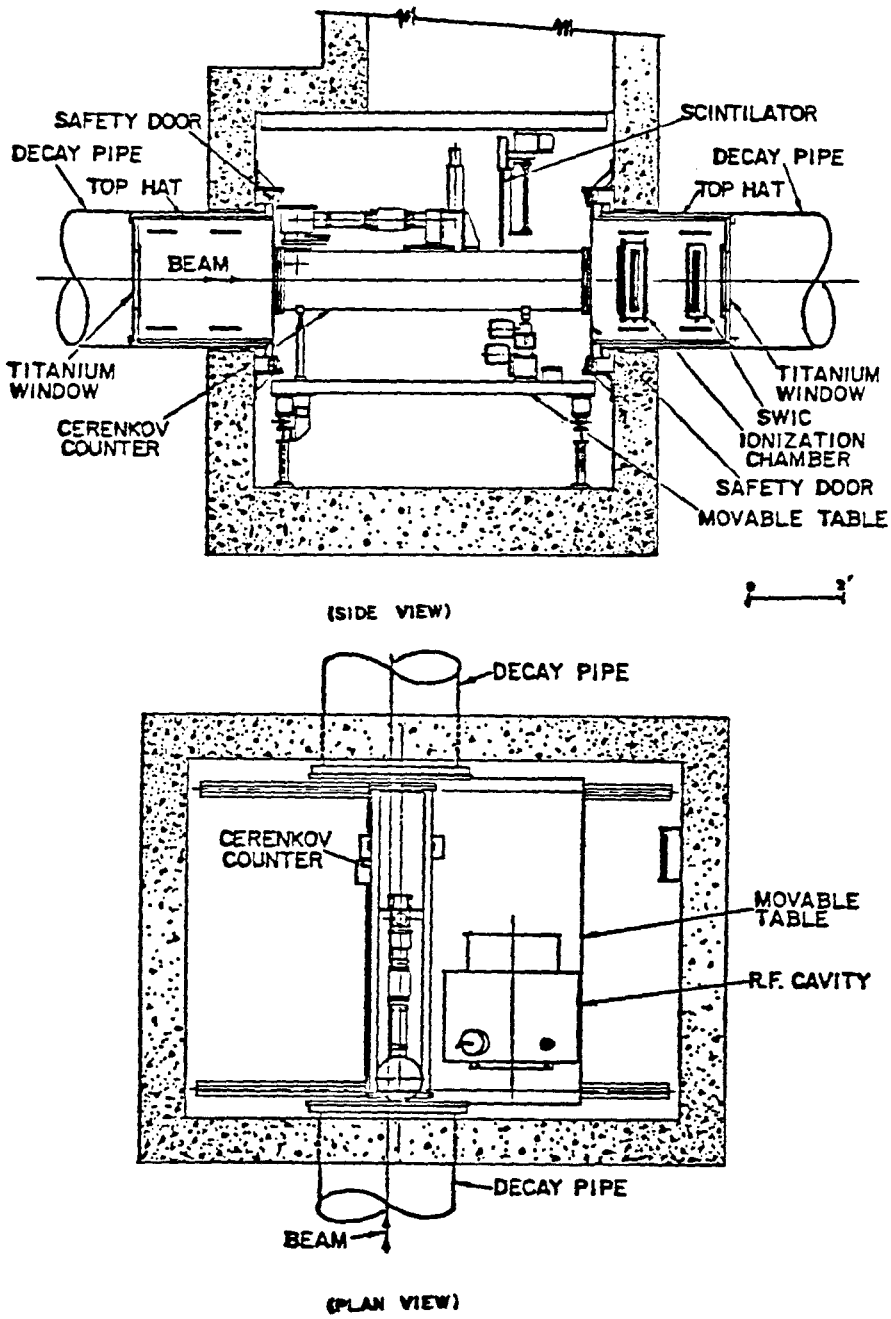

Figure 2-6: Beam monitors in the expansion port.

The R.F. cavity, which was in the beam during much of the running, exploits the fact that the beam is bunched in "R.F. buckets" of about 4 ns. in duration separated by 18.2 ns. This temporal structure results from the fact that the proton beam is accelerated with R.F. cavities and becomes synchronized and tightly bunched. The R.F. cavity used as a monitor is tuned to the same frequency as the accelerating cavities and its output is proportional to the electric field strength across its gap at that frequency. As a result the output is proportional to the number of beam particles that pass through it.

The R.F. cavity provided one calibration of the ion chamber. The proportionality constant relating R.F. cavity output to number of particles can be calculated given the cavity properties (resonant frequency, Q, and geometry of the cavity). We can then compare the output of the ion chamber in pico Coulombs to the output of the R.F. cavity stated in particles. The overall accuracy of this method is about 5% but it has the advantage that it is done in the dichromatic beam while taking neutrino data. Fitting the data with various meson and proton contents yields a value for the ion chamber response as $3.47\pm.17x10^{-18}\frac{Coulombs}{particle}$ mesons and $3.76\pm.22x10^{-18}\frac{Coulombs}{particle}$ for protons.

Another method used to calibrate the ion chamber was to bring main ring protons through the train and use foil irradiation to determine the relative intensity before and after the train. In this way the $N0$ toroid which measured the number of protons before the train could be used to establish beam intensity and the foils could determine the train transmission. This calibrates the ion chamber against the toroid, whose response was measured using a current loop which passed a test current through the toroid. In addition the foil after the train could act as an absolute monitor in the sense that other groups have measured the cross section for production of ^{24}Na in a copper foil. Using the foils to measure transmission we get an ion chamber response of $3.45\pm.22x10^{-18}$

Coulombs per particle. Using the Cern cross section for ^{24}Na production we get $3.38\pm.097x\,10^{-18}$ Coulombs per particle.

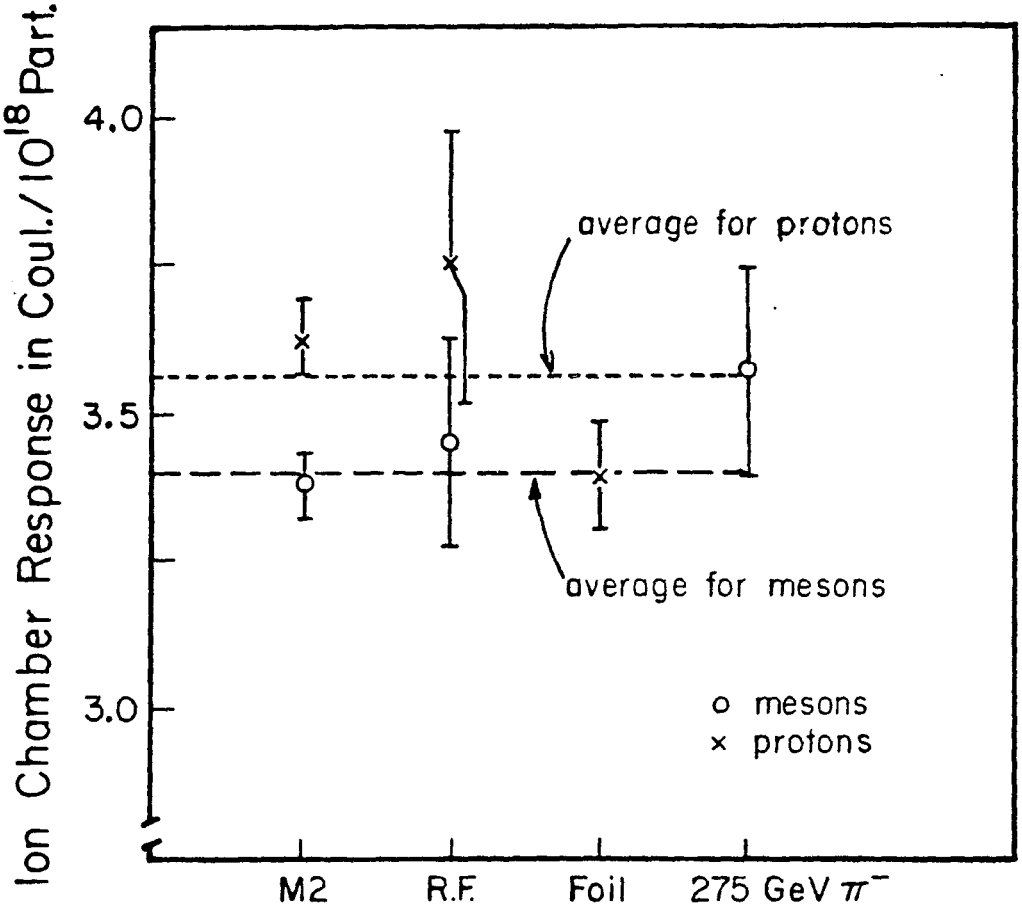

Figure 2-7: Calibration of the ion chamber. The results of several calibration runs done with different beams and at different times are summarized here. The difference between the ion chamber response for mesons and protons observed in the most accurate calibration runs (labeled M2), motivated the separation into two different calibration constants (one for protons and one for mesons).

Two other calibrations were done with test chambers in low intensity beams with the intensity monitored by counting particles using scintillation counters. Our best calibration was done this way in the Fermilab M2 beam line. The results were $3.38\pm.05x\,10^{-18}$ Coulombs per particle for mesons and $3.63\pm.06x\,10^{-18}$ Coulombs per particles for protons.

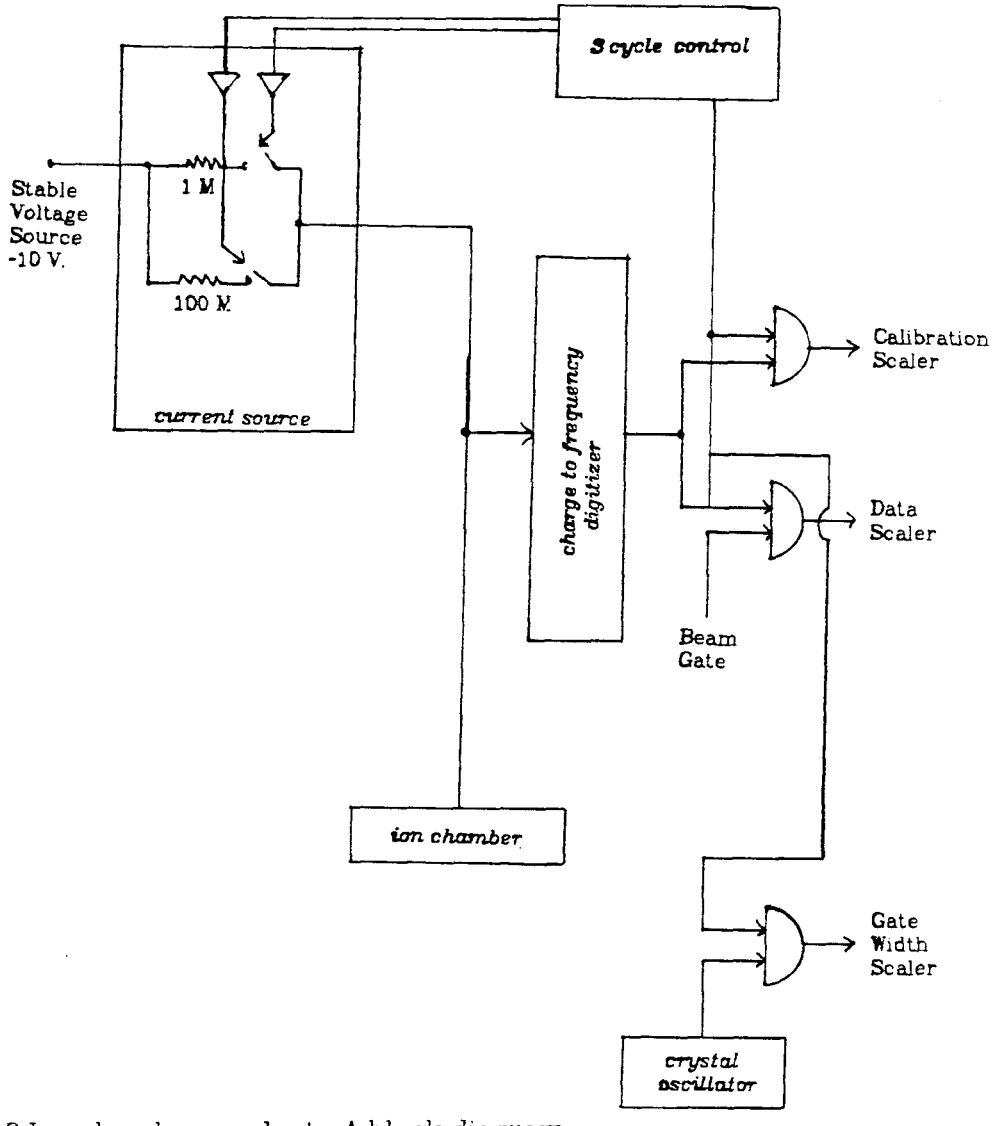

Figure 2-8:Ion chamber readout. A block diagram of the electronics used to read out the ion chamber. The 3 cycle control sets the current source switches and a logic level. The switches may be set for - no output, .1 microamp or 10 microamp.

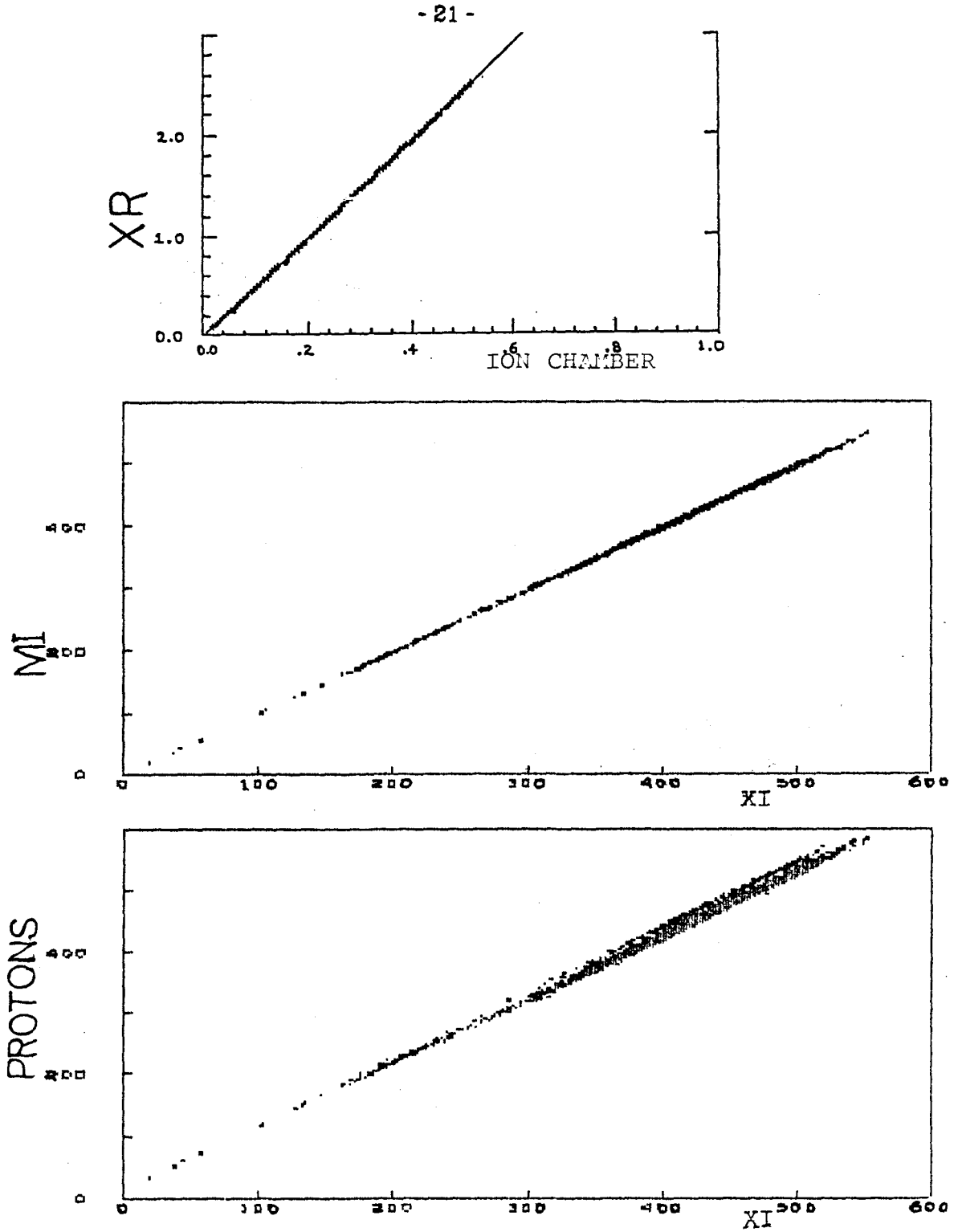

Figure 2-9: Cross comparison of monitors. The ratio of various primary and secondary intensity monitors are plotted, to demonstrate their linearity. The devices used to obtain neutrino flux are the manhole and expansion port ion chambers labeled MI and XI respectively. The other monitors include the R.F. cavity (XR) and a toroid used to monitor protons incident on the production target.

See figure 2-7 for a comparison of the various calibration results. During neutrino running, the output of the ion chambers was digitized using a charge to frequency converter and a scaler; a block diagram of the ion chamber readout appears in figure 2-8. Throughout the running, along with the output of the ion chamber during the beam, calibration pulses were digitized which monitored the zero response and signal responses at two different input charge levels. A comparison between several devices which monitor intensity appears in figure 2-9.

2.5.Cherenkov Counter Pressure Curves

Accurate calculation of the neutrino flux requires a knowledge of the number of pions and kaons that pass down the decay pipe. The total number of particles can be measured using the ion chambers. The relative number of pions and kaons was determined using an integrating Cherenkov counter (see figure 2-10). Basically, the Cherenkov counter consists of a helium radiator and optics designed to collect all light emitted at an angle $\Theta_0 \pm \delta$ from the axis of the counter. For a monoenergetic beam of one species (of mass m_0, momentum p_0) and no angular dispersion, changing the pressure of the helium (and therefore the index of refraction) would give a response like that portrayed in figure 2-11. This follows from the pressure dependence of the index of refraction and laws governing the emission of Cherenkov light [LI73].

$$n = 1 + \kappa P$$

$$\Theta_c^{\,2} = 2\kappa P - \frac{m_0^{\,2}}{p_0^{\,2}} \propto I_c$$

Where n = index of refraction of the helium radiator

κ = constant depending on gas and spectrum of light sampled

$\mathbf{P}$ = pressure of helium

Θ_c = emission angle from particle trajectory of Cherenkov light

I_c = intensity of emitted light

The threshold values of $\mathbf{P}_a$ and $\mathbf{P}_b$ in figure 2-11 where the intensity falls to zero are given by:

$$\mathbf{P}_a = \frac{[(\Theta_0-\delta)^2 \div \frac{m_0^2}{p_0^2}]}{2\kappa}$$

$$\mathbf{P}_b = \frac{[(\Theta_0-\delta)^2 + \frac{m_0^2}{p_0^2}]}{2\kappa}$$

the area of the pressure curve will be:

$$A_c = \Delta\mathbf{P}((\Theta_0-\delta)^2+\kappa\Delta\mathbf{P})\cdot g \cdot N$$

$$\Delta\mathbf{P}=\mathbf{P}_b-\mathbf{P}_a=\frac{(\Theta_0+\delta)^2-(\Theta_0-\delta)^2}{2\kappa}$$

Where the output is integrated over a pulse with N particles and g is some constant which depends only on the counter properties (it does not depend on m_0, p_0, Θ_c, etc.)

Since $\mathbf{P}_a$ and $\mathbf{P}_b$ depend on the ratio of $\frac{m_0}{p_0}$, provided Θ_0 and δ are chosen appropriately, a mixed beam of pions, kaons and protons would give three separate regions of non zero output in a plot of Cherenkov output versus pressure. The area of each "lump" would be proportional to the number of particles of each

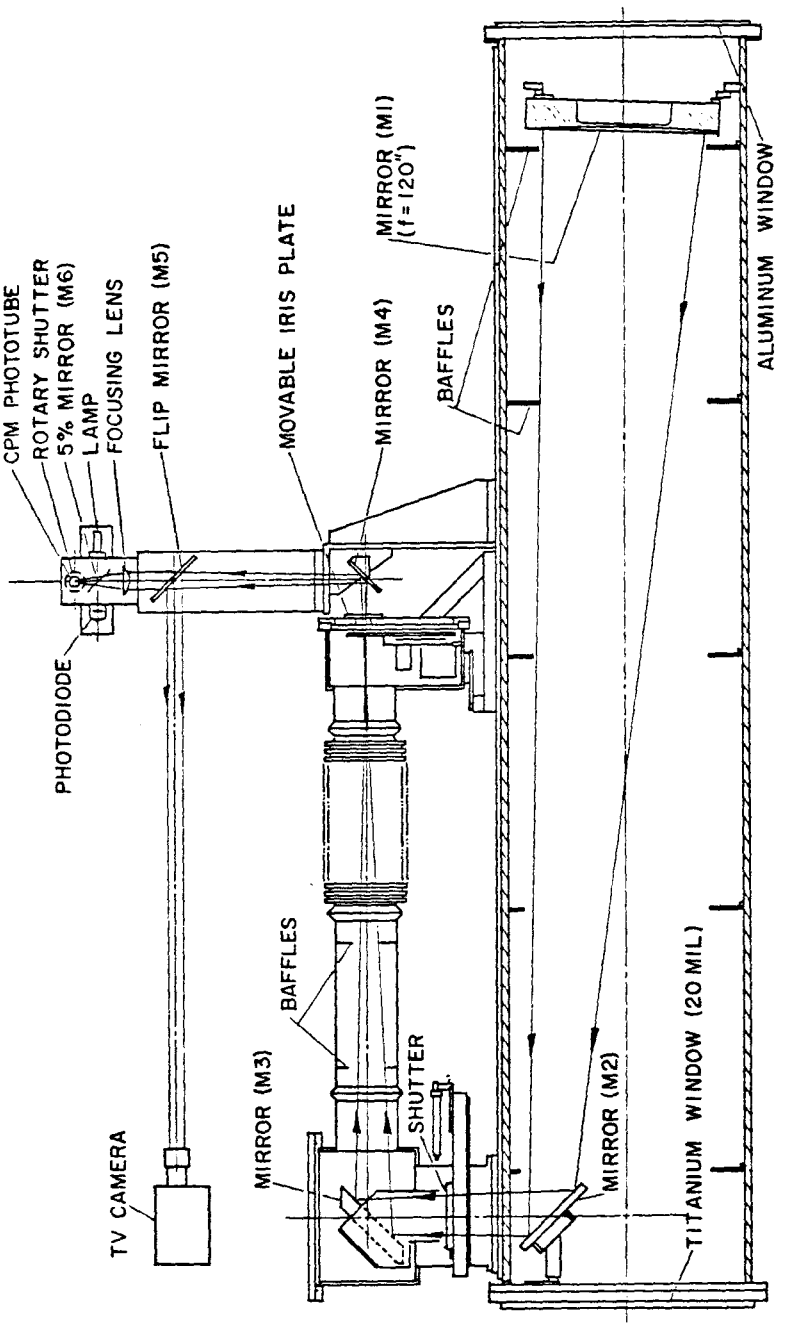

Figure 2-10: Cherenkov Counter. The beam enters from the left in this drawing. Note in particular the shutter (between mirrors M2 and M3) used to measure how much light is produced outside of the radiator.

type, with the same proportionality constant. We could measure the fraction of each particle type by comparing the area of that type's "lump" to the total area of the Cherenkov pressure curve. Provided the angular dispersion of the beam is small with respect to Θ_0 and the momentum spread does not induce significant overlap of the various "lumps" in the pressure curve, this method is valid for a real particle beam. The dichromatic train has a typical angular dispersion of .2 mr. This is small compared to Θ_0 = .85 and δ = .15 used. The "lumps" are well separated as can be seen in figure 2-12, where a typical curve is exhibited after all background subtractions and corrections are made. A Monte Carlo study was performed to insure that this simple area scaling approach did not introduce any significant error into the particle fraction evaluation. The method was good from 1% to 2% and the level of uncertainty induced by using this scheme was considered insignificant compared to larger experimental errors.

2.5.1. Background Subtraction

There are four backgrounds which must be subtracted from the Cherenkov pressure curves. These backgrounds represent spurious light which does not originate from secondaries passing through the helium radiator.

The first source of background is measured directly. Light is produced outside of the radiator by Cherenkov emission in the optics of the counter. Any light produced outside of the radiator was measured periodically while making a pressure sweep by closing a shutter which isolated the radiator from the rest of the counter optics. The counter output with this shutter closed is pure background.

Another source of background is light produced by particles which are collision products of beam interactions in material in front of the Cherenkov counter. These collision products may be produced at large angles and are a

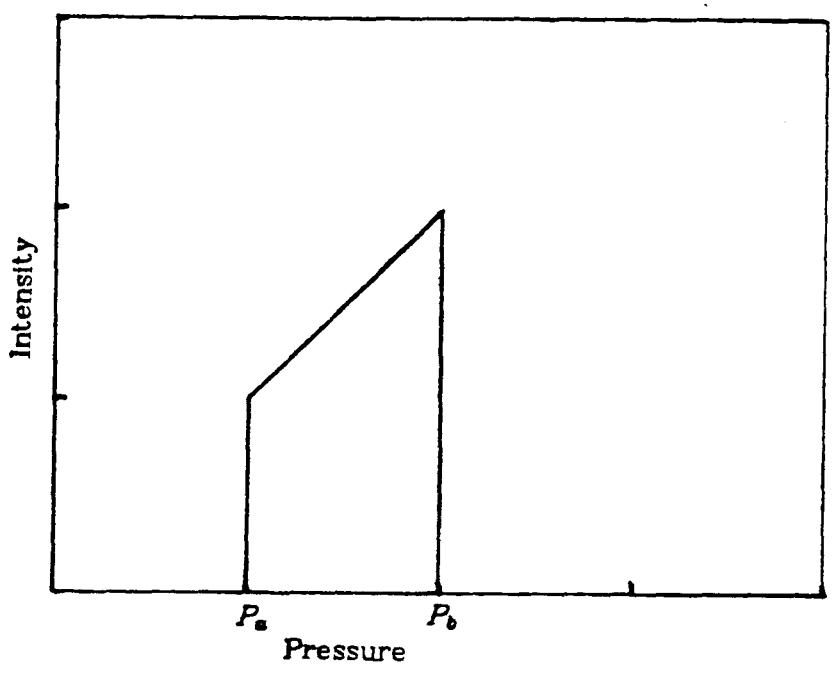

Figure 2-11: Ideal beam Cherenkov output. For gas pressure below P_a, the ring image of the Cherenkov light produced by a monoenergetic beam is too small to pass through the iris of the Cherenkov counter. For gas pressure above P_b, the ring image is too large. In between all the Cherenkov light is passed and its intensity rises linearly with pressure.

source of diffuse Cherenkov light. Measurements were made with additional material in front of the Cherenkov counter to assess this source of background.

Additional light reached the phototube indirectly by scattering off of counter walls, baffles, and contaminants on the mirror surfaces. This source of background will be proportional to the amount of Cherenkov light produced. Runs were done with main ring 200 GeV protons brought through the train. This provided a pure beam of extremely monochromatic protons ($\frac{\Delta p}{p} \ll 1\%$). After subtracting the material contribution (measured with material in and out runs), we have a determination of the pressure dependence of the light scattering background. This "point source" shape was scaled appropriately and integrated over the pion, kaon and proton peaks of each Cherenkov curve to yield a light

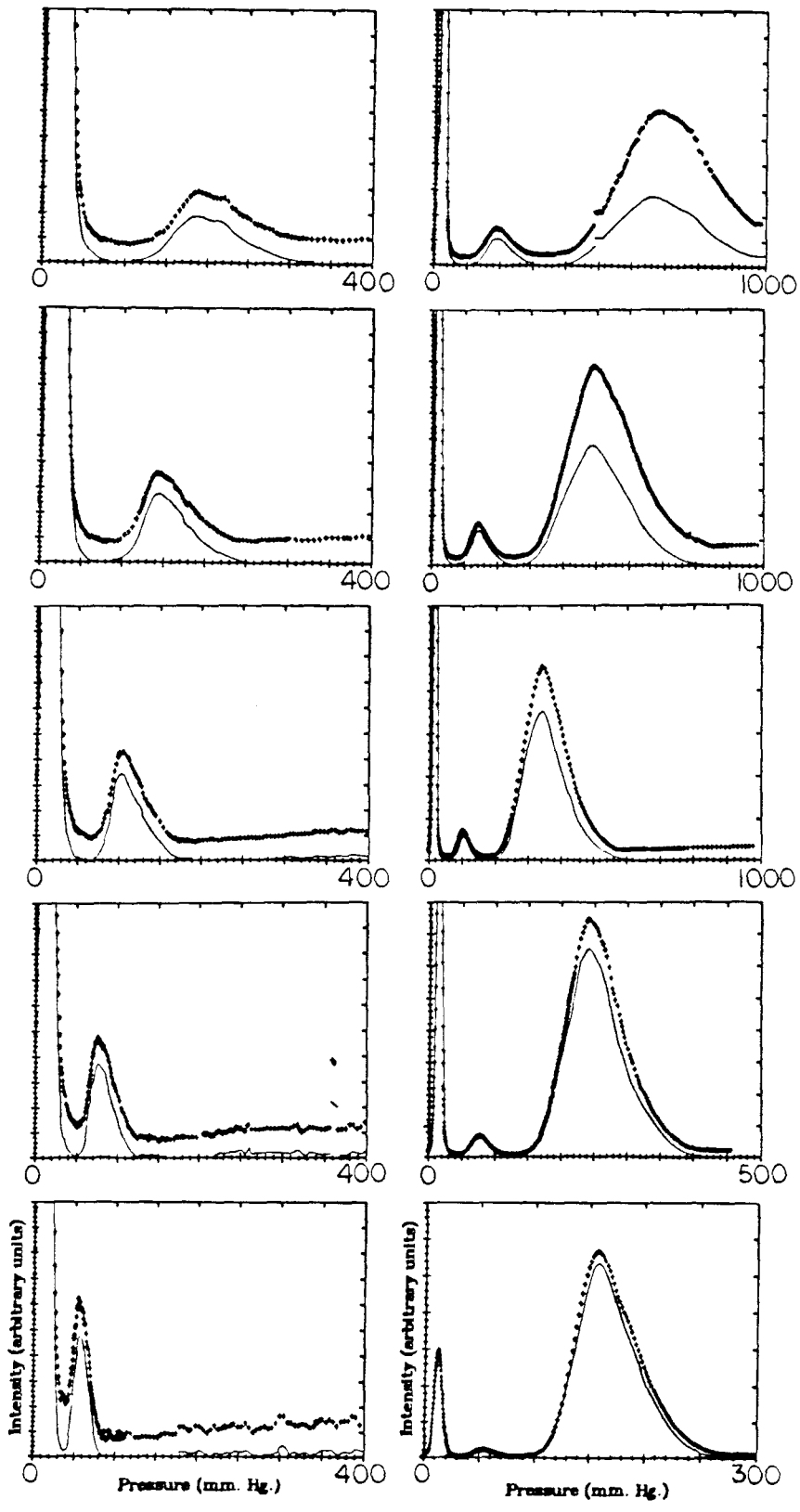

Figure 2-12: Cherenkov curves. The discrete points are Cherenkov data for each of the secondary settings (upper left hand corner down is -120 through -250, upper right hand corner down is +250), after subtracting the shutter closed background. The solid lines are the corresponding curves after all corrections for material, lightscattering etc.(see text).

scattering background shape which was then rescaled to make the total background agree at pressures well above the proton peak (up to 10% adjustments in material background were also made to facilitate the high pressure match). The rescaling accounted for any time dependence imposed by additional dust depositing on the mirrors.

The final background was of unknown origin. The Cherenkov light produced in the gas radiator must go to zero as the pressure is reduced to zero. This was not observed. The output at the lowest pressure point ($\sim$ 60 microns) was higher than the valley between pions and kaons. Since at low energies high energy electrons in the beam could be distinguished as a separate peak, this light was produced by a source distinct from Cherenkov emission in the gas radiator. Possible sources include fluorescence produced in the counter walls and mirror coatings. Monte Carlo studies indicated that, in the absence of decay products, the valley between pions and kaons should go to zero output. For different energy settings the pion to kaon valley appears at various pressures. The ratio of valley to zero pressure output formed a universal curve in pressure. This curve was used to indicate the pressure dependence and the zero pressure output was used to normalize the level of this background for each curve. This background was significant only in the low pressure part of the Cherenkov curve (see figure 2-13).

2.5.1.1. Alignment Correction

Due to physical instability of the Cherenkov counter, the optical axis of the counter shifted as the gas pressure was changed. Alignment of the counter was usually performed just beyond the pion peak by rotating the counter with respect to the beam to force the image of the Cherenkov light at the iris plane to be circular. The misalignment tended to spread

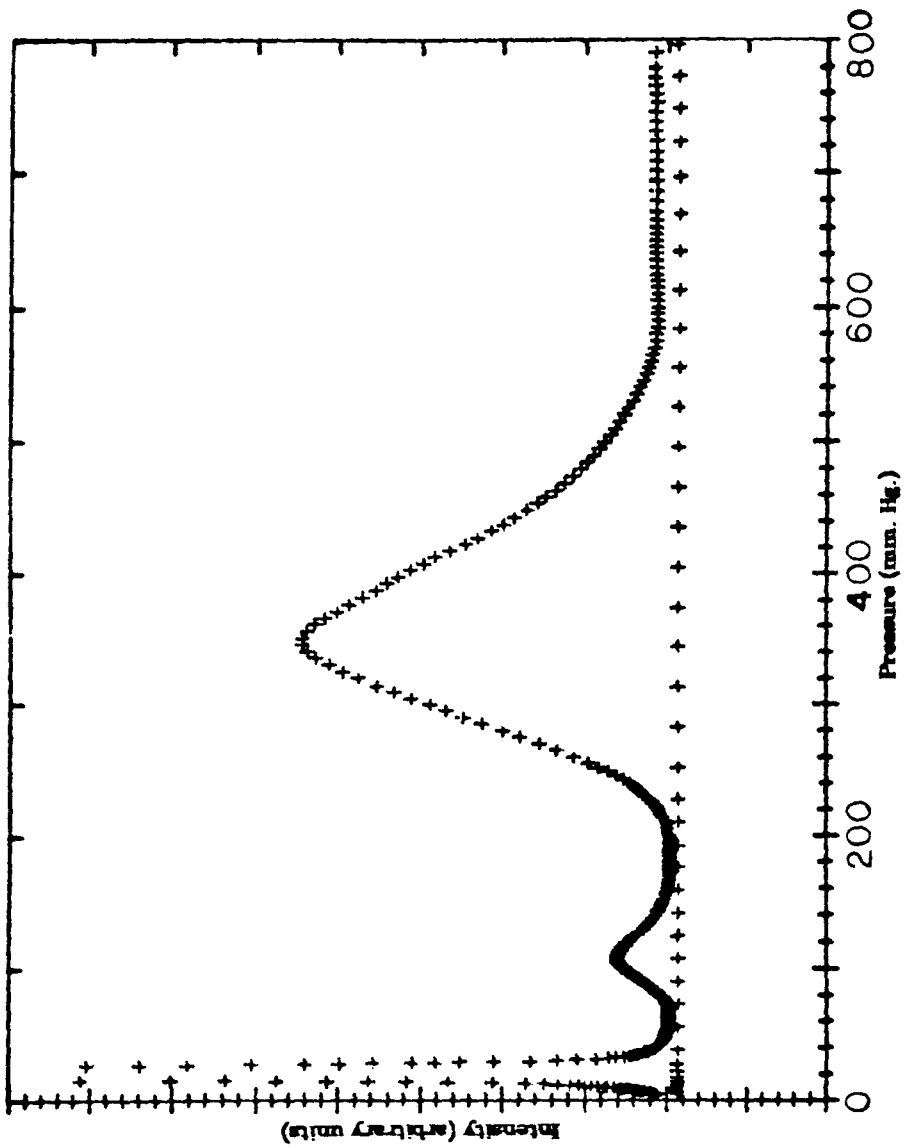

Figure 2-13a: Cherenkov Backgrounds.
Raw curve with closed shutter data. The data points that form a flat pedestal above which sits the cherenkov curve, are the counter output with shutter closed.

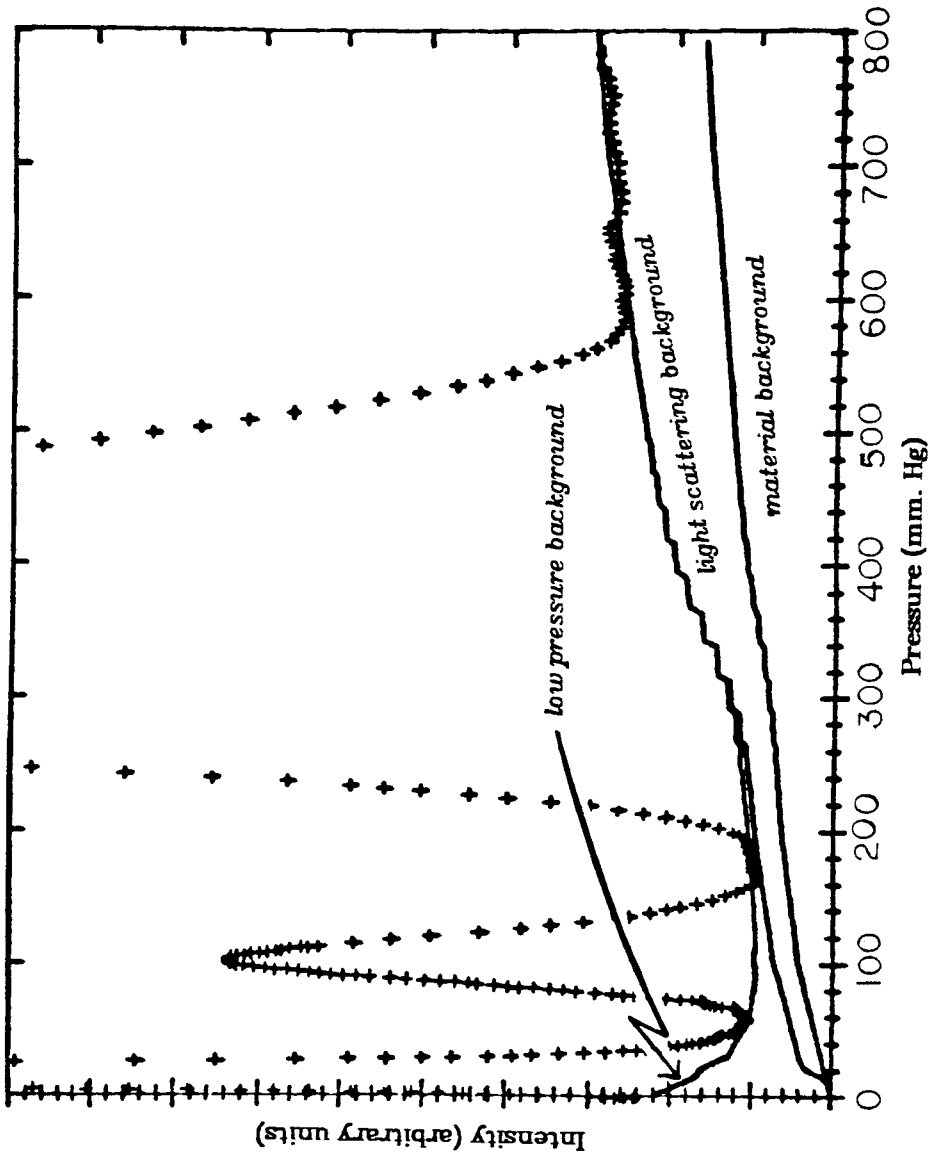

Figure 2-13b: Cherenkov Backgrounds.
Remaining backgrounds (see text) are designated along with the curve, from which they are to be subtracted.

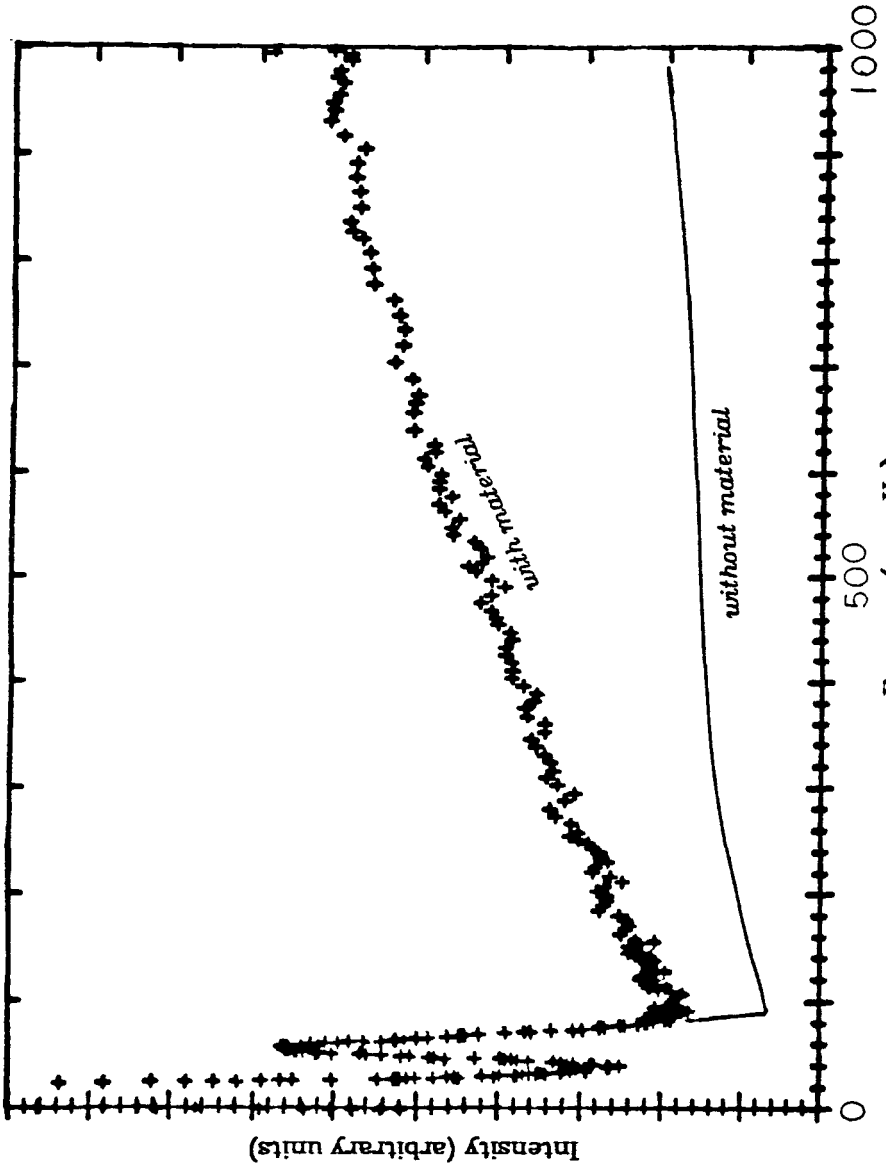

Figure 2-14: Measurement of material background. Curves were taken with additional material in the beam to assess the background due to scattering and interactions in the windows. The data points are a curve taken with additional material in the beam. The solid line shows the level without the additional material (only the window material remains).

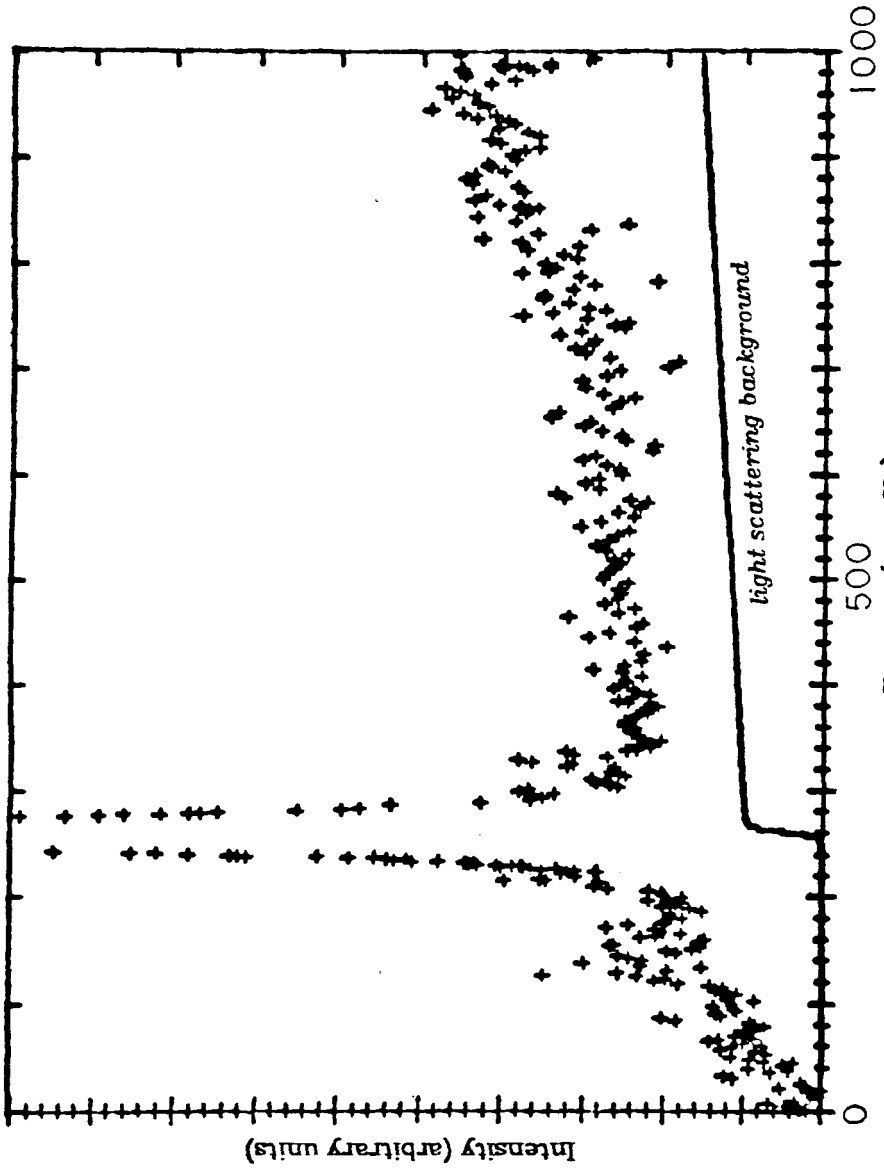

Figure 2-15: Measurement of background due to scattered light. Cherenkov curve with 200GeV. monoenergetic protons. The peak (from about 200-300mm. Hg.) rises above a background due to material and light scattering. The material background is evaluated from runs with additional material. The remaining background (solid line) results from light scattering in the optics.

out the proton and kaon pressure peaks. When this problem was discovered, after the running, the Cherenkov counter was fitted with a special window and a theodolite was used to measure the shift as a function of gas pressure (see figure 2-16). The pressure dependence of the misalignment was very reproducible. This measurement was used to correct the curves to what would be obtained with the counter properly aligned.

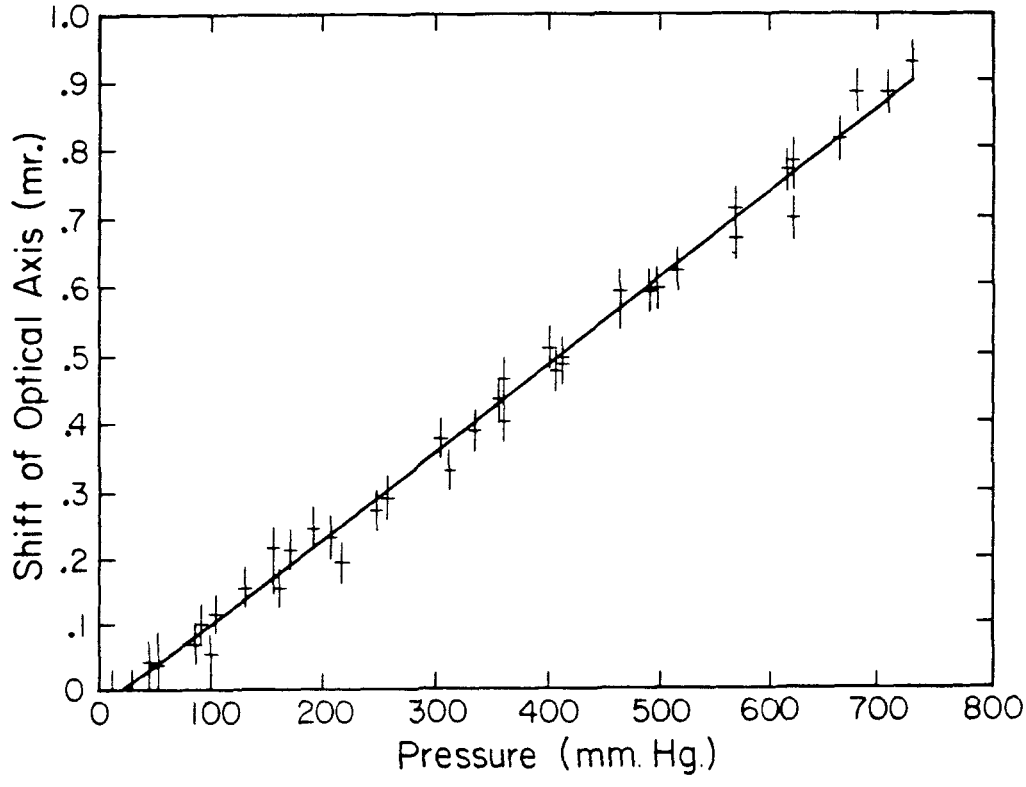

Figure 2-16: Shift of Cherenkov optical axis versus pressure. Due to poor design, the Cherenkov counter flexed upon being filled. The effect of this flexing was to move the optical axis with respect to the iris. The above plot shows this effect.

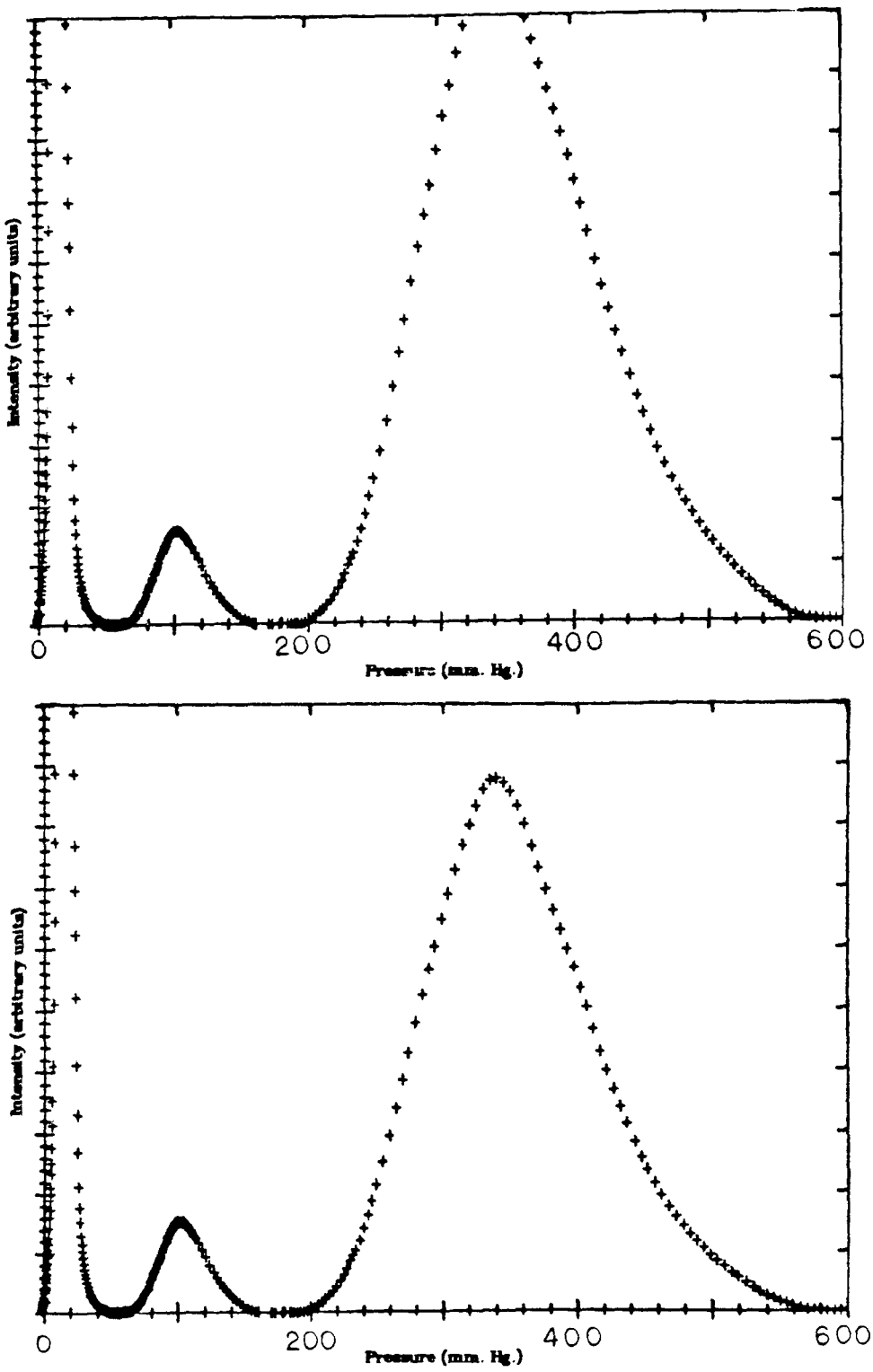

Figure 2-17: The effect of misalignment on the pressure curves. A curve (+168GeV. secondaries) is shown before (above) and after (below) the correction for the shift in the optical axis as a result of counter flexing.

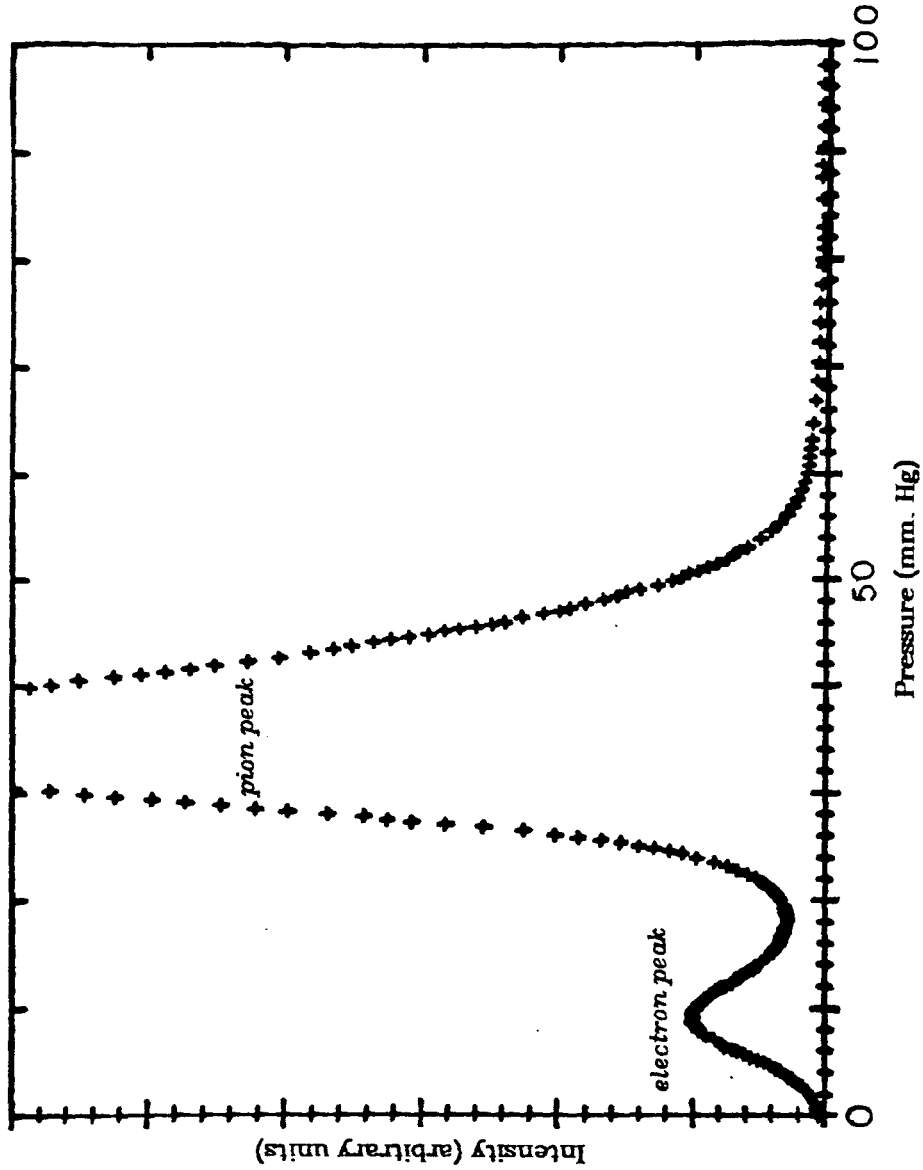

Figure 2-18: Electron pion Cherenkov curve. Part of a 90GeV. Cherenkov curve showing the electron and pion peaks. Note that no data were taken at 90GeV.

2.5.1.2. Electron and Muon Content of the Beam

In addition to pions, kaons and protons the beam has some electrons and muons. The electrons are predominantly from π^0 decay and gamma conversion at the production target. The muons are decay products from pion and kaon decay. The electrons, having passed through the train, are momentum selected and at low energies, show up in the pressure curve as a peak at a pressure slightly lower than the pressure of the pion peak (see figure 2-18). At higher momentum settings (greater than 140 GeV.) the pion and electron peaks are not resolved, so we must rely on a calculation of the electron content relative to the pion content of the beam. The result of the calculation and low energy measurements are shown in figure 2-19.

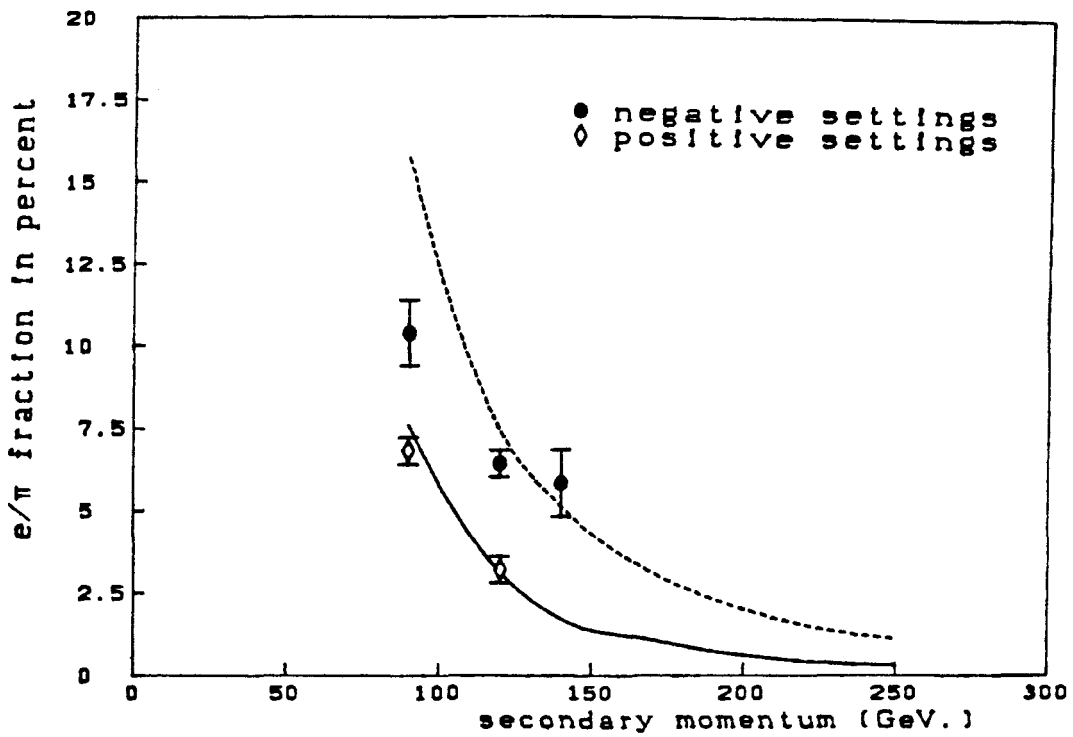

Figure 2-19: Electron content of the beam. The calculated electron content of the beam, relative to pions (smooth curves) and the low energy measured values.

Accounting for the muon content of the beam is more problematic since the muons are not momentum selected and tend to contribute over a wide range of pressure. Muons from pion decay will generally form a peak which is not resolved from the pion peak (most of this peak is underneath the pions, the rest is between the pions and the kaons). The contribution of decay products from kaon decay do not add to one single pressure region. Since the method of background subtraction (in particular the "zero pressure" background) tended to eliminate some part of this contribution,, and since the level is small (<.5%), the decay product contribution was considered uncertain. Appendix 1 contains a more detailed description of how this uncertainty was evaluated and incorporated into the systematic errors.

2.5.1.3. Particle Fractions

After making all the background subtractions and corrections to the pressure curves, we can use the relative areas of each peak to find the beam composition (see figure 2-12 for an example of a pressure curve after all corrections). Figure 2-20 shows the particle fractions versus momentum and, for comparison, the results of a beam survey done at CERN with various target lengths, production angles and momenta [AT80].

2.5.1.4. Evaluation of the gas constant

As mentioned above, runs were done with main ring 200 GeV. protons brought through the train. These runs provided valuable information for background subtraction and also give us an accurate determination of κ in the Cherenkov expression. The 200 GeV. protons give us a monochromatic beam with a well determined momentum. The position of the peak in the Cherenkov curve for such a beam and the iris dimensions

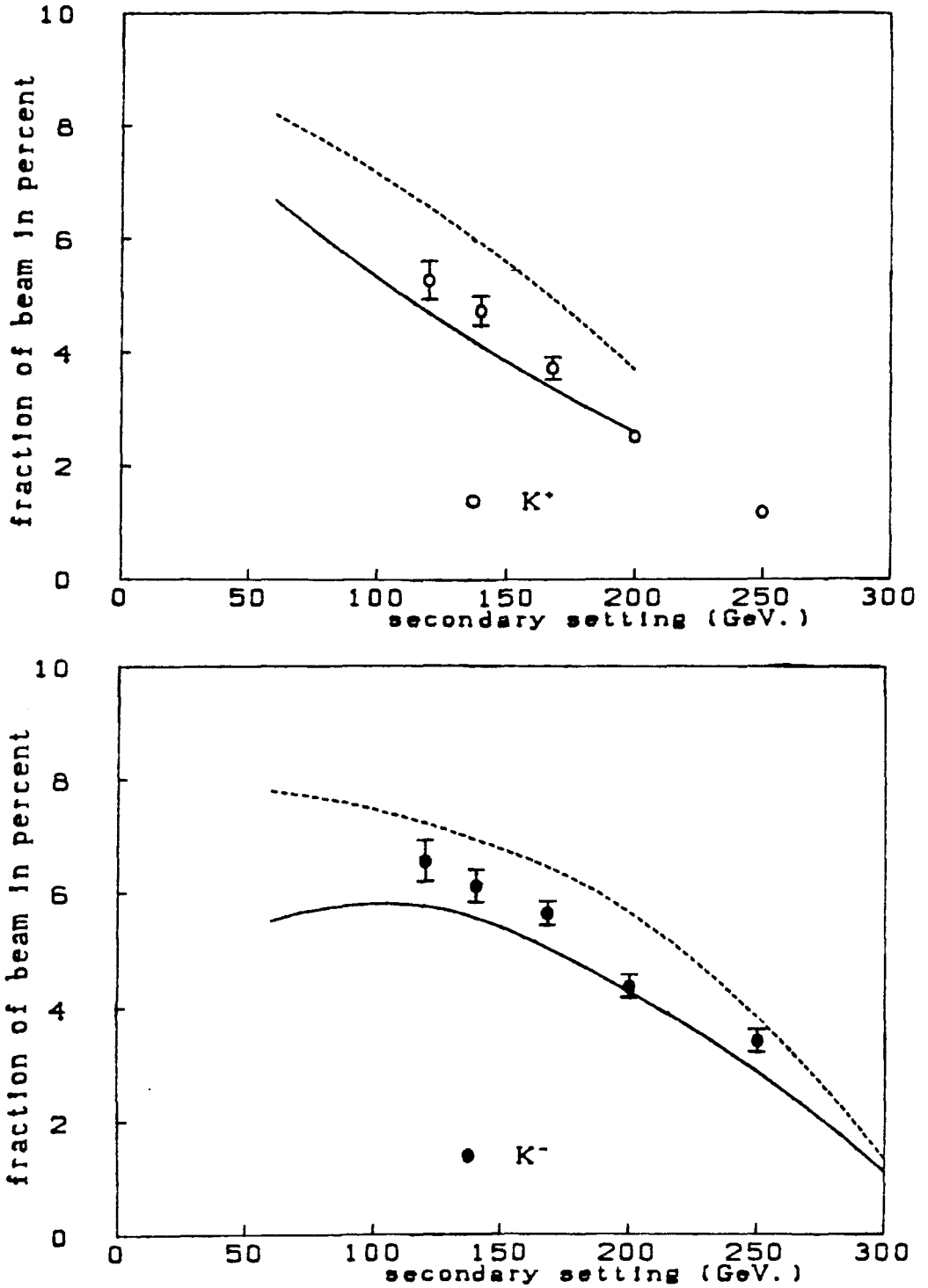

Figure 2-20: Particle fractions. The fraction of kaons and pions to all charged particles are depicted along with two curves showing the range of values expected from the CERN beam survey [AT80]. The solid line is a smooth curve through the CERN data for forward production. The dashed curve is an estimate from the CERN data of 3.4 mr. production (about the limit of the train's acceptance).

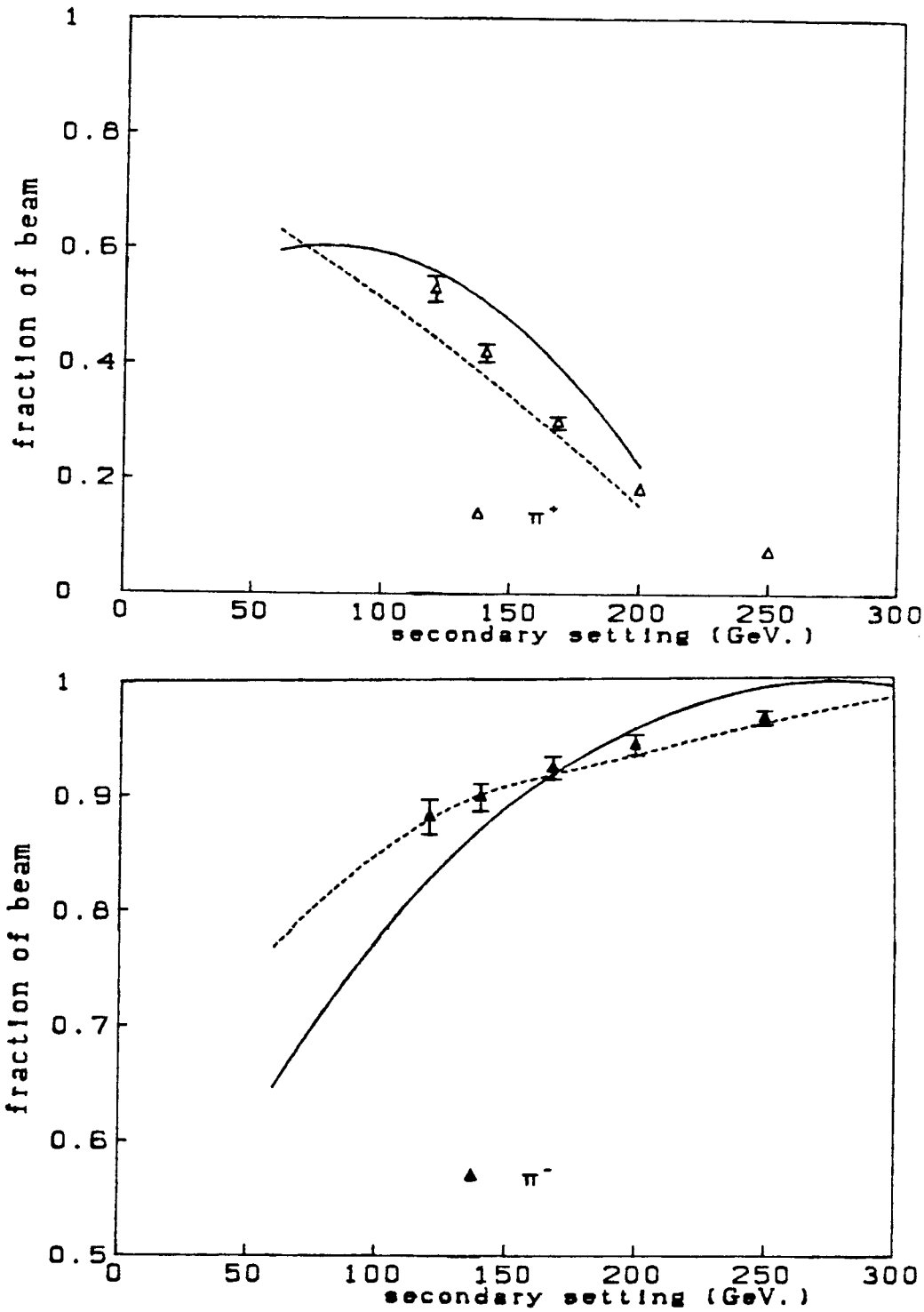

Figure 2-20: (see previous page for caption)

yield the value of κ averaged over the frequency of light sampled. The value obtained in this way is $4.38\pm.04 x \frac{10^{-8}}{mm \cdot Hg}$. The error is dominated by the lack of temperature compensation (κ will vary inversely with temperature). While the Cherenkov gas temperature was monitored, no correction was made for temperature differences between runs. The level of other uncertainties is about one tenth of the overall error.

2.5.1.5.Average Momentum

The pressure curve for a given particle type acts as a momentum transform of the beam. The low momentum component maps to the high pressure part of the curve, and the high momentum maps to the low pressure part. Given the values of κ and the iris size, we can use the average pressure of the curve to reconstruct the average momentum. For an ideal beam (with no angular dispersion but some momentum dispersion):

$$2\kappa\langle P\rangle = \left\langle \frac{m^2}{p^2} \right\rangle + \frac{2(\Theta_2^4+(\Theta_1\Theta_2)^2+\Theta_1^4)}{3(\Theta_1^2+\Theta_2^2)}$$

where $\langle P\rangle$=the average pressure of the peak

Θ_1,Θ_2= limits of the Cherenkov light accepted (~ 1. mr. and ~ .7 mr.)

The smaller the particle mass the more important the second term, the angular term, on the right hand side of the above expression is. Because of this, the uncertainty introduced by the angular dispersion of the beam becomes significant for pions (see figure 2-21). Because the contribution of angular divergence was significant (from 3% to 12%), we did not try to

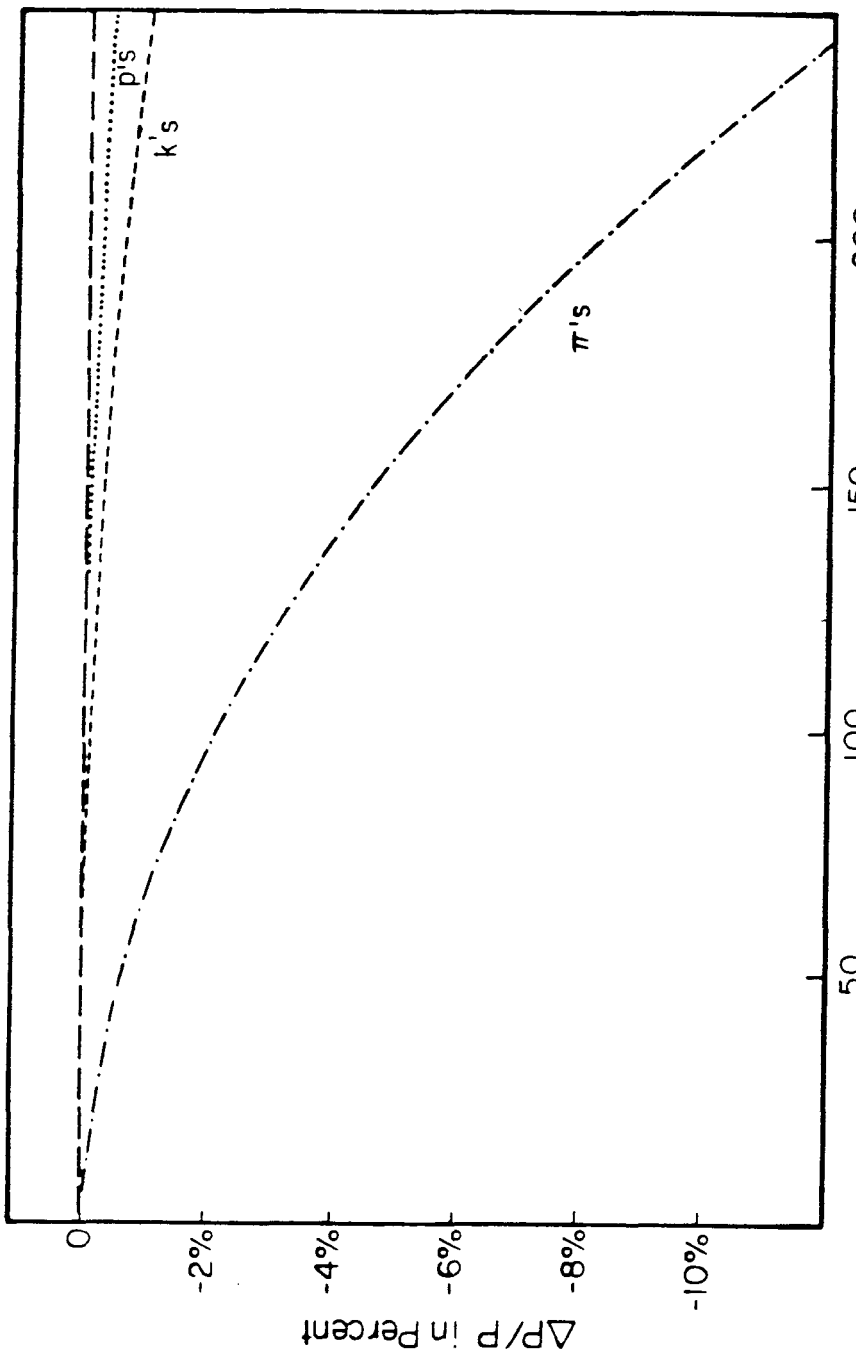

Figure 2-21: Effect of angular dispersion on determining mean momentum. The evaluation of momentum from mean pressure of the Cherenkov peak is affected by the angular spread of the secondaries more or less depending on their mass. The above curves illustate this by showing how much uncertainty arises from a .2mr. to 0 change in r.m.s. angular divergence (about 100% for our beam).

use the average pressure as a measure of momentum for pions. Instead, we used the other method of evaluating secondary momentum, comparison of the total energy of neutrino events from pion decay to that expected from the Monte Carlo to find the momentum of the pions. We then used this momentum to evaluate the angle term in the above expression. From the nominal values of the iris in the Cherenkov counter, we expect $2(\Theta_2^4+(\Theta_1\Theta_2)^2+\Theta_1^4)/(3(\Theta_1^2+\Theta_2^2))$ to be $.774x10^{-6}$. Averaging the different energy settings and using the total energy of neutrino events to estimate $<\frac{m^2}{p^2}>$ for pions gives $.76x10^{-6}$ (see figure 2-22). The latter value was used since it was considered to include beam angular divergence as well as counter properties (see Appendix 1 for more detail). A comparison of the average kaon momentum deduced using the mean pressure and the total observed energy of neutrino events appears in figure 2-23.

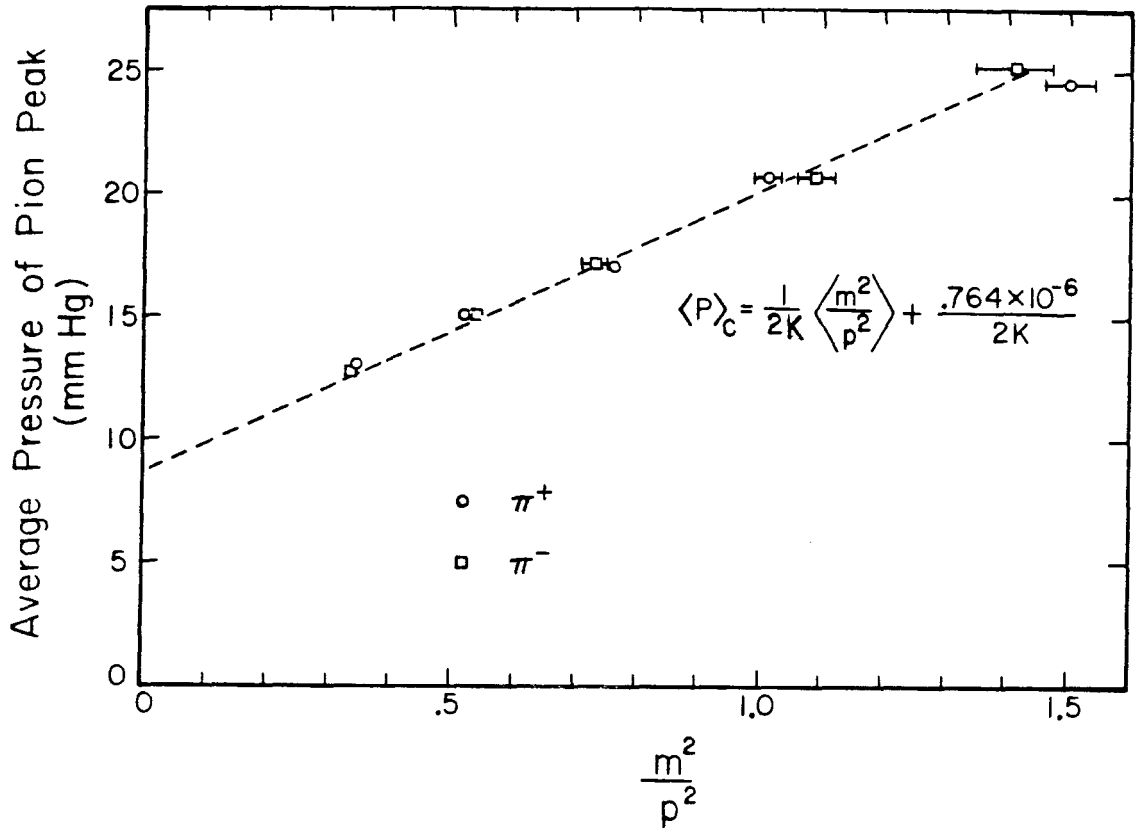

Figure 2-22: The determination of the angle term in the Cherenkov relation. The value of m/p for pions can be determined from the average energy of neutrinos emitted forward in pion decay. The effective iris size can be determined by using this and the mean pressure and extrapolating to m/p = 0.

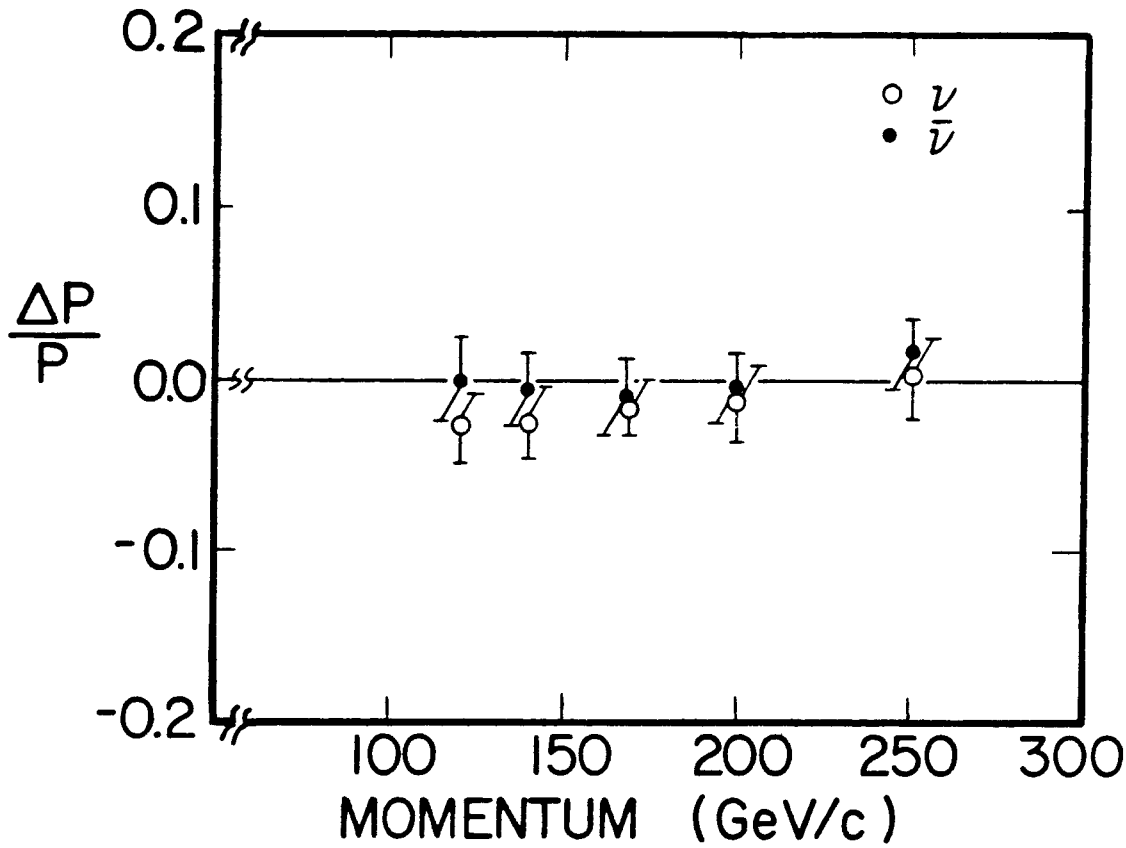

Figure 2-23: Comparison of kaon mean momentum measurements. Two methods were used to determine the mean kaon momentum: the average energy of neutrinos from kaon decay and the mean pressure of the Cherenkov pressure peak. The difference in the two methods is displayed above.

3. The Lab E Apparatus

3.1. Target Statistics and Layout

The apparatus in Lab E consists of an instrumented target and toroidal momentum analyzing magnet. Both, the target and toroidal magnet are sandwiches of iron, scintillation counters and spark chambers (details of the spacing and layout can be found in table 3-1 and figure 3-1). The target was organized into six approximately cubic blocks which could be moved on tracks (perpendicular to the axis of the apparatus) into the N5 charged particle beam line. The toroid was, in similar fashion, organized into three independently movable toroid carts. This structure and the nearby charged particle beam made calibration and resolution measurements possible directly on the apparatus.

For completeness, a brief description of the apparatus is included here, but more detail will be found in reference [LE81].

Table 3-1: Target and Toroid Statistics	
Target tonnage	642 metric tons
Toroid tonnage	380 metric tons
Scintillator sampling density:	
Target	1 counter / 10.8cm.Fe
Toroid	1 counter / 21.6cm. Fe
Chamber spacing (approx.):	
Target	48cm.
Toroid	150cm.
Steel between chambers (approx.):	
Target	23cm. Fe
Toroid	80cm. Fe
Magnet pperp kick	2.45GeV./c total .408GeV./c for each half toroid cart

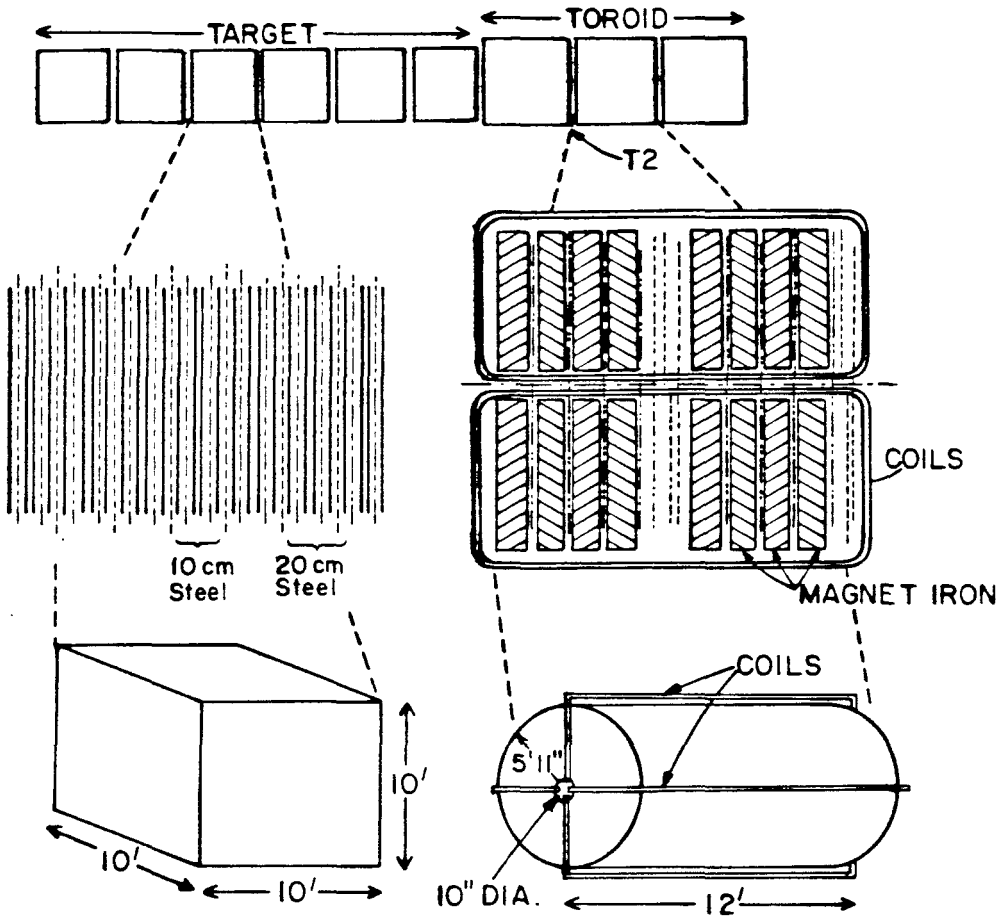

Figure 3-1: Diagram of the Lab E detector. The various components of the detector and their relationships are designated.

3.2. Spark Chambers

There are six spark chambers in each target cart, a set of spark chambers in between toroid carts and in the gap in the middle of each toroid cart. Each chamber had x and y wires with 1 mm. spacing. The chambers were read out by x and y magnetostrictive "wands" along the edge. The resolution of the chambers was ±.5mm. The chambers were fixed with respect to each other (aligned) using muons that passed through the whole apparatus. The accuracy of this procedure was 10 mils in the target and 15 mils in the toroid chambers. For each event all wand hits plus a beginning and end fiducial were recorded.

3.2.1. Muon momentum resolution

The amount of steel between chambers and the chamber resolution determine the accuracy with which the momentum of a muon can be reconstructed from its toroid track. The muon momentum resolution for this experiment is 11% to 12%. The chamber resolution contributes very little to this value (<1%) in the energy range of this experiment.

3.3. Scintillation counters

There were fourteen liquid scintillation counters in each target cart and eight acrylic counters in each toroid cart. The target counters were 10'x10'x1" tanks of clear plexiglas which contained a mixture of scintillator and wavelength

shifter in the body of the counter and shifter bars along the edges for light collection. Each "counter" was actually constructed of four 5'x5'x1.5" sheets of acrylic scintillator , each surrounded by "shifter" bars (see figure 3-2).

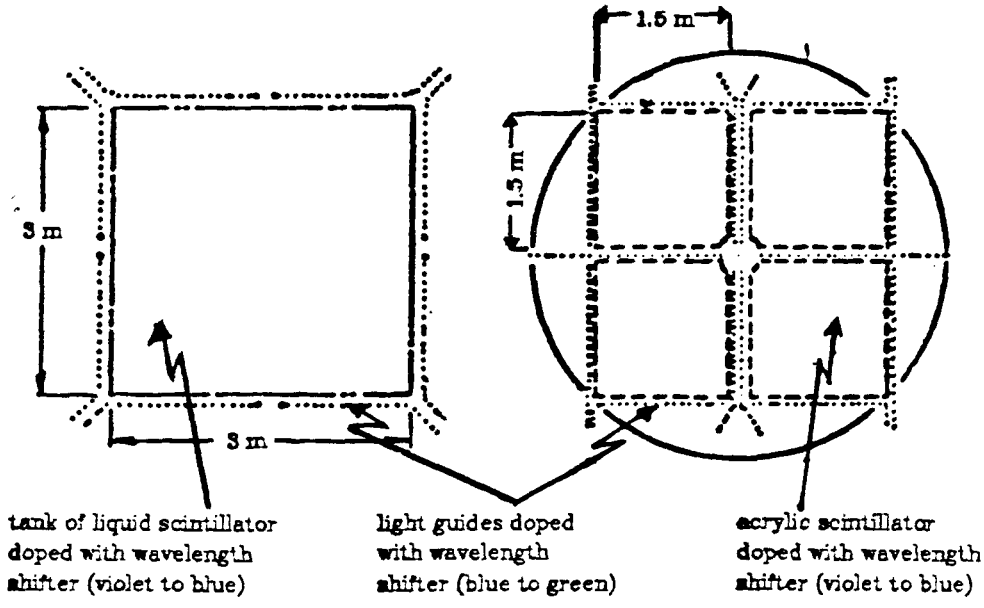

Figure 3-2: Counter construction. Note that the toroid counters consist of two independent pieces (the left and right halves are in separate boxes). This allows them to be installed without moving the magnet coils.

3.3.1. Analog Counter Information

The output of each phototube was split to provide trigger information and to allow for digitization with ADC's of differing dynamic ranges (see figure 3-3). For each tube a "low" ADC digitized the tube output, a "high" ADC digitized the output of the sum of all tubes in a counter and a "superlow" ADC digitized the output of the sum of several tubes in different counters. For this analysis the fiducial volume for events was restricted to be well within the target. The ADC's used for the target accurately digitized (~ 1% linearity) pulse heights from

about 1 times minimum ionizing to 1000 times minimum ionizing (where minimum ionizing is the average output obtained when a relativistic muon traverses the center of the counter). This was adequate for all but a very small (<1%) number of events where one of the "low" ADC's saturated, in these cases the appropriate superlow was used to recover that tube's output.

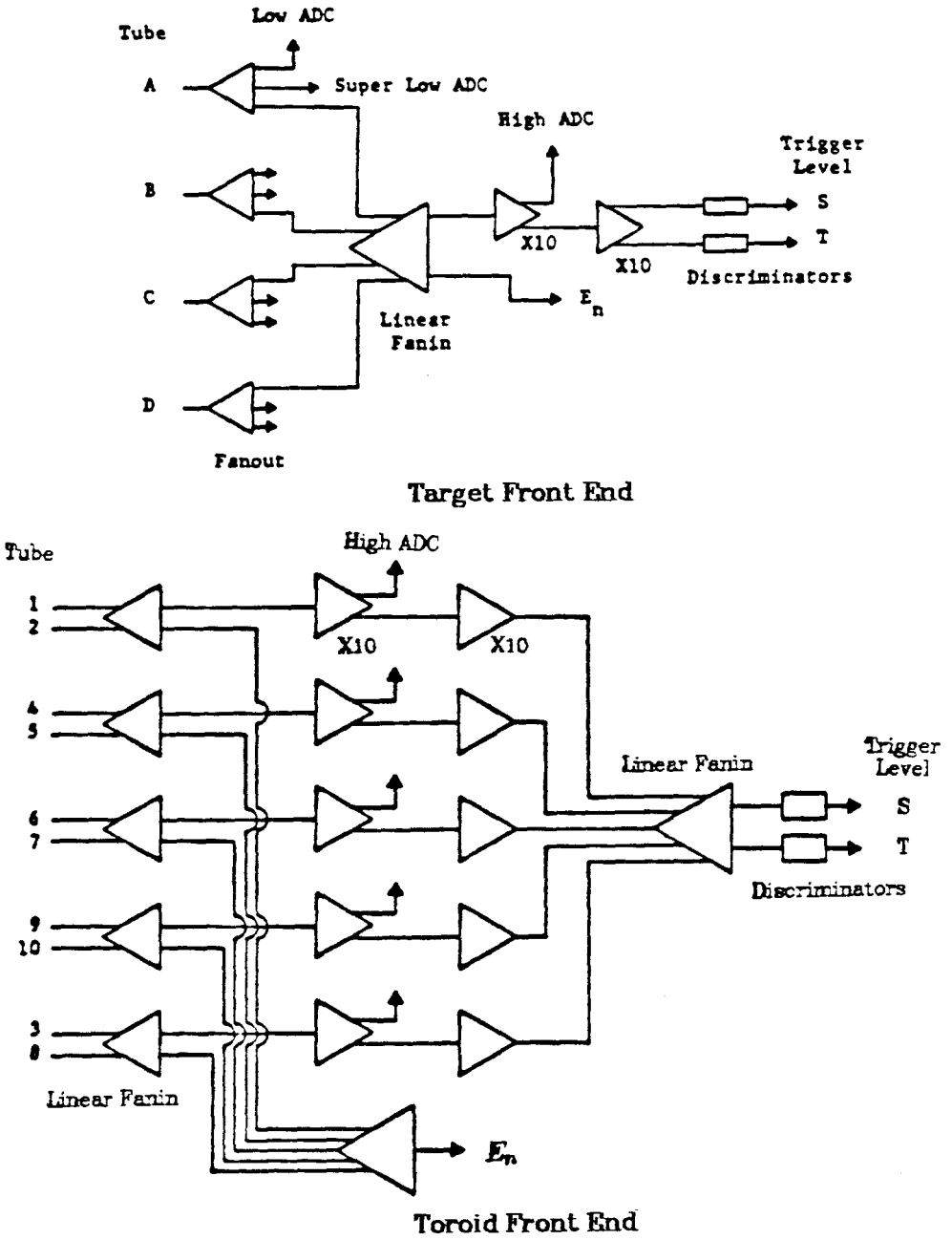

Figure 3-3: Target and toroid front end electronics. The input electronics for each of the 82 target counters and 25 toroid counters is depicted above. The S,T and E_n lines are used for the trigger electronics.

3.3.2. Counter Maps

The size of the target counters is of order of the attenuation length of the blue light which must travel to the edge (a 10' counter length compared to attenuation lengths of approximately 6'). In order to correct the outputs for this attenuation, counter maps were constructed using neutrino events. A model of the counter response was made which had 4 parameters, the center of the counter with respect to the spark chambers and the horizontal and vertical attenuation lengths (the counters have vertical ribs, for mechanical stability, which allows a possible difference between horizontal and vertical attenuation). This model used the known optical properties of the counters to calculate (given the above parameters) the expected light output of each tube. For each neutrino interaction we measured the event interaction point and the output of each tube. The model allowed us to fit the relative tube outputs versus interaction point. As an example, for the i^{th} event we can add a term to a χ^2 sum of the form:

$$\delta_i^2 = \frac{(a_i - e_i \cdot A(x_i,y_i))^2}{a_i} + \frac{(b_i - e_i \cdot B(x_i,y_i))^2}{b_i}$$

$$+ \frac{(c_i - e_i \cdot C(x_i,y_i))^2}{c_i} + \frac{(d_i - e_i \cdot D(x_i,y_i))^2}{d_i}$$

where a_i, b_i, c_i, d_i = the measured output of each tube

$e_i = a_i + b_i + c_i + d_i$

$A(x_i,y_i), B\ldots$ = the predicted relative light outputs

from the model given trial values of the four parameters

The error on each measurement is $\propto$ square root of the tube output.

By minimizing the χ^2 sum over all events for each counter, we obtained attenuation lengths and centers. It should be noted that a fiber optics flasher system

was used in situ to equalize the gains of the four tubes by noting the response of the tubes to a flash of light in the center of the counter throughout the running period (details of this system can be found in reference [LE81]).

As a check on this procedure we took hadron beam data at various points in one of the neutrino target carts. The output relative to the center before and after correction are plotted in figure 3-4 along with a contour map showing profiles of equal correction versus position for a typical map.

As mentioned above the relative phototube gains were tracked throughout the running using a flasher reference system (basically a set of spark gaps and fiber optics to transmit the light to the center of the counters). In order to correct for week to week and month to month variations in counter outputs, we averaged the pulse heights from muons which traversed within 30" of the center of each counter from about .1 to 2 times minimum ionizing pulse height. This average was used to define the average minimum ionizing pulse height and set the scale for all calculations using the counter information. These averages were computed using neutrino and straight through muon data and were updated on approximately a weekly basis (the reproducibility and temporal drift are demonstrated by figure 3-5). Finally, to insure that there was no counter to counter bias induced by low pulse height ADC non linearities, we set an overall scale for each counter

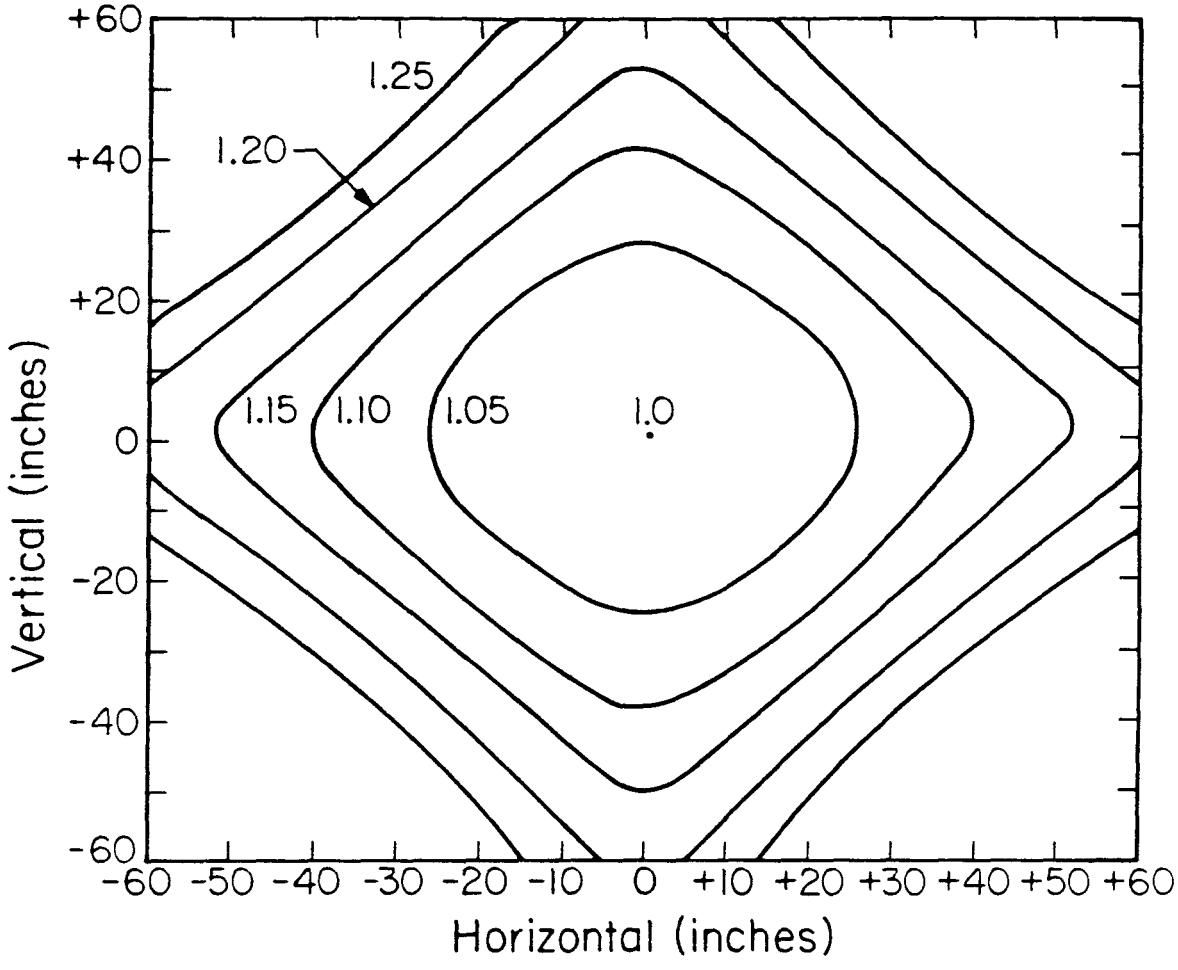

Figure 3-4a: Counter map. The contours of equal correction are plotted for a target counter.

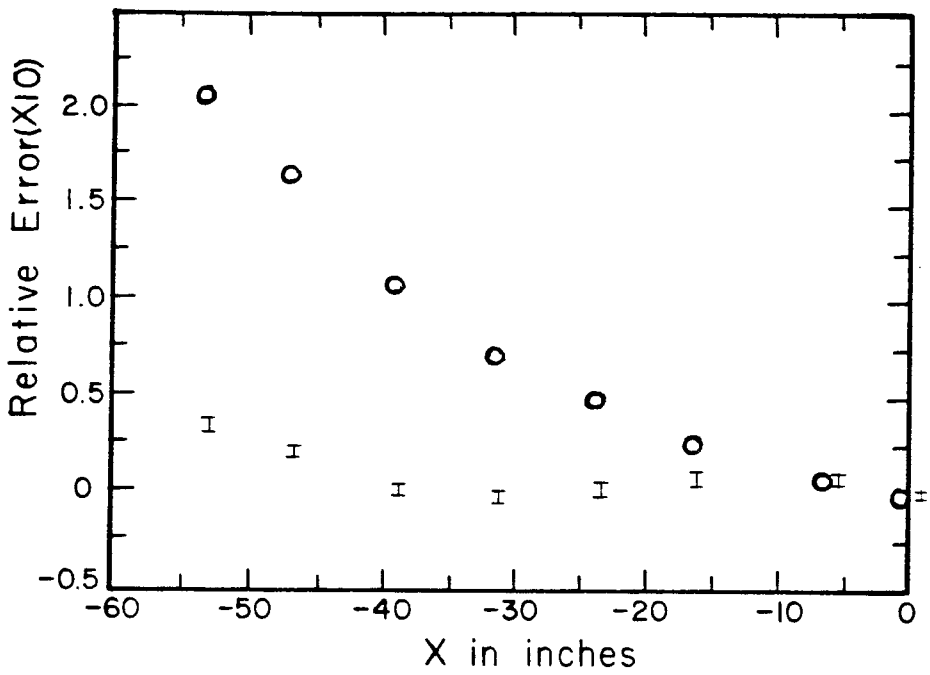

Figure 3-4b: Counter map. The circles show the difference between true and measured hadron energy without any map correction. The other points are the same quantity after map correction. The data are from hadron beam runs.

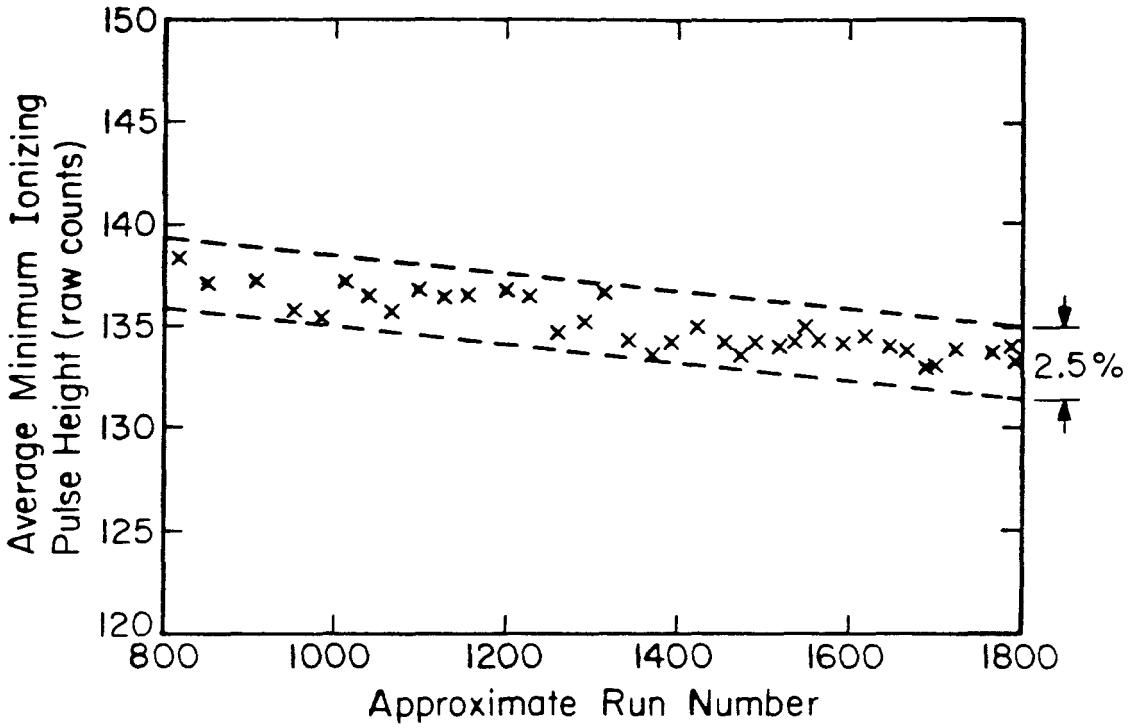

Figure 3-5: Counter gain stability. The plot shows average gain of all target counters versus time (expressed as approximate run number). The ordinate is obtained by observing the pulse height from muons traversing within 30" of the center of the target.

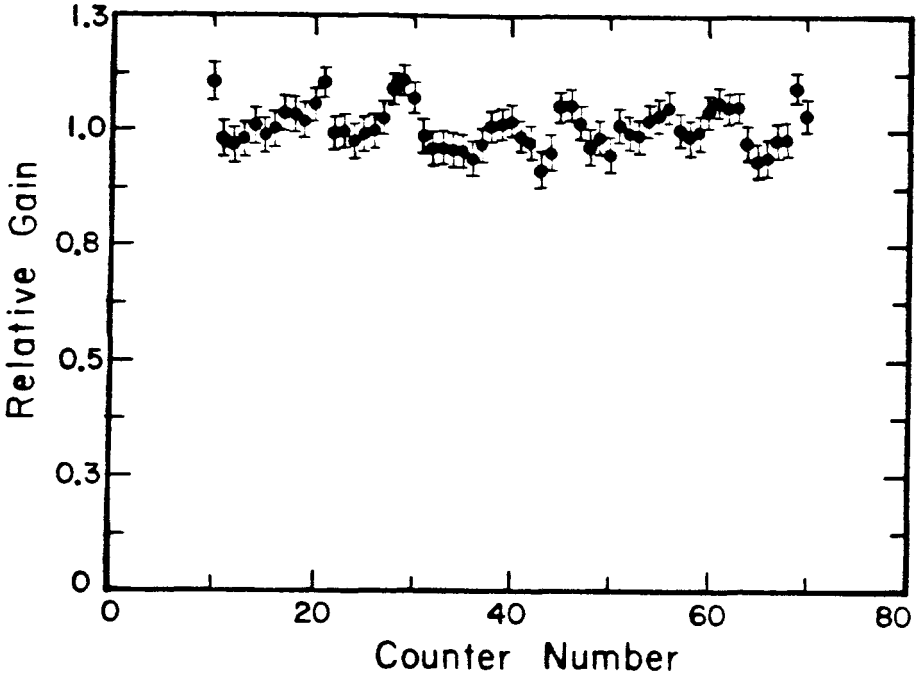

Figure 3-6: Relative gain of target counters. The counter to counter gain was adjusted to equalize the mean energy sampled in neutrino events (for the ensemble of events chosen, hadron energy was unbiased in z). The plot shows the relative gain determined in this way.

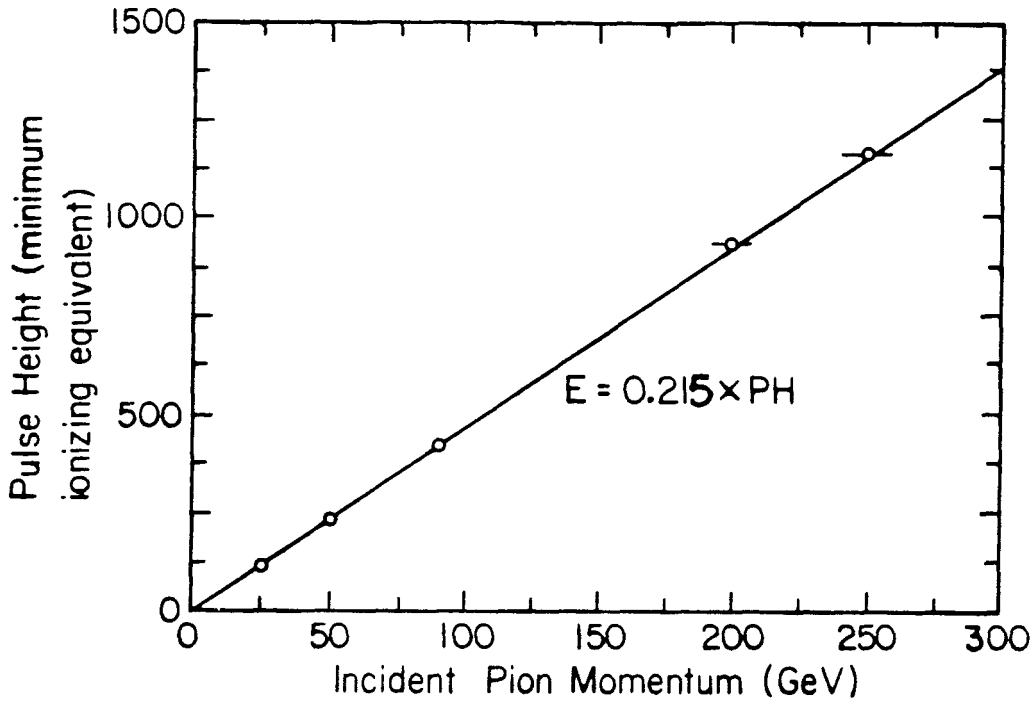

Figure 3-7a: Hadron energy response. The response of the target to hadron showers was calibrated with a pion beam. The total output is plotted versus incident momentum above.

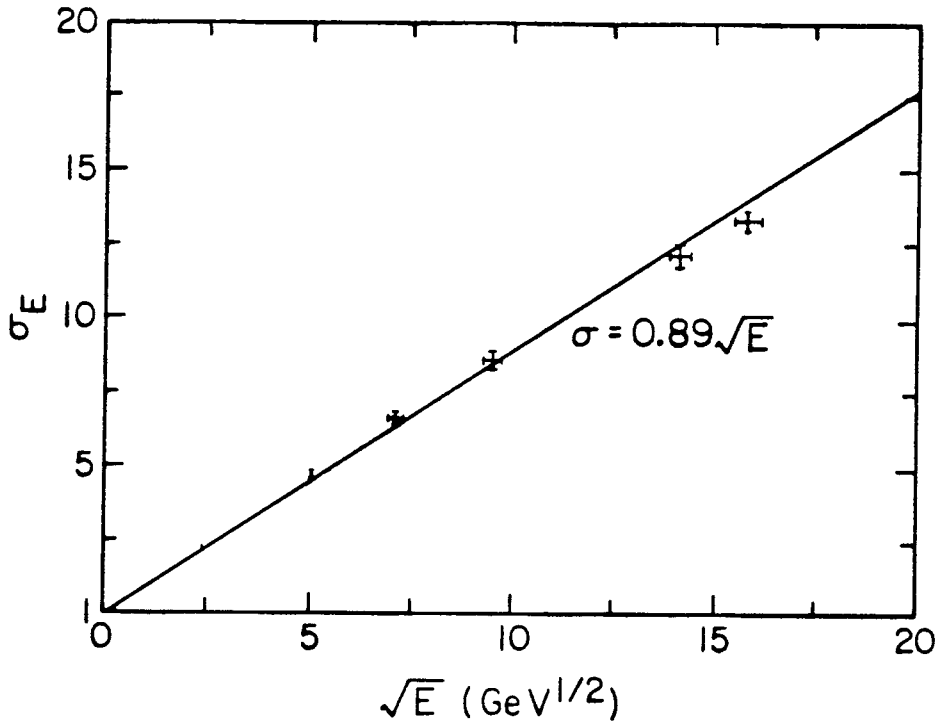

Figure 3-7b: Hadron energy response. The hadron energy resolution of the target was measured with a pion beam. The r.m.s. spread in measured hadron energy is plotted versus the square root of the incident beam energy above.

by averaging the pulse height from hadron showers for an ensemble of events for which there was no counter to counter bias. A gain was evaluated for each counter to force these averages to be equal (see figure 3-6 for a plot of the gain factors versus counter).

3.3.3. Hadron Energy Calibration and Resolution

In order to convert shower pulse heights to energy in GeV, we took hadron beam data at several energies in the Fermilab N5 line. After making all the corrections listed above to the pulse heights for the first and second target carts, we calculated the average and width of the pulse height distributions in terms of minimum ionizing for showers produced by hadrons hitting the center of target cart 2. The pulse height is linear with respect to hadron energy with

E(in GeV.) = .215· (pulseheight in times minimum) and the resolution is given by $\delta E_h = .93 + .78\sqrt{E_h}$ (constraining δE_h to go through 0 at $E_h = 0$ gives $\delta E_h = .89\sqrt{E_h}$).

3.4. Trigger Electronics

For the charged current events we had two triggers. The triggers were designed to be electronically independent, and to overlap substantially while covering each other's blind spots. This facilitated efficiency measurements by comparison of the two, and enabled coverage of a large acceptance region without an unduly complicated trigger.

3.4.1. Muon Trigger

The muon trigger was designed to get events with a muon produced at a small angle with respect to the interacting neutrino. The trigger required a hit in T2 (a trigger counter between the first and second toroid carts) and hits in at least two target counters among the first four along with hits further upstream in the target or downstream in the toroid (see figure 3-8 for a logic diagram). This provided events with low hadron energy but missed events where the muon does not pass through the toroidal magnetic field.

3.4.2. Penetration Trigger

The penetration trigger was designed to get events where the muon is produced at a wide angle. It required that more than sixteen target counters fire and that the overall pulseheight exceed a level that corresponds to about a 4 GeV. shower (see figure 3-10). This trigger picked up events with a muon penetrating more than 1.6 m. of steel and with a hadron shower of greater than 4 GeV. It, of course, missed low hadron energy events ($E_h < 4 GeV.$).

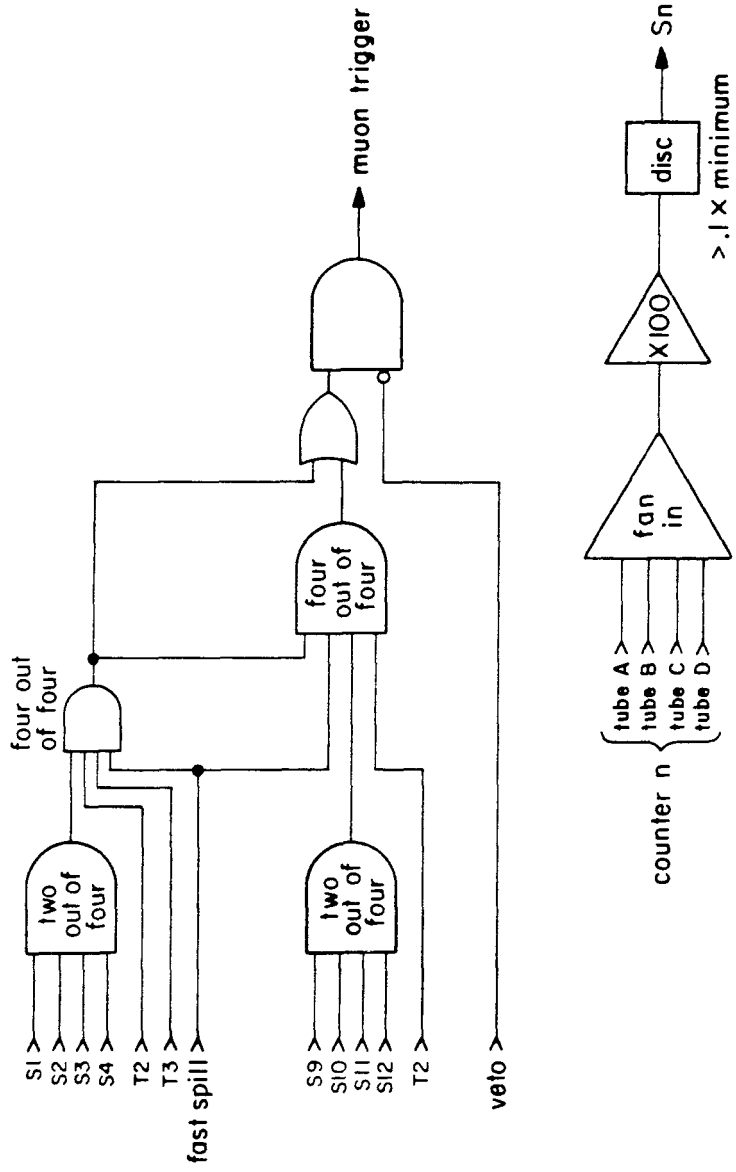

Muon Trigger

Figure 3-8: Muon trigger logic. In the above: veto refers to the or'ed output of a wall of veto counters in front of the detector, T2 and T3 refers to the output of trigger counters in the toroids, and fast spill is the output of a discriminator on a proton intensity monitor.

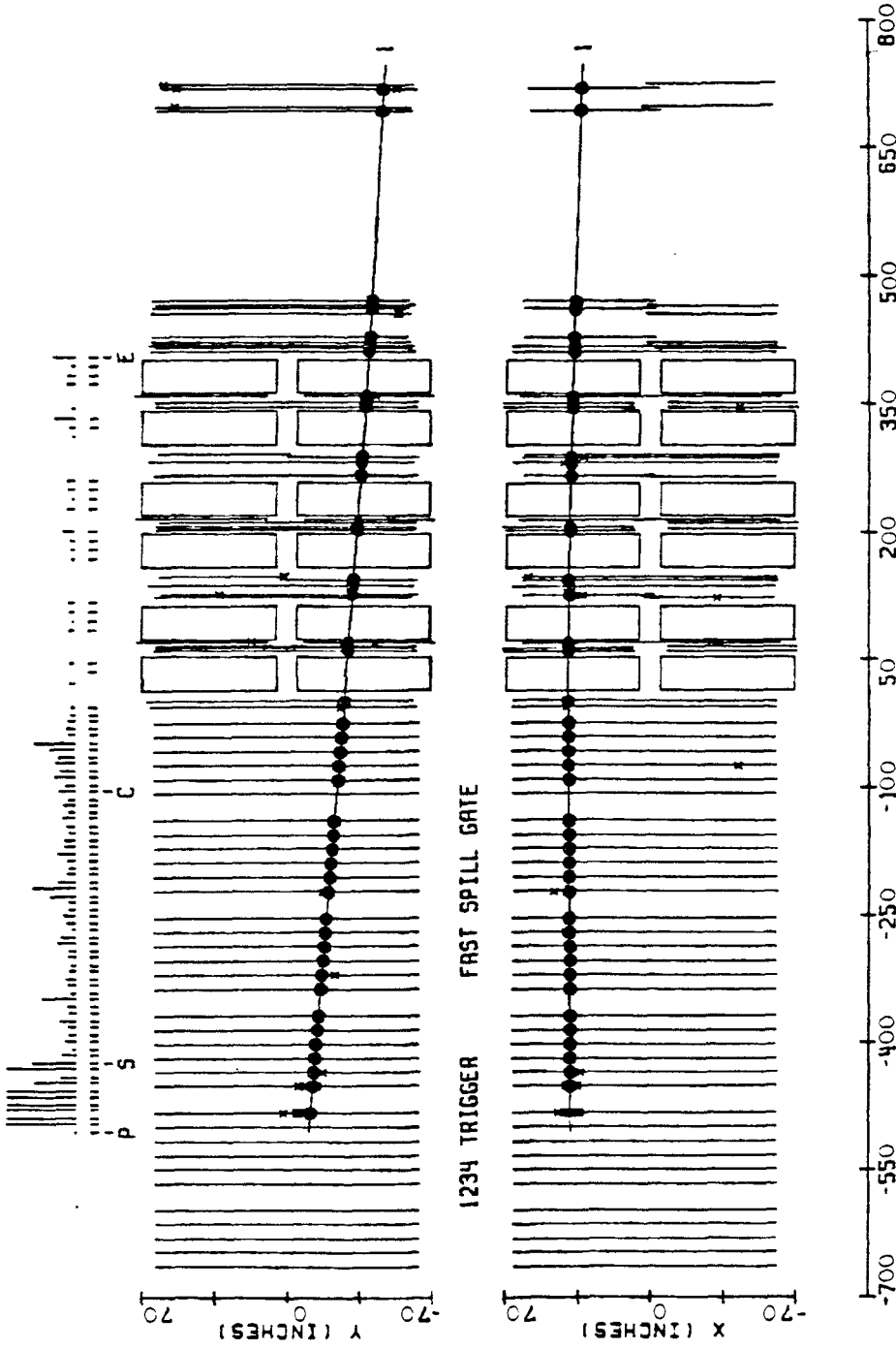

Figure 3-9: Muon trigger event. A muon trigger event after computer reconstruction. The circles are sparks identified as being on the muon track. The x's are sparks unassociated with the muon. The solid line is the reconstructed trajectory. Above the views of the apparatus is a bar graph of the counter pulse height.

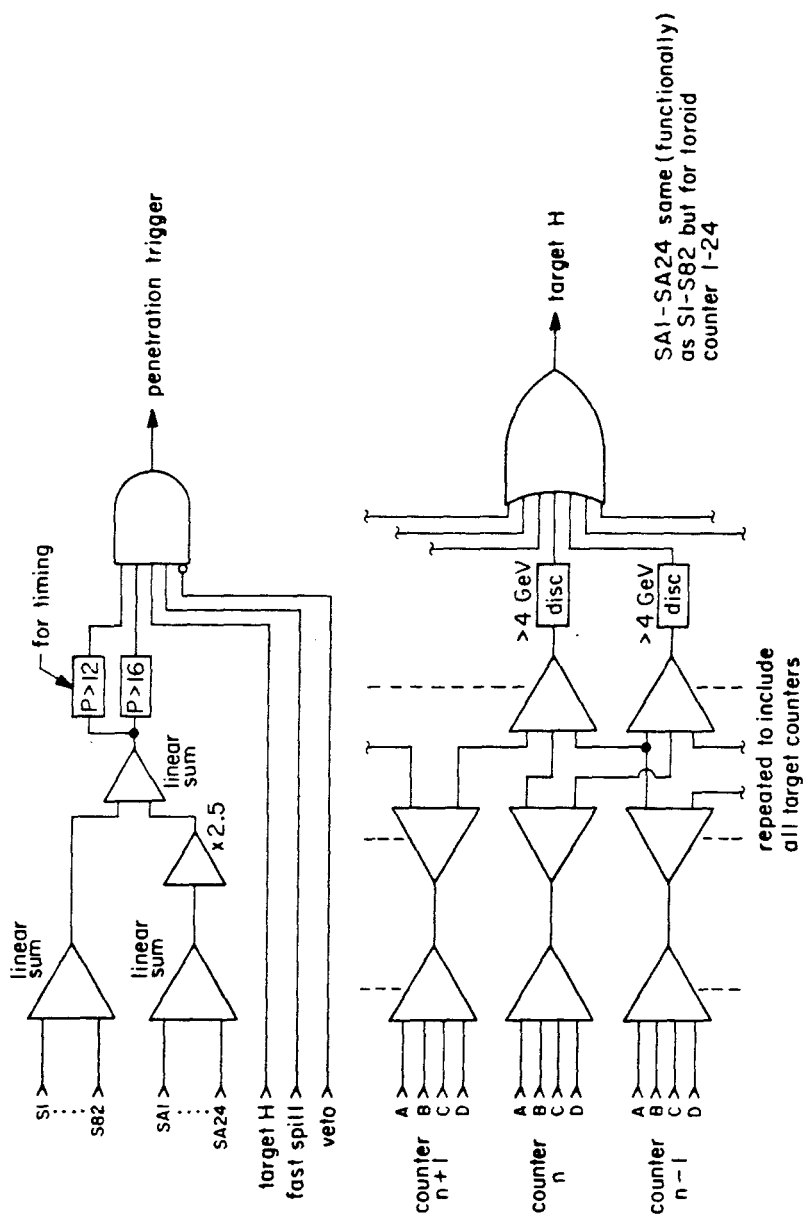

Penetration Trigger

Figure 3-10: Penetration trigger logic. In the above, P>12 and P>16 are discriminators with thresholds set to fire if more than 12 or 16 target $'s are on respectively. For the definition of veto and fast spill see figure 3-8.

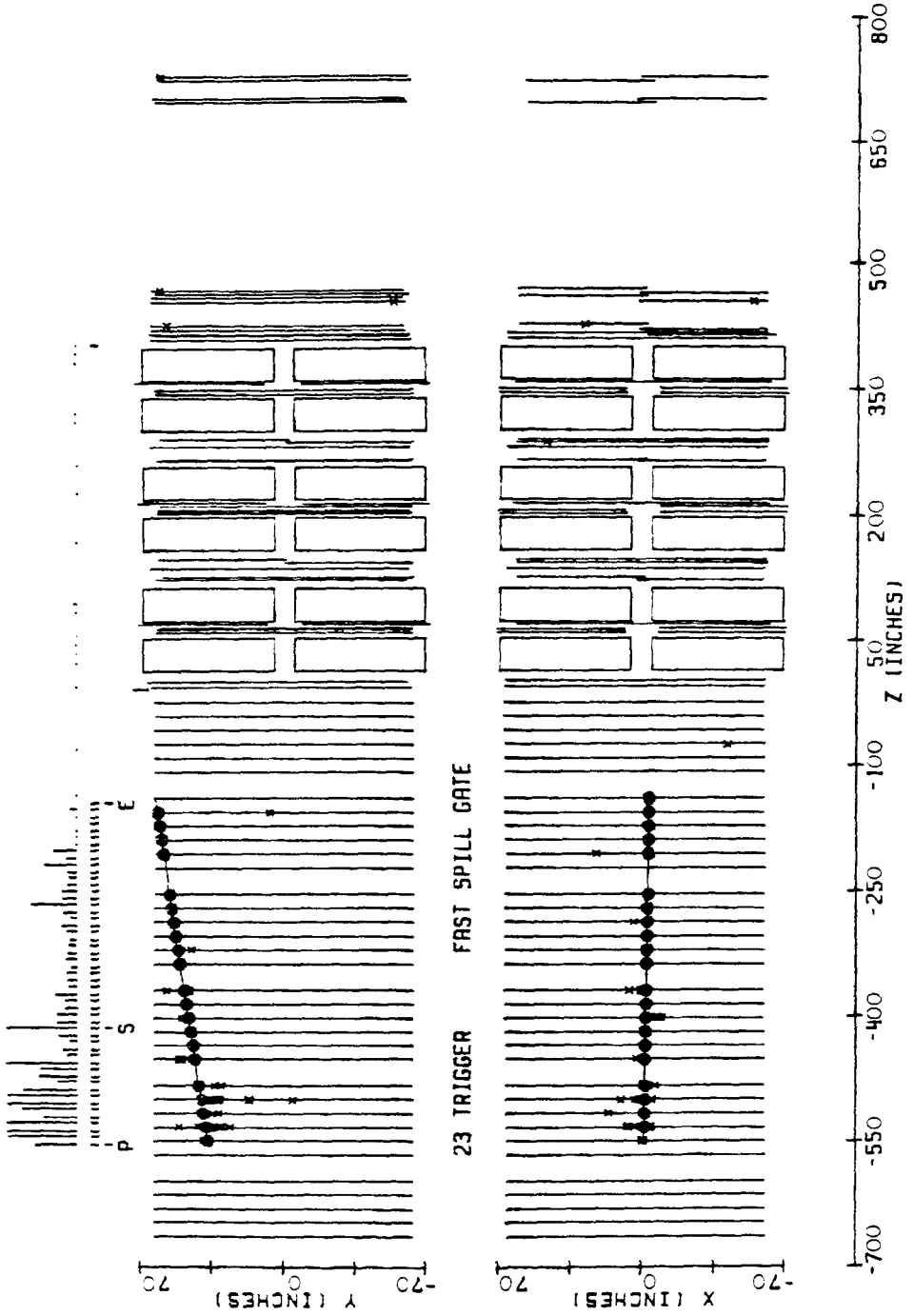

Figure 3-11: Penetration trigger event. Computer reconstructed penetration trigger event (for a description of the display conventions see figure 3-9).

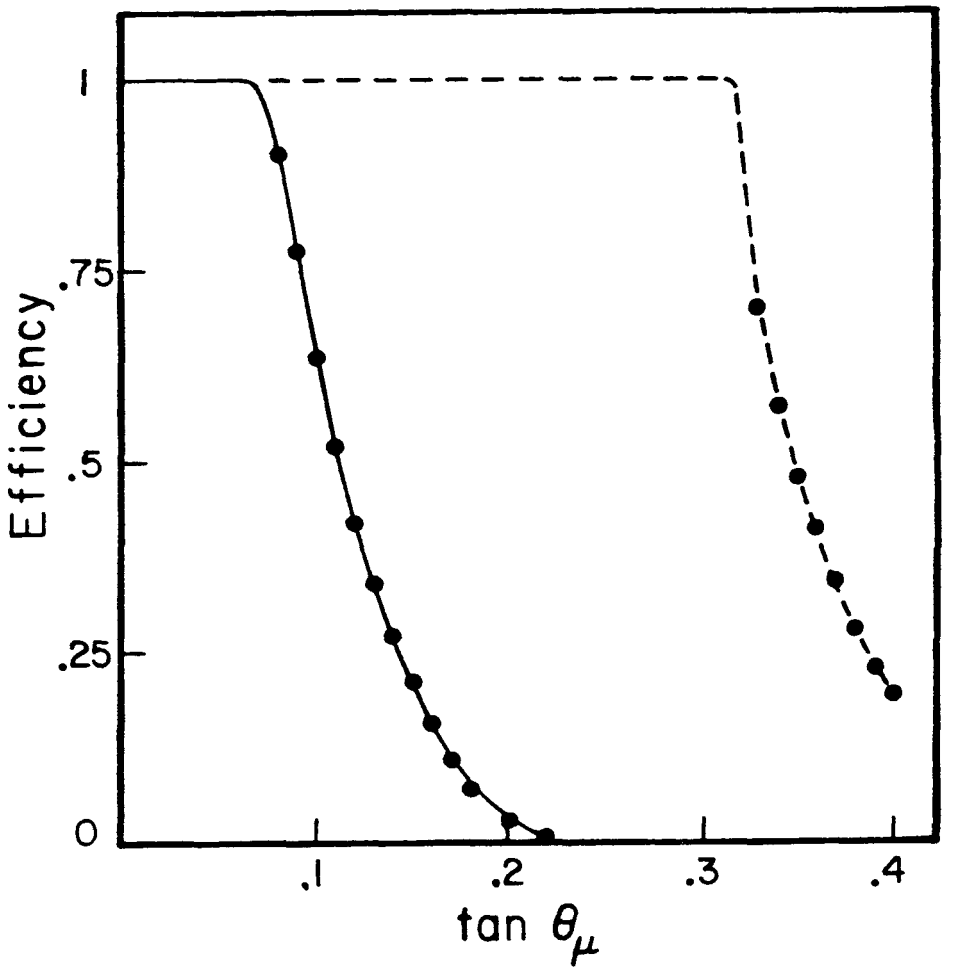

Figure 3-12: The efficiency of the muon and penetration triggers after all software cuts (see section 5.1). The dashed curve is for penetration events; the solid line is for muon events. The event vertex is assumed to be at x = y = 0 (x and y are transverse to the beam). For the muon trigger plot the efficiency is averaged along the fiducial volume in z (the beam direction).

4.Event and Monitor Analysis

4.1.Cuts on Events

4.1.1.Unanalyzable events

Each event was computer reconstructed to yield the event vertex, E_h, Θ_μ and where possible p_μ. Throughout the running there were occasional events that defied analysis, either due to instrumental inadequacies or because of unusual event topologies (e.g. ADC's were saturated or a cosmic ray air shower caused scattered hits throughout the apparatus). In order to avoid using these events, a set of algorithms was devised to eliminate such events without compromising good neutrino data.

These cuts break down into four categories. The first class of cuts, by far the easiest to deal with, are the fiducial cuts. Events were thrown out early if they did not fall within an extended fiducial volume for which the track finding was reasonably efficient and the hadron calorimetry would not suffer seriously from leakage of charged particles out of the sides of the calorimeter. This required that events occur in the target with event vertex more than 171" from the front of the first toroid cart and within 55" horizontally and vertically from the center of the target. The second class of events included those cases where some instrumental failure made hadron energy calculation impossible. The third category was composed of events that could not be identified from the counter information as having a single neutrino interaction. Almost all of these events were cosmic rays where several sections of the target were hit by particles originating from a shower in the atmosphere above the apparatus. After subtracting cosmic rays the last two categories account for less than 1% of the events used in the analysis.

4.1.2. Events with Improper Track Reconstruction

The final class of events that were thrown out were those events for which track reconstruction failed. The vast majority of these events were cases where the momentum could not be obtained. The fit to sparks in the toroid chambers used the method outlined in reference LE81 . This method was a χ^2 minimization technique that included correct handling of the full error matrix which includes the correlations, due to multiple scattering, of the residuals in each chamber. The method failed on some events in the sense that the track found had a very high χ^2 (we rejected events with χ^2/degree of freedom > 9) or the minimization technique used was unable to find a minimum in χ^2 as a function of p. These events were eliminated as muon triggers but, if they fired the penetration trigger, were still used as if they had been penetration triggers that did not fire the muon trigger.

4.1.3. Scan Results

In order to estimate the event losses due to the above cuts, we scanned a random sample of good (retained) and bad (eliminated) events (about 1000 events total were scanned). Excluding the toroid track finding requirements, we find that a true neutrino event inside the fiducial volume would pass the above requirements 99.4±.3% of the time,, that .8±.3% of the events had no visible muon track and could have been neutral current events with penetrating showers, and that .2±.2% of the events were improperly reconstructed and should not have been accepted, yet made it through to the final sample. The loss or gain of events was less than 1% and was not considered significant (i.e. no correction was made).

While the events were scanned, any event that appeared to be mishandled by the track finding routines was manually fixed. This gave us a set of events for

which we knew the true muon momentum and also the original uncorrected estimate of the momentum. These events were used to evaluate the extent to which the toroid track finding cut was biased in momentum. A plot of the efficiency for passing this cut versus true muon momentum as the muon enters the toroid appears in figure 4-1. The efficiency is flat down to about 20 GeV. where it starts to fall off. Because the method used to construct the cross sections and y distributions uses penetration triggers for high y events (p_μ is small), the effect of this fall off in efficiency at low momentum is extremely small. A simple parameterization of the shape of the efficiency versus p_μ of the form $\alpha(1+.0196\cdot(p_0-18)\Theta(18-p_0))$ was used to correct for lost muon triggers (p_0 is the momentum evaluated at the front face of the first toroid). The scale of this correction (α) was fixed independently for each momentum setting by comparing the number of penetration triggers versus the number of events lost due to the cut, for events which should have satisfied both triggers (see figure 4-2).

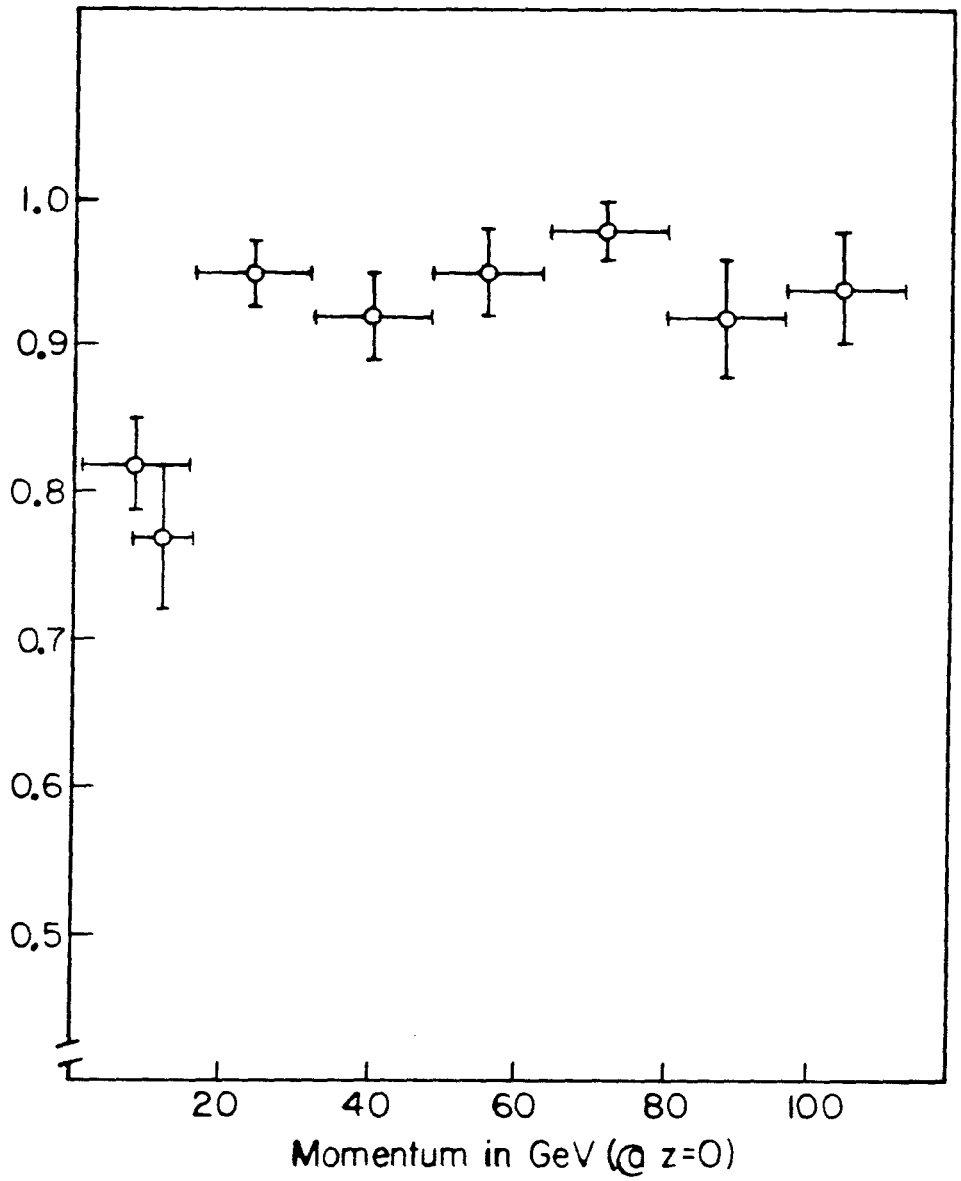

Figure 4-1: Track reconstruction efficiency versus momentum. The dependence of muon momentum reconstruction efficiency on momentum was determined by "fixing" events the computer misanalyzed. The number of events that the computer successfully reconstructed over the total number of events is plotted above versus the "fixed" momentum at the toroid front face.

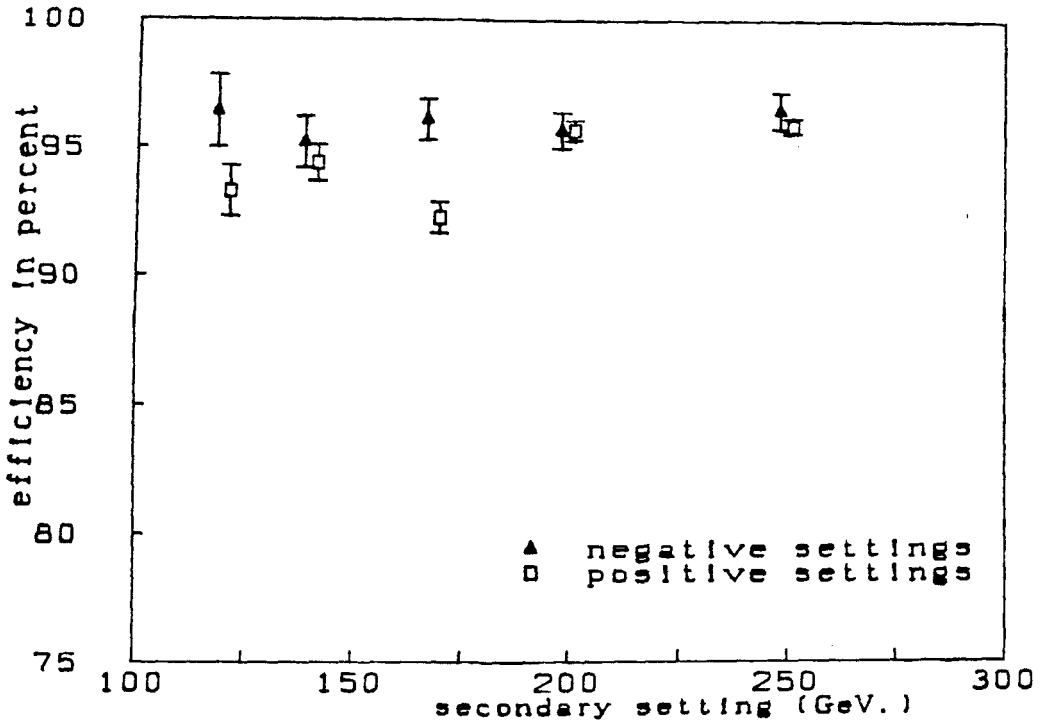

Figure 4-2: Muon momentum reconstruction efficiency versus setting. The average momentum reconstruction efficiency (after correcting for the muon momentum dependence of this efficiency) is plotted for each of the 10 secondary settings.

4.2. Monitor Cuts (applied to monitors and events)

In order to keep beam conditions stable and to avoid washing out the dichromatic nature of the neutrino beam by missteering of the secondaries, throughout the running, we maintained the secondary beam direction by compensating for changes in main ring proton extraction with two dipoles in front of the production target. The beam direction was assessed by two SWICs in the decay pipe and a pair of split plate ion chambers. The split plates were housed in the same cans as the intensity monitoring chambers. This procedure was done manually and occasionally spills were missteered or of very low intensity. These cycles we eliminated from the analysis by making cuts on the split plate ratio for the manhole ion chamber and on the beam intensity recorded by the manhole ion chamber. Both the monitor information and any events in these

cycles we eliminated from the final analysis. The steering tolerance used corresponded to fixing the neutrino beam center to remain inside a box of 2.4" on a side at lab E.

4.2.1. Ion Chamber Selection

A careful study of how well the various monitors of secondary and primary (protons on target) intensity tracked each other was carried out by Taka Kondo of FNAL. A cross comparison was made of the two ion chambers and their various plates. When one of the total intensity plates did not agree well with several other measures of secondary intensity it was considered unreliable. Mostly both ion chambers agreed well and their average was used. Runs were eliminated in cases where the monitoring stability was uncertain.

5. Expectations Versus Results

5.1. Cross Sections

5.1.1. Method of Counting Events

The cross section slope is given by the expression

$$\frac{\sigma}{E} = \frac{N^{ev}(r)}{F_\nu(r)E_\nu(r)N_{nuc}}$$

where N^{ev} = number of events for neutrinos from pi or ka decays in the target with vertex in region r corrected for geometric efficiency and event losses

(where r designates an annular bin centered on the beam)

$F_\nu(r)$ = number of neutrinos of a given type

$E(r)$ = average neutrino energy

N_{nuc} = number of nucleons/unit area

The average neutrino energy and neutrino flux per secondary are evaluated by using "decay turtle" to calculate the phase space of secondaries in the decay pipe and then folding in decays. The Monte Carlo used to calculate mean energy and neutrino flux was checked against measured quantities and in cases where it was deemed appropriate, adjusted to agree with measurements made while we were running. For a more detailed description of what was adjusted and how the level of agreement was used in evaluating the systematic error see appendix 1.

The number of nucleons per unit area was obtained by taking the known mass of the target steel (each plate was weighed before installation) and an estimate of the additional mass due to scintillion counters and chamber material (amounting to 7% of the target mass) in the fiducial volume and combining with

Avagadro's number to yield $3.14x10^{27}\frac{nucleons}{cm^2}$

The event count must include a correction for finite apparatus acceptance and a method for separating events into those from neutrino's from pion and kaon decays. Two triggers were used which had very different acceptances. The "muon trigger" required that the muon produced in an interaction pass through a counter in the toroids (trigger counter T2) as well as several counters in the target. This trigger picked up events for which all kinematic quantities (E_h, p_μ, Θ_μ) could in principle be measured. The "penetration trigger" required a muon traversing sixteen counters in the target and a hadron shower exceeding 4 Gev. This trigger picked up events that exited the target and did not reach the toroid (for these events only E_h and Θ_μ can be obtained). Separation of pion and kaon decay neutrinos was possible for all events by exploiting the fact that, for large enough neutrino energy, the muon trigger was reasonably efficient out to large values of y (recall that $\Theta_\mu^2 \approx \frac{2mxy}{E_\nu(1-y)}$). This allowed us to use the muon trigger events for neutrinos from kaon decay from a hadron energy of zero up to a hadron energy beyond which there would be no events from pion decay.

In order to simplify the acceptance corrections each event is tested against a set of geometric conditions (see figure 5-1). These geometric conditions are more restrictive than the hardware trigger and act as a sort of software trigger. The "muon" and "penetration" events originate from independent hardware triggers and satisfy different geometric requirements. These requirements depend only on the muon angle from the z axis (taken to be along the beam direction), the azimuthal angle and the interaction point. Since muons will be produced uniformly in azimuthal angle, an efficiency for each event can be defined by finding

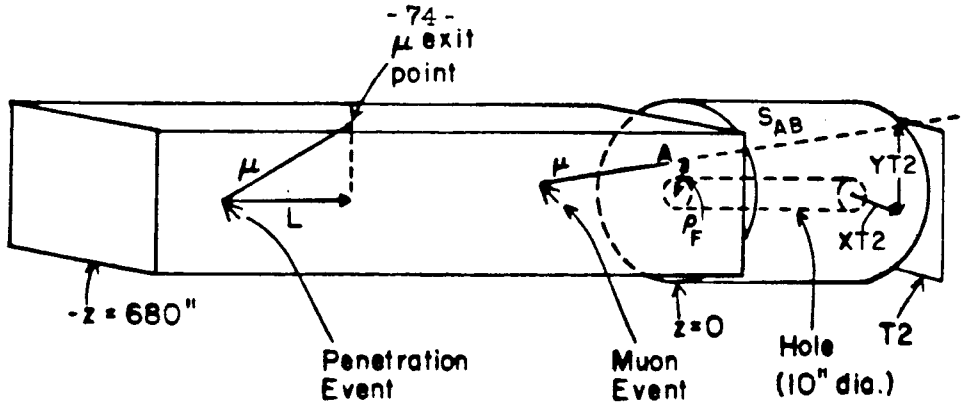

Muon Events	
quantity	cut
z position of vertex	-653" to -167" (-16.6m. to -4.2m.)
ρ_F	less than 69" (175.cm.)
|XT2| and |YT2|*	less than 55" (140cm.)
fraction of line segment S_{AB} inside hole	less than 30%
|X| and |Y| of vertex*	less than 55" (140cm.)

Penetration Events	
quantity	cut
z position of vertex	-653" to -167" (-16.6m. to -4.2m.)
L (penetration)	greater than 171." (435cm.)
|X| and |Y| of vertex*	less than 55" (140cm.)

*(X and Y coordinates are measured from the apparatus center)

Figure 5-1: Event cuts. The above cuts are made on the two classes of events in order to facilitate efficiency calculations. The line segment S_{AB} is a straight line projection of the muon track from the target to the end of the toroids (not shown).

the fraction of events that would pass the cuts as the event is rotated about z. The muon events have a different angular acceptance at different z positions in the target, but the number of neutrino events with a given muon angle cannot depend on z position. For muon events the efficiency is extended to include a translation of the interaction point along the z axis. This corrects for missing wide angle events far from the toroids by using wide angle events near the toroid face. In all sums the events are weighted by one over the efficiency. An overall angle cut is imposed on muon events. The penetration event hardware trigger includes a hadron energy threshold, so penetration events are used only if E_h is greater than 10 Gev. For muon angles below 100 mr. and E_h greater than 10 Gev. both triggers are efficient and a comparison can be made. Figure 5-2 shows the ratio of weighted events of the two types, demonstrating the consistency of the two weighting methods and also the limitations of the two types of triggers. An additional correction must be made to muon events to account for those cases where the momentum of the muon cannot be determined by the fitting program. This correction has been determined by scans to be 95% for most momenta, somewhat worse at low momenta (see section 4.1.3).

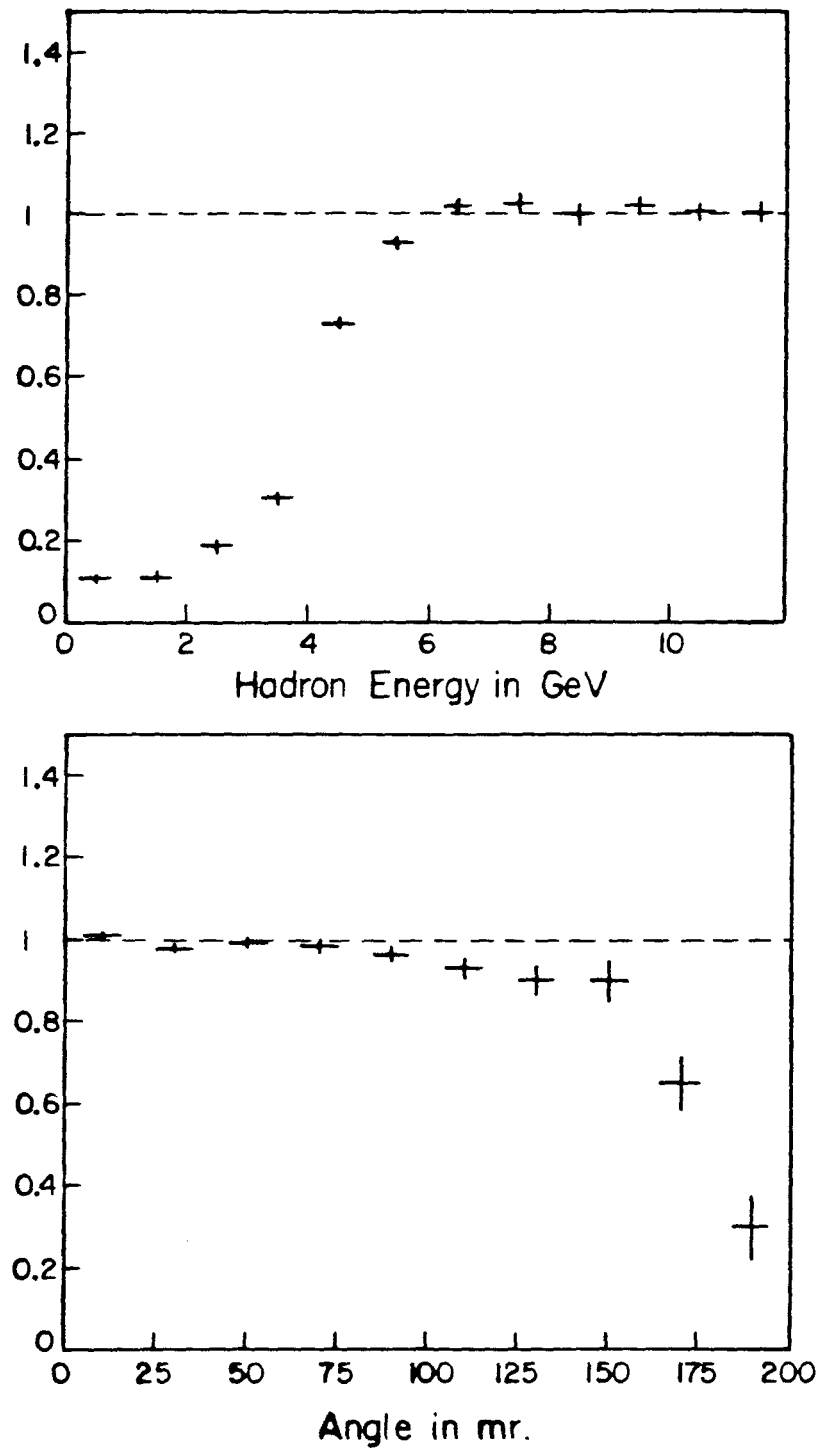

Figure 5-2: Comparison of muon and penetration events. The top plot is the ratio of penetration events to muon events versus hadron energy (for events with $\Theta_\mu < .1$). The lower plot is the inverse ratio versus Θ_μ (for events with $E_h > 10$ GeV.). In the overlap region ($\Theta_\mu < .1$ and $E_h > 10$ GeV.) the ratio of events is unity. Outside of this region each trigger has some limitation which leads to unsampled events which cannot be corrected for by event rotation around z.

Along with the cut on the maximum Θ_μ there are several other cuts imposed on the data, all on "physics" parameters (see table 5-1). A Monte Carlo calculation was used to correct for the losses imposed by these cuts; the Monte Carlo corrections are listed in table 5-2.

Table 5-1: Physics Cuts on Events

muon events	penetration events
$\Theta_\mu < .1$	$\Theta_\mu < .37$
$E_\mu > 10 GeV.$	$E_h > 10 GeV.$
for events with $R_{vertex} < 5 inches$ $\Theta_\mu > .0071$	$E_\mu > 2.9 GeV.$ (due to penetration cut)

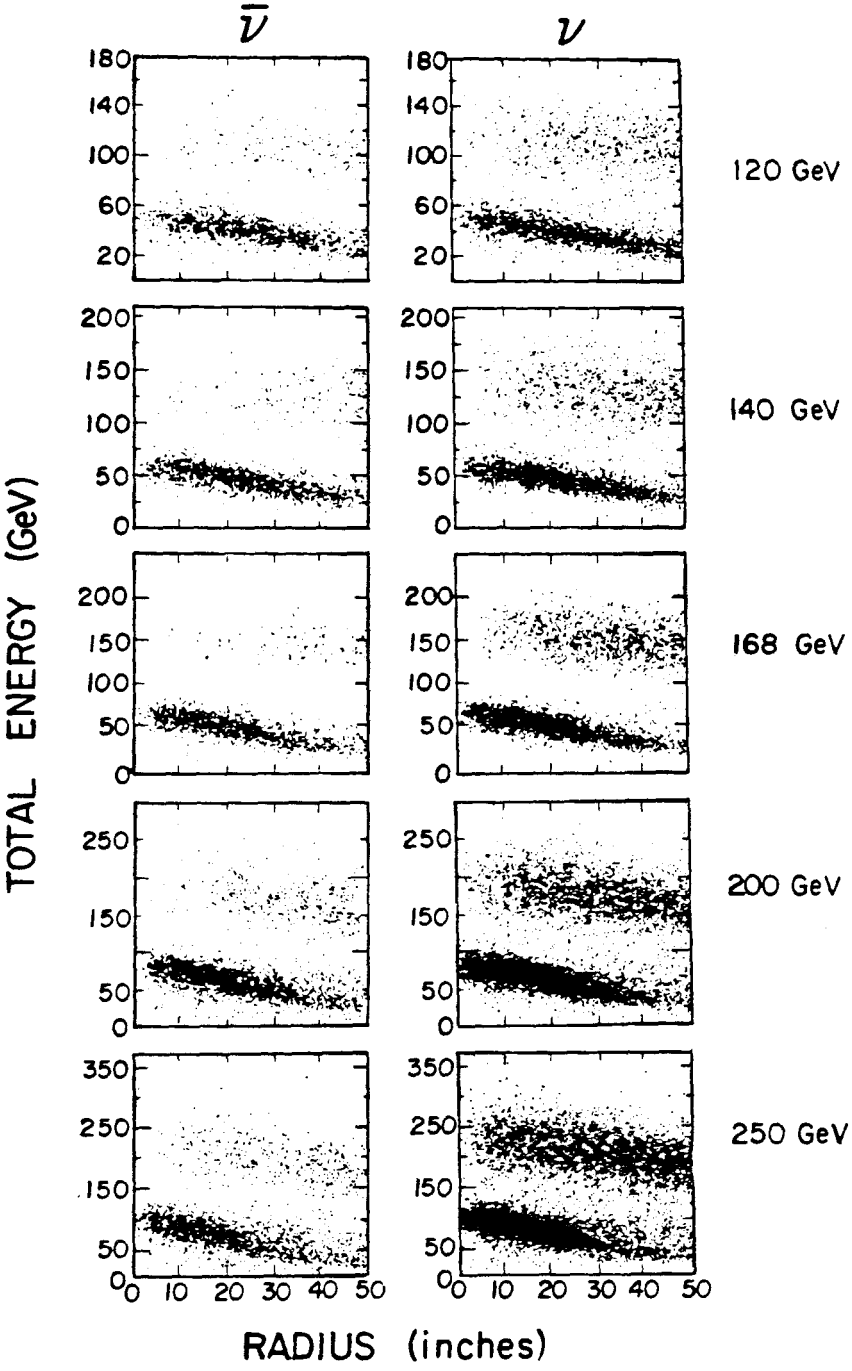

Figure 5-3: Energy versus radius for muon events. Plots showing the clean seperation in energy between events from pion and kaon decay neutrinos.

Table 5-2: Corrections and Backgrounds for Total Cross Section

	acceptance		$K_{\mu 3}\nu$'s		wide band ν's	cosmic rays
energy	pions	kaons	pions	kaons		
+120	9.6%	3.5%	.3%	.6%	2.8%	0%
+140	8.4%	3.0%	.4%	.7%	2.0%	"
+168	7.4%	2.5%	.6%	.6%	2.6%	"
+200	6.0%	2.3%	.6%	.6%	2.2%	"
+250	5.4%	1.9%	.9%	.6%	2.7%	"
-120	3.7%	1.4%	.2%	.5%	3.9%	"
-140	3.7%	1.4%	.2%	.6%	4.0%	"
-168	2.8%	1.1%	.3%	.5%	4.7%	"
-200	2.1%	1.2%	.2%	.5%	6.4%	"
-250	2.1%	1.2%	.2%	.5%	15.7%	"

The cross section is calculated for each radial bin (5" annulus centered about the mean of the pion neutrino event vertex distribution) by dividing events into three regions of hadron energy. For the low hadron energy region (E_h < 10 Gev.) only muon events are used, since the penetration trigger would be inefficient for these events. Separation between events from pion and kaon decay neutrinos (referred to below as ν_π and ν_K) is done on the basis of total energy. The separation energy is defined by $E_s = \frac{\alpha}{(1+\beta^2 R^2)}$. The values of α and β are listed in table 5-3. Above a hadron energy of 10Gev. and below $.85E_s$ the number of ν_π events is determined by counting the total number of penetration

trigger events and subtracting the ν_K muon events with measured energy greater than E_s. Above this region, all penetration events are considered to be ν_K events; there are no ν_π events. Figure 5-4 includes plots of the number of events versus hadron energy with the three regions designated.

Table 5-3: Pion and Kaon fractions and separation parameters

	fraction of total beam		separation parameters	
energy	pions	kaons	α	β
+120	.5256±.0083	.0526±.0028	80	.0119
+140	.4176±.0062	.0472±.0021	92	.0126
+168	.2969±.0042	.0371±.0013	110	.014
+200	.1812±.0024	.0251±.0010	134	.0155
+250	.0718±.0009	.0118±.0007	165	.0177
-120	.876±.014	.0650±.0034	80	.0119
-140	.898±.013	.0607±.0027	92	.0126
-168	.920±.012	.0560±.0020	110	.014
-200	.934±.011	.0434±.0019	134	.0155
-250	.966±.011	.0339±.0018	165	.0177

There are three sources of background. There are cosmic ray events,

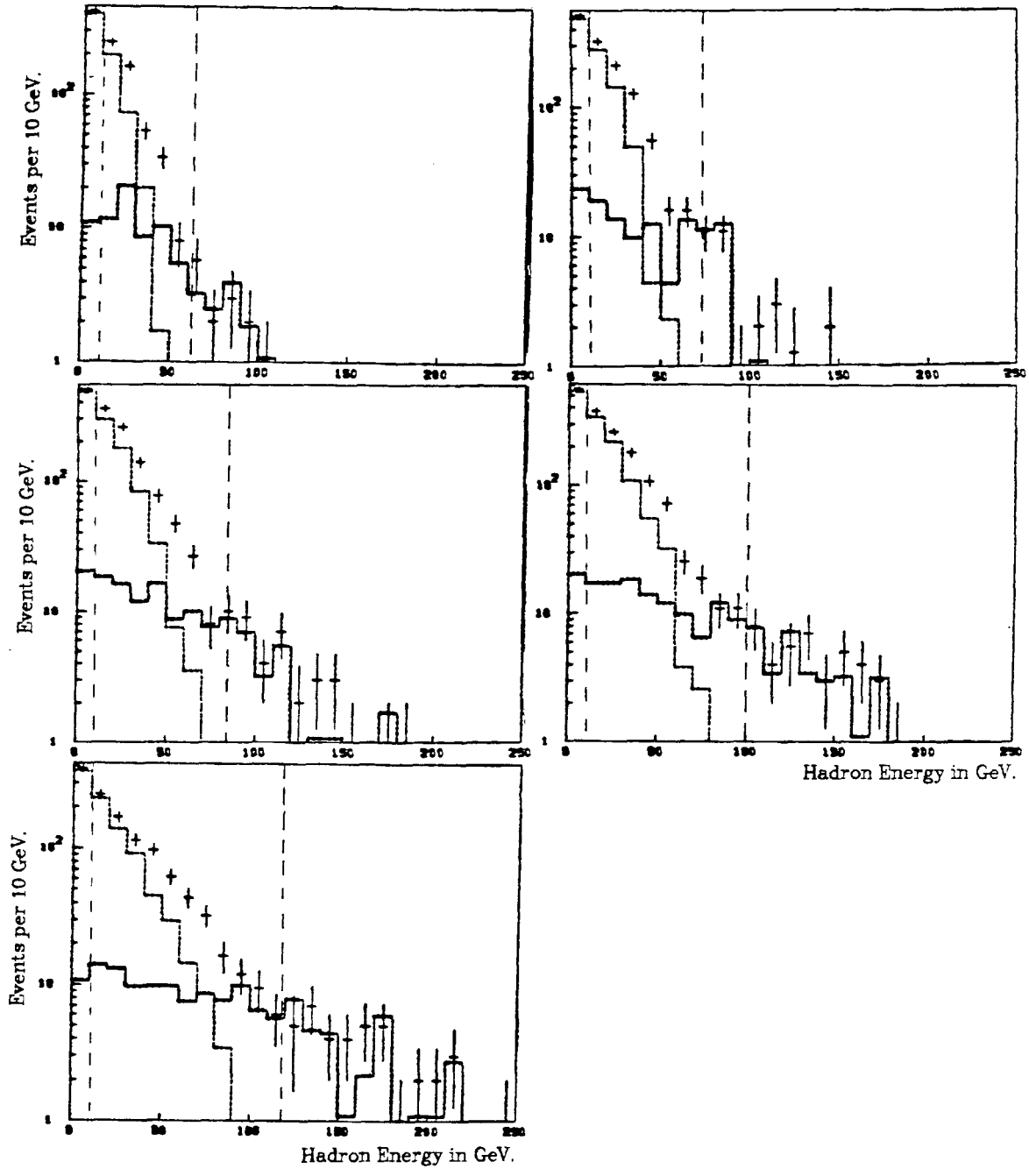

Figure 5-4a: Events versus hadron energy. The three regions in hadron energy are designated above by dashed vertical lines. Depicted are:
crosses - E_h < 10 GeV all muon events , E_h > 10 GeV all penetration events
dashed histogram - pion decay muon events
solid histogram - kaon decay muon events
From right to left, top to bottom we have the -120 GeV through the -250 GeV settings.

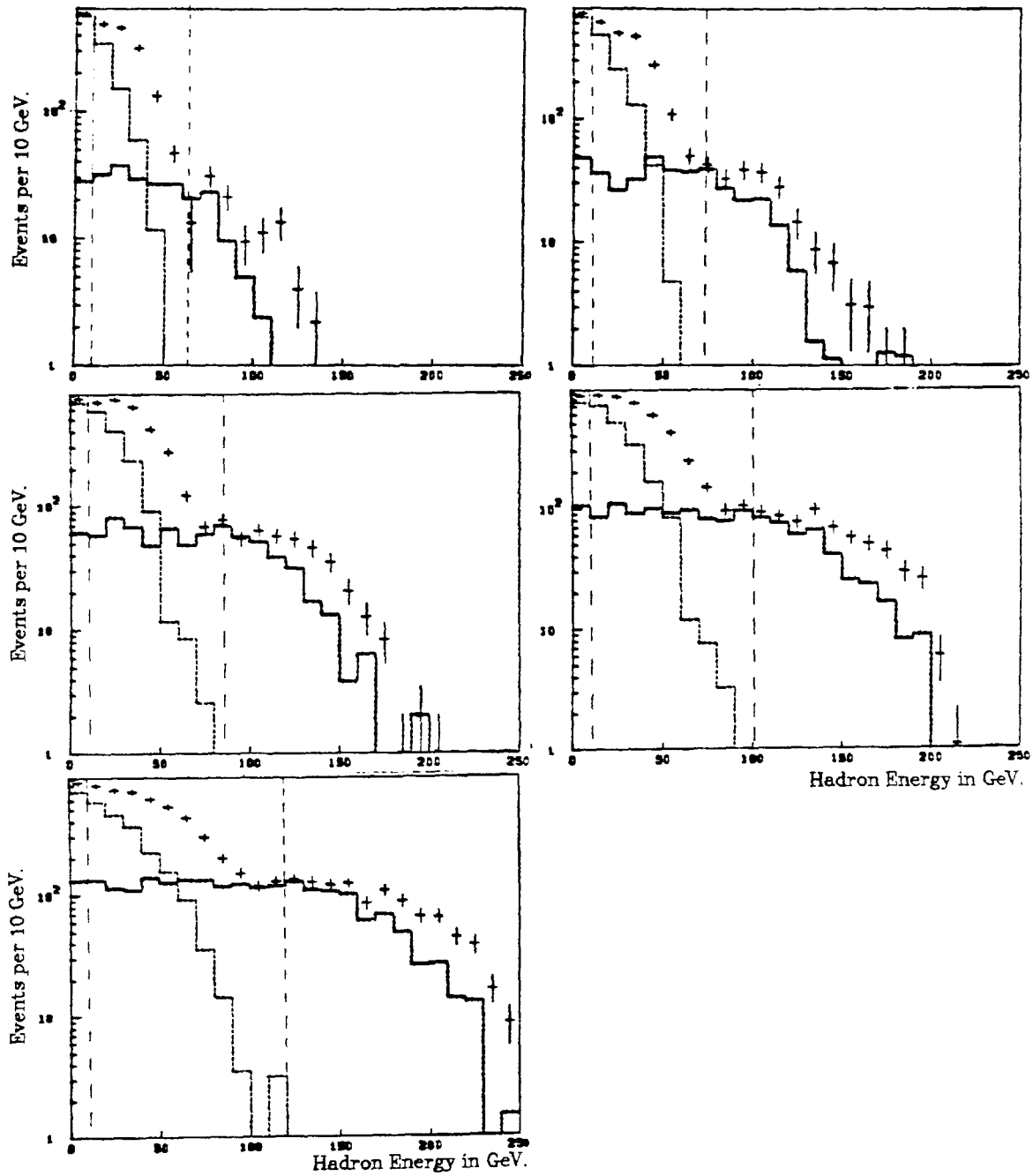

Figure 5-4b: Events versus hadron energy. The same as figure 5-4a for +120 GeV through +250 GeV settings.

events produced by ν's originating upstream of the decay pipe and events produced by K_{μ_3} decay. The cosmic ray rate is measured by taking triggers for 10 ms. between beam pulses (compared to the 1 ms. duration of the beam). The number of events due to upstream decays is determined by running with the momentum collimating slit closed (just in front of the entrance to the decay pipe). For negative settings, since the proton dumping does not change with momentum setting, the upstream decay, or closed slit background, is considered to be independent of setting. For all settings the "closed slit" background is assumed to scale with the solid angle subtended at the neutrino target. The consistency of these two expectations with the data is demonstrated in figure 5-5. Finally, the background due to K_{μ_3} decays is calculated using the same Monte Carlo that gave the neutrino flux. The level of all three backgrounds is listed in table 5-2.

A correction is applied to the cross sections to account for unsampled regions in x and y ($\frac{Q^2}{2m\nu}$ and $\frac{E_h}{E_\nu}$) using the model x and y distributions of reference DE79a (see table 5-2, the column labeled acceptance). In addition the neutrino cross section is multiplied by a factor of .979 and antineutrinos by 1.014 to compensate for the neutron excess of iron and yield cross sections for an isoscaler target.

5.1.2. Cross Section Results

After constructing cross sections for each 5" radial bin and each energy setting, the results are averaged over regions of energy. These averaged cross sections and an indication of the range of mean neutrino energy used (mean within a 5" bin) are listed in table 5-4 and plotted in figure 5-7.

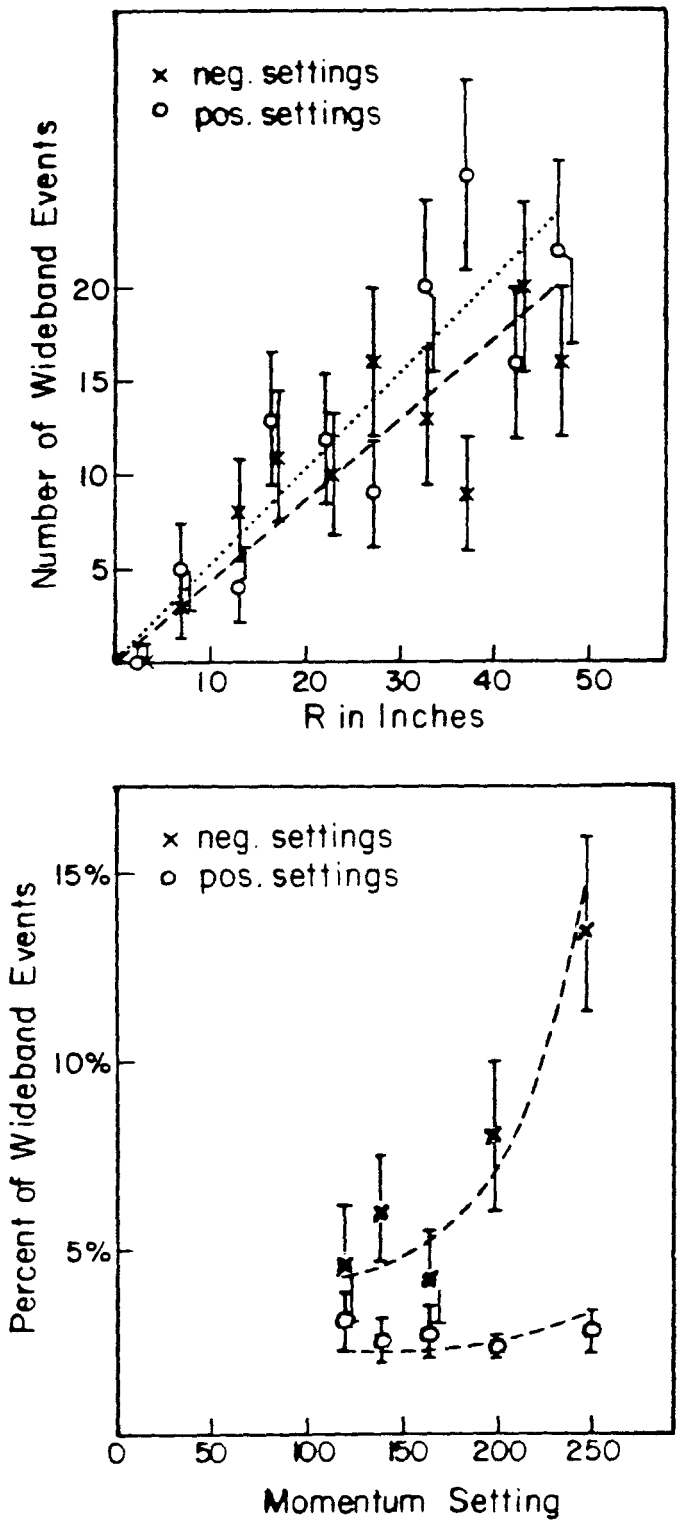

Figure 5-5: Wideband (or closed slit) events versus radius and setting. The data are plotted along with the assumptions that: upper plot: the number of wideband events is proportional to the area from which events are collected (dotted line positives - dashed negatives) lower plot: the number of wideband events is proportional to the number of protons on target regardless of the setting.

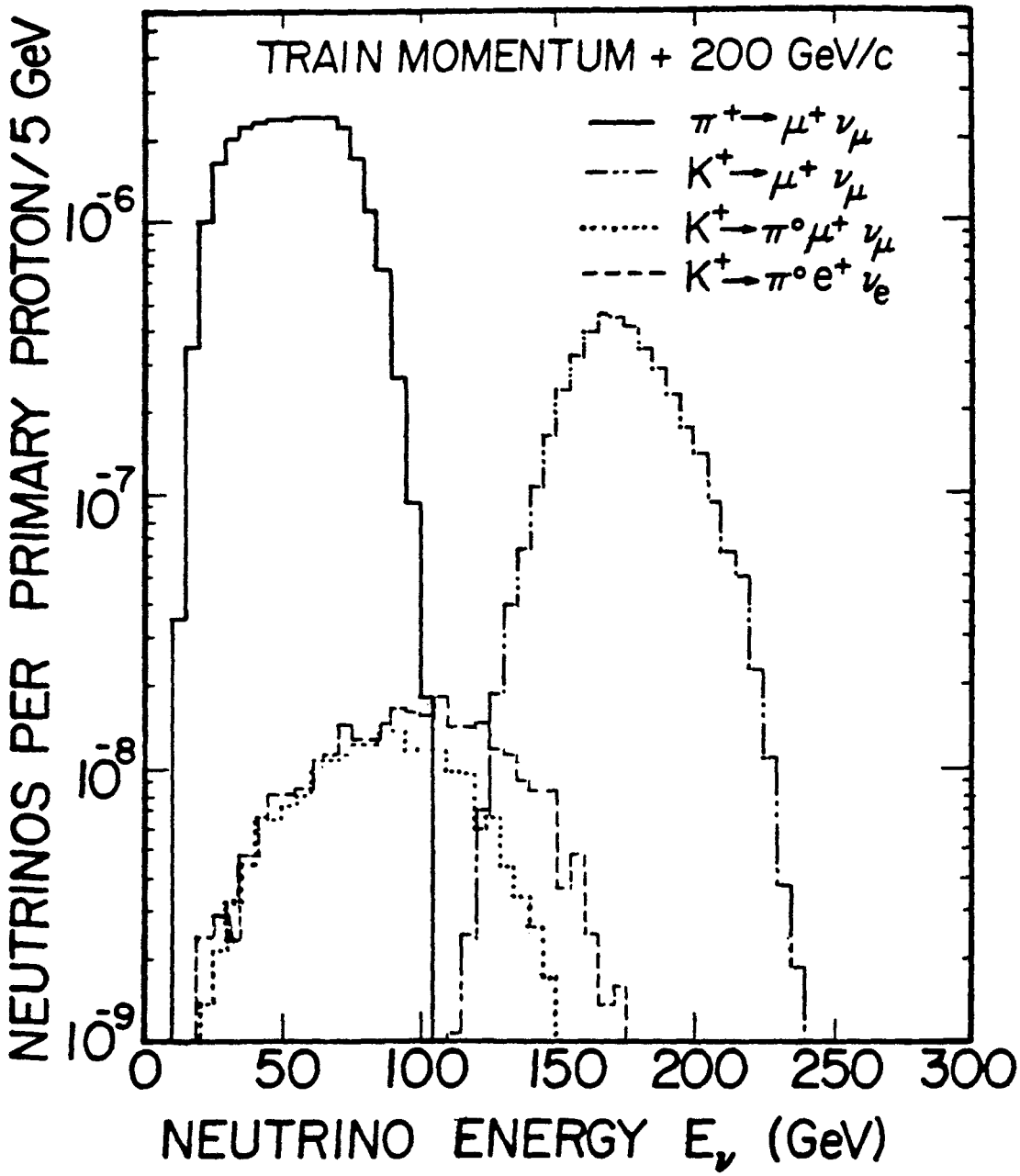

Figure 5-6: Three body decay backgrounds. The neutrino flux from kaon three body decays are depicted along with the flux of neutrinos from two body decays.

Table 5-4a: Neutrino and Antineutrino cross sections

Neutrinos

(errors below do not include an additional 3.6% common scale error)

E_{lo}	E_{hi}	E_{av}	$\frac{\sigma}{E}(10^{-38}cm^2/GeV)$*	χ^2	n_{df}
33.70	39.30	37.07	.6782+-.0133+-.0199	.169	2
41.80	49.40	44.69	.6649+-.0104+-.0211	2.540	2
50.20	57.10	53.97	.7135+-.0088+-.0188	.629	3
61.70	67.50	63.54	.7293+-.0114+-.0258	.079	2
70.20	81.60	75.36	.7260+-.0093+-.0302	.001	1
89.70	94.40	90.97	.7001+-.0161+-.0618	.000	0
108.90	113.40	111.10	.6806+-.0336+-.0603	.000	0
114.70	117.80	116.05	.7611+-.0415+-.0636	.000	0
123.30	134.50	128.46	.7081+-.0203+-.0529	.000	0
135.70	148.50	141.22	.7561+-.0278+-.0465	.050	1
151.70	159.20	157.41	.7173+-.0194+-.0343	1.075	1
160.90	169.80	165.12	.7497+-.0216+-.0369	1.056	1
174.60	183.40	179.83	.7831+-.0162+-.0388	.050	1
186.20	197.90	190.75	.8009+-.0160+-.0369	.270	1
205.60	219.90	212.48	.7757+-.0152+-.0530	.000	0
225.90	234.60	229.14	.8142+-.0201+-.0559	.000	0

Table 5-4b: Neutrino and Antineutrino cross sections

Antineutrinos

(errors below do not include a 5.9% common scale error)

E_{lo}	E_{hi}	E_{av}	$\frac{\sigma}{E}(10^{-38}cm^2/GeV)$*	χ^2	n_{df}
33.60	39.10	36.92	.3715+-.0099+-.0150	.671	2
41.80	49.80	45.04	.3617+-.0072+-.0131	.511	2
50.30	56.60	53.97	.3617+-.0073+-.0133	.733	3
61.00	69.20	63.80	.3367+-.0093+-.0146	2.189	2
71.60	80.40	75.55	.3375+-.0094+-.0205	.052	1
88.00	92.70	89.27	.3396+-.0153+-.0319	.000	0
106.70	114.50	110.30	.3000+-.0212+-.0324	.000	0
121.00	133.60	126.48	.3747+-.0192+-.0349	.000	0
138.70	158.70	149.97	.3792+-.0177+-.0249	.004	1
160.90	185.00	174.42	.3853+-.0173+-.0253	1.145	1
185.00	225.10	201.85	.3816+-.0216+-.0331	.595	1

* first error is statistical, the second is point to point systematic

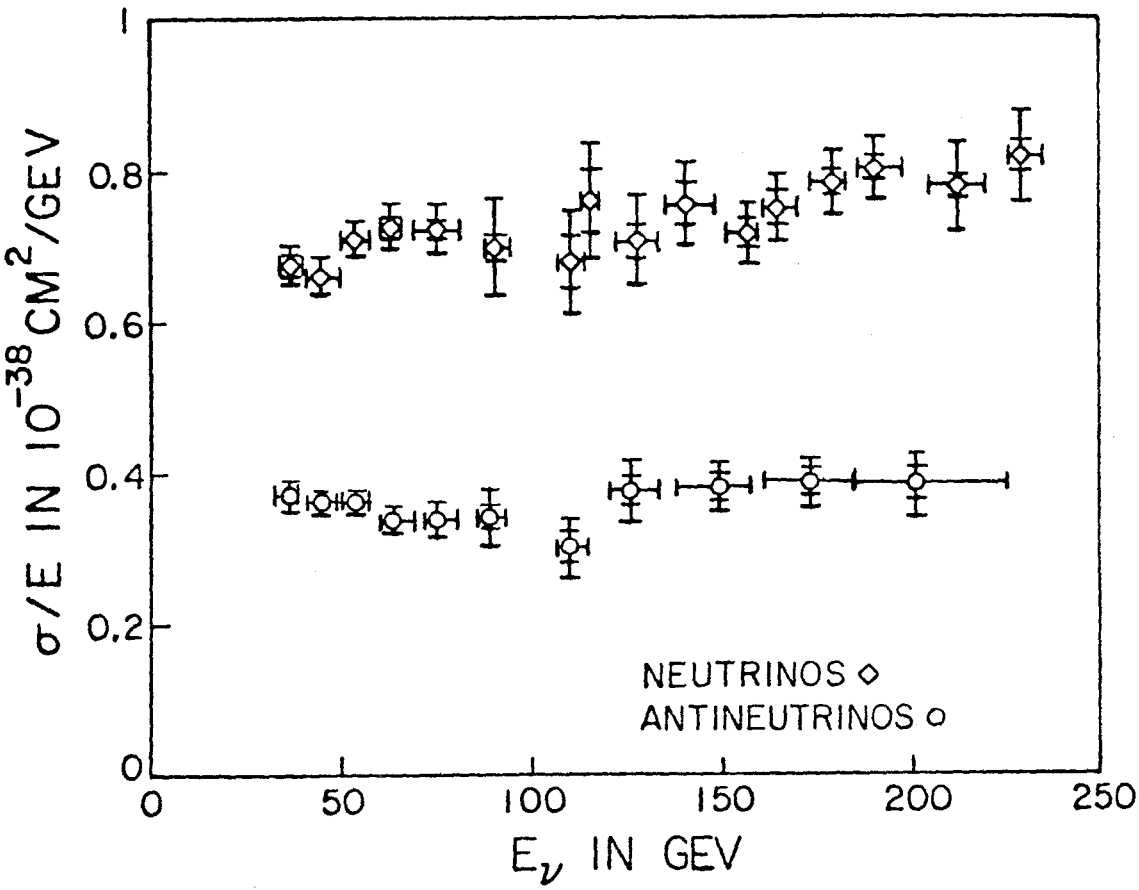

Figure 5-7: The slope of the neutrino and antineutrino cross section versus energy. The horizontal error bars indicate the range of average energies (5" radial binning) from which the slope is obtained. The inner error bars are statistical and outer are total point to point (there is an additional scale error of 3.6% for positives and 5.9% for negatives which is not plotted).

It should be emphasized that this measurement indicates a cross section level about 15% higher than most previous experiments. Table 5-5 lists the average slope (versus E_ν) of our neutrino and antineutrino cross sections along with the corresponding values obtained by other neutrino experiments. While this disagreement is alarming, we feel confident that adequate cross checks have been made to eliminate analysis errors as a source of this discrepancy.

The cross section slope ($\frac{\sigma}{E_\nu}$) is consistent with constant, although it is more consistent with a slight rise with energy. Assuming that the slope is independent of energy yields .721±.030 $\frac{x10^{-38}cm^2}{GeV}$ for neutrinos and .360±.023 $\frac{x10^{-38}cm^2}{GeV}$ for antineutrinos. The chi square of the data given this assumption is 39.2 for 30 degrees of freedom (87.9% confidence level) for neutrinos and 18.3 for 23 degrees of freedom (25.9% confidence level) for antineutrinos. These chi squared estimates include all independent cross section measurements (different secondary settings) as distinct and an accounting of the collective nature of beam errors for each setting. For example if the cross section slope for neutrinos from decays of 200GeV. kaons exhibits an energy dependence, this can have nothing to do with the ion chamber calibration nor with the 200GeV. kaon fraction in the beam. These do contribute to the error on the slopes, but not to the relative error between these points.

A number of redundancies were built into our experiment to insure that no single device was critical to our measurements. By comparing various measurements of the same or related quantities we were able to estimate the level of uncertainty in that quantity (see Appendix 1). Additional checks were performed to insure that cross sections were independent of the run number, and that geometric corrections (event weighting) were consistent with other methods of calculating these corrections (Monte Carlo method). A check was performed to exclude the possibility that different accelerator cycles might be used in the event and monitor analysis. The Cherenkov counter was run with both Helium and Nitrogen, thus measuring the proton peak in two vastly different pressure regimes as a check on the alignment corrections.

Table 5-5: average cross section slopes

Ref.	Energy (GeV)	$\frac{\sigma^{\nu}}{E}$ $(10^{-38}\frac{cm^2}{GeV})$	$\frac{\sigma^{\bar{\nu}}}{E}$ $(10^{-38}\frac{cm^2}{GeV})$
AS78	3-30	.72±.07	.32±.03
BA77	40-200	.61±.03	.29±.02
BO77	40-200	.63±.05	.29±.03
DE79b	30-200	.62±.05	.30±.02
JO80	20-200	.60±.03	.30±.02
LE81	25-260	.70±.03	
FR81	10-200	.66±.03	.30±.02
MO81	15-150	.62±.08	.29±.04
This Exp.	30-230	.72±.03	.36±.02

5.2. Method of construction of y distribution

There are two techniques available for the reconstruction of $y=\frac{E_h}{E_\nu}$ for a given neutrino event. The most straightforward and accurate method is to evaluate the hadronic energy and the energy of the muon produced and to consider their sum as an estimate of E_ν giving $y_1=\frac{E_h}{(E_h+E_\mu)}$. Unfortunately, this

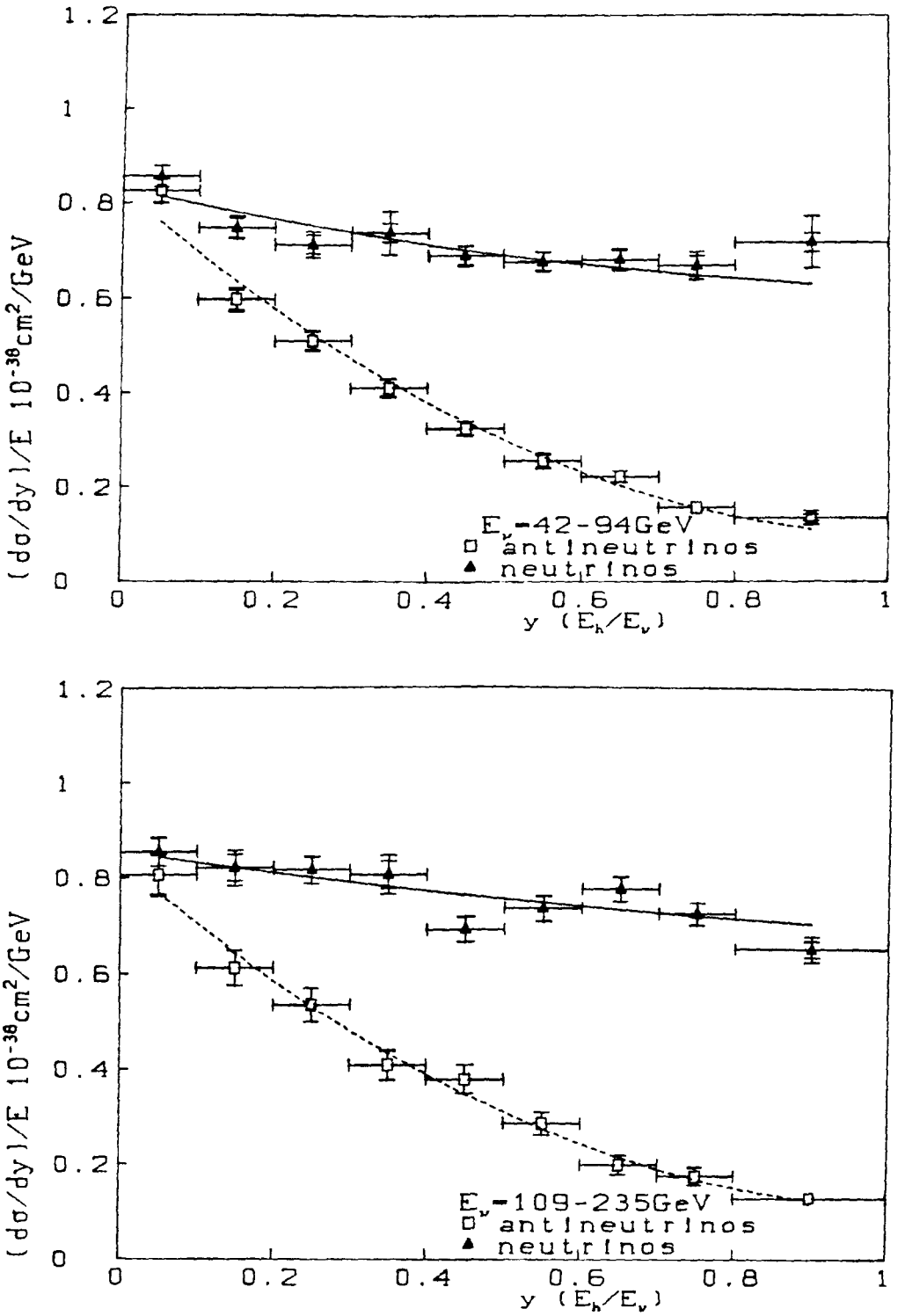

Figure 5-8: Neutrino and antineutrino y distributions. The error bars (vertical) include a systematic point to point error, but no contribution from flux errors which affect the over all level is included.

method requires that the muon passed through the toroid and consequently the muon angle must be smaller than about 100 mr., to insure that we do not need a sizable correction for acceptance. The other method is to use the properties of the dichromatic beam to predict for a given vertex location in the target what the average neutrino energy is, giving $y_2=\frac{E_h}{E_\nu(R)}$. This method sacrifices resolution but for large y it has the advantage that it uses all events which are used in the cross section analysis, since as described in section 5.2.1 we can count events from pion and kaon decay neutrinos for all values of E_h. These two methods clearly complement each other. For this reason it was decided to use the first method $y_1=\frac{E_h}{(E_h+E_\mu)}$ for low y and the second $y_2=\frac{E_h}{E_\nu(R)}$ for high y. For neutrinos from pion decay the transition point was taken at $y=.2$ and for neutrinos from kaon decay $y=.4$, using these values insured that the low y acceptance corrections were small (<3%). Above y of .8 the value of $\frac{d\sigma}{dy}$ is sensitive to the model used to correct the y distribution for acceptance and resolution as well as the secondary beam energy and the width of the neutrino energy distribution. Because of the sensitivity of this high y region, the value of $\frac{d\sigma}{dy}$ for y above.8 was never used in making fits to the data. All corrections were made using the x and y distributions reported in reference [DE79a]. Plots of $\frac{1}{E}\cdot\frac{d\sigma}{dy}$ averaged over all 5 energy settings for kaon and pion decay neutrinos after all acceptance, resolution and radiative corrections appear in figure 5-8. Fits were performed of the form $\beta(1-\alpha+\alpha(1-y)^2-\frac{Ry^2}{2(1+R)})$ for neutrinos, and $\beta(\alpha+(1-\alpha)(1-y)^2-\frac{Ry^2}{2(1+R)})$ for antineutrinos (with $R=.1$). Fits of this form appear in figure 5-8 and the results of fitting pion and kaon decay neutrinos for all settings are listed in table 5-6.

Table 5-6: Summary of Fits to Y Distributions

type	E_{av}	α	β	<y>	χ^2 (df=7)
ν	45.1	.29±.08	.872±.053	.482±.010	12.2
ν	51.1	.17±.08	.809±.046	.481±.015	1.9
ν	58.5	.19±.07	.820±.043	.494±.009	10.8
ν	66.3	.14±.07	.812±.039	.489±.008	6.3
ν	77.0	.18±.07	.816±.043	.489±.008	3.7
ν	113.0	.29±.11	.895±.081	.469±.013	4.8
ν	129.2	.10±.10	.779±.058	.485±.010	14.3
ν	150.9	.06±.08	.838±.048	.480±.007	10.2
ν	173.8	.16±.06	.854±.039	.479±.006	3.3
ν	205.6	.13±.05	.926±.035	.468±.006	16.7
$\bar{\nu}$	44.7	.13±.03	.881±.053	.318±.011	3.9
$\bar{\nu}$	50.6	.15±.03	.857±.044	.331±.011	5.9
$\bar{\nu}$	58.0	.15±.03	.863±.041	.335±.011	7.9
$\bar{\nu}$	65.4	.19±.03	.771±.038	.338±.008	5.5
$\bar{\nu}$	75.9	.17±.03	.747±.046	.337±.010	6.3
$\bar{\nu}$	110.3	.09±.05	.750±.075	.316±.017	11.8
$\bar{\nu}$	126.5	.18±.04	.859±.068	.331±.014	3.6
$\bar{\nu}$	147.6	.17±.04	.868±.063	.340±.103	4.7
$\bar{\nu}$	169.3	.19±.04	.773±.056	.345±.013	15.3
$\bar{\nu}$	199.1	.16±.04	.902±.071	.332±.014	3.5

0.0.1. Differential cross section at y=0

For an isoscaler target (one which has an equal number of neutrons and protons) as y approaches 0 the cross section should be the same for neutrinos and antineutrinos provided we stay well above the threshold of charmed and strange particle production. The reason for this is that the sea being invariant under CP will have the same probability for interaction with neutrinos and antineutrinos, the probability for scattering off of valence quarks at y=0 is proportional to $\frac{2G^2mE}{\pi} \cdot \langle x \rangle_{q_{valence}} \cdot (1+R)$ and given the above conditions this will be the same for neutrinos and antineutrinos . The y=0 value of the fits to the y distribution are plotted for each energy setting in figure 5-9. The average of $\frac{1}{E} \cdot \frac{d\sigma}{dy}|_{y=0}$ for neutrinos is $.842 \pm .016 \times 10^{-38} \frac{cm^2}{GeV}$ and for antineutrinos it is $.827 \pm .018 \times 10^{-38} \frac{cm^2}{GeV}$(the errors quoted here do not include the beam monitoring uncertainty of about 5%). The value of $\frac{1}{E} \cdot \frac{d\sigma}{dy}$ also gives us an estimate of $\int_0^1 F_2 dx$ for low Q^2. In fact $\int_0^1 F_2 dx \cdot \frac{G^2m}{\pi} = \frac{1}{E} \cdot \frac{d\sigma}{dy}|_{y=0}$ and since $Q^2 = 2mxyE + m^2$ limiting y to $y < .1$ insures that we use only low Q^2 events. Using only low y data yields $\int_0^1 F_2 dx$ as outlined in table 5-7 along with other measures of this quantity.

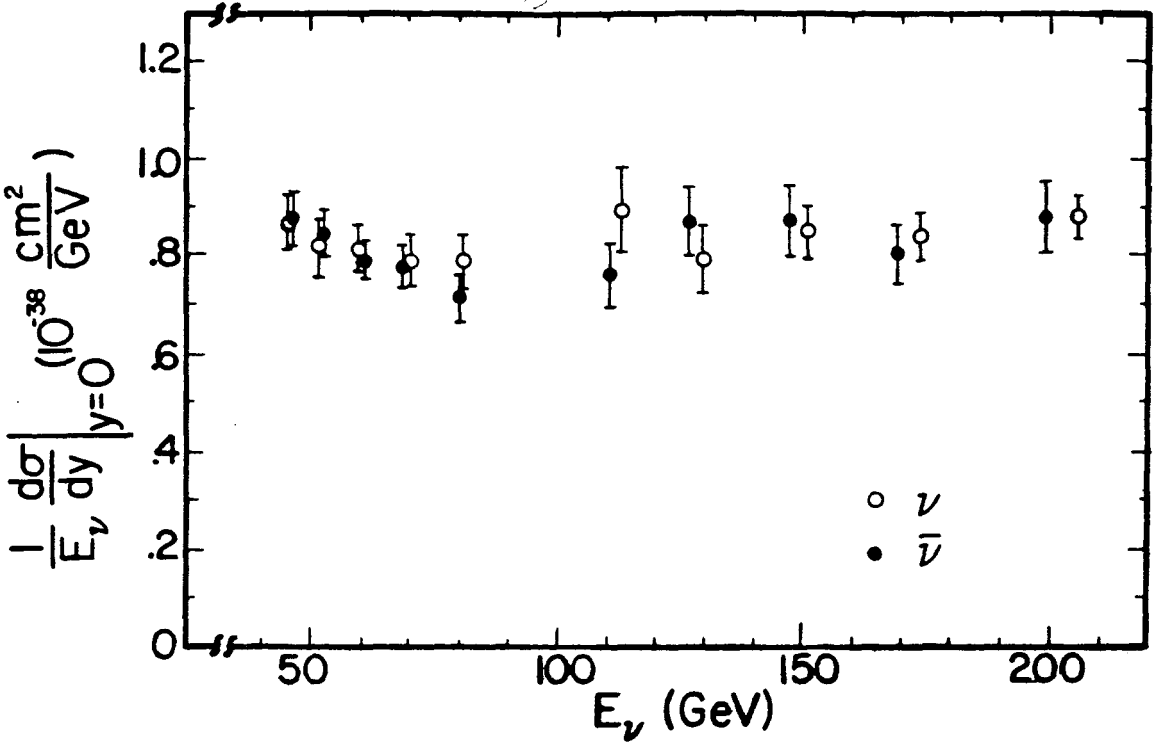

Figure 5-9: The y equal zero cross section from fits to the y distributions. The errors are statistical only.

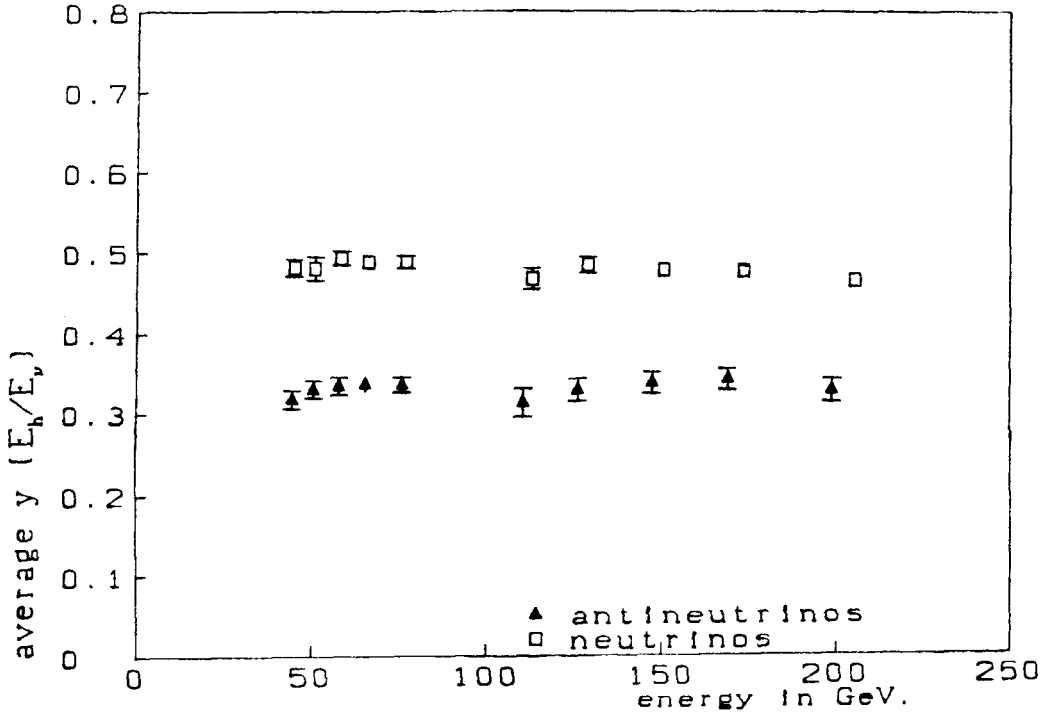

Figure 5-10: Average y of neutrino and antineutrino interactions.

Table 5-7: Low Q^2 measurements of $\int F_2 dx$

group	experiment	$\int F_2 dx$	method
CFRR	$\nu Fe \rightarrow \mu X$	.53±.02	fit to $\frac{d\sigma}{dy}$ $y<.8$
"	$\bar{\nu} Fe \rightarrow \mu X$	.52±.03	" " " "
"	average of $\nu+\bar{\nu}$	.53±.02	
CFRR	$\nu Fe \rightarrow \mu X$	.55±.02	low y ($y<.1$) value of $\frac{d\sigma}{dy}$
"	$\bar{\nu} Fe \rightarrow \mu X$	.56±.03	" " " "
"	average $\nu+\bar{\nu}$	.56±.02	
CDHS	average of $\nu+\bar{\nu}$	.45±.02	$\frac{d\sigma}{dy}$ *all* y
BEBC	average of $\nu+\bar{\nu}$	.51±.05	$\frac{d\sigma}{dy}$ $y<.2$
GGM	average of $\nu+\bar{\nu}$	.48±.04	$\frac{d\sigma}{dy}$ $y<.2$
SLAC	$eD \rightarrow eX$	.52	integrating fit to $F_2(x')$
CITFR	average of $\nu+\bar{\nu}$	.46±.02	$\frac{d\sigma}{dy}$ $y<.2$

5.2.2. Average y

The average value of y is a measure of the relative amount of quark and antiquark in the nucleon. Recall that in the NQPM we have (see next section):

$$\frac{1}{E}\cdot\frac{d\sigma^{\nu}}{dy}=\frac{2G^2m}{\pi}[<x>_q+<x>_{\bar{q}}(1-y)^2]$$

and

$$\frac{1}{E}\cdot\frac{d\sigma^{\bar{\nu}}}{dy}=\frac{2G^2m}{\pi}[<x>_q(1-y)^2+<x>_{\bar{q}}]$$

$$<y>^{\nu}=\frac{(<x>_q+\frac{<x>_{\bar{q}}}{6})}{(2<x>_q+\frac{2<x>_{\bar{q}}}{3})}$$

$$<y>^{\bar{\nu}}=\frac{(\frac{<x>_q}{6}+<x>_{\bar{q}})}{(\frac{2<x>_q}{3}+2<x>_{\bar{q}})}$$

in the limit at $<x>_{\bar{q}} \ll <x>_q$ we see that:

$$<y>^{\nu}\approx\frac{1}{2}$$

$$<y>^{\bar{\nu}}\approx\frac{1}{9}$$

or if $<x>_{\bar{q}} \gg <x>_q$

$$<y>^{\nu}\approx\frac{1}{9}$$

$$<y>^{\bar{\nu}}\approx\frac{1}{2}$$

This demonstrates that as the relative amount of quark (antiquark) in the nucleon increases the average value of y increases (decreases). The average

value of y versus energy is plotted in figure 5-11. There is no indication of any energy dependence in this quantity for neutrinos or antineutrinos. The average over all energies is .483± .003 for neutrinos (with a chi squared of 11.5 for 10 degrees of freedom) and .333 ± .004 for antineutrinos (with a chi squared of 6.3 for 10 degrees of freedom). If we use these measured values and solve for $\frac{<x>_{\bar{q}}}{<x>_q}$ we get:

for neutrinos

$$\left(\frac{<x>_{\bar{q}}}{<x>_q+<x>_{\bar{q}}}\right)=.18\pm.03$$

and for antineutrinos

$$\left(\frac{<x>_{\bar{q}}}{<x>_q+<x>_{\bar{q}}}\right)=.142\pm.009$$

Unfortunately, the neutrino value is sensitive to the assumption that R=0, if we evaluate $\frac{<x>_{\bar{q}}}{(<x>_q+<x>_{\bar{q}})}$ with R fixed at .1, we get .1, the antineutrino value is unchanged.

5.3.The Standard Theory and Beyond

5.3.1.The Quark Parton Model and Scaling

As a tool for interpreting the cross section and y distribution results, we may use the naive quark parton model (NQPM). We can add QCD simply by allowing for a q^2 dependence in our quark x distributions [AL77]. The predictions of the NQPM allows us to relate various aspects of the distributions and the cross section. This should provide some insights into how well the data agree with any model which approximates the NQPM. In terms of the structure functions F_1, F_2, F_3 we have

$$\frac{d\sigma}{dxdy} = \frac{G^2 mE}{\pi}[(1 - y - \frac{m}{2E}xy)F_2^{\nu(\bar{\nu})}(x, Q^2)$$

$$+ \frac{y^2}{2} \cdot \frac{(1+4m^2\frac{x^2}{Q^2})}{(1+R(x))} F_2 \pm (y - \frac{y^2}{2})xF_3^{\nu(\bar{\nu})}]$$

$$R(x) = \frac{\sigma_L}{\sigma_T} = (1 + \frac{4m^2x^2}{Q^2}) \cdot \frac{F_2}{2xF_1} - 1$$

The NQPM yields

$2xF_1 = 2x(\Sigma_q f_q(x) + \Sigma_{\bar{q}} f_{\bar{q}})$

$xF_3 = 2x(\Sigma f_q - \Sigma f_{\bar{q}})$

where f_q = the x distribution of quark q in the nucleon

(only interacting quarks are counted, e.g. $d, s, \bar{u}, \bar{c}$ for ν's)

For high energies, where we can drop terms $O(\frac{mxy}{E})$, we can write:

$$\frac{d\sigma^{\nu}}{dxdy} = \frac{G^2 mE}{\pi}[Q + \bar{Q}(1-y)^2 + R\,(Q+\bar{Q}) \cdot (1-y)\,]$$

$$\frac{d\sigma^{\bar{\nu}}}{dxdy} = \frac{G^2 mE}{\pi}[\bar{Q} + Q(1-y)^2 + R\,(Q+\bar{Q}) \cdot (1-y)\,]$$

where $Q \equiv 2x\Sigma_q f_q$

$\bar{Q} = 2x\Sigma f_{\bar{q}}$

Intergrating over x we get:

$$\frac{d\sigma^{\nu}}{dy} = \frac{2G^2 mE}{\pi}[<x>_q + <x>_{\bar{q}}(1-y)^2 + <xR>\cdot(1-y)]$$

$$\frac{d\sigma^{\bar{\nu}}}{dy} = \frac{2G^2 mE}{\pi}[<x>_{\bar{q}} + <x>_q(1-y)^2 + <xR>\cdot(1-y)]$$

Integrating over y we have:

$$\sigma^{\nu} = \frac{2G^2}{\pi} mE[<x>_q + \frac{<x>_{\bar{q}}}{3} + <xR>\frac{1}{2}]$$

$$\sigma^{\bar{\nu}} = \frac{2G^2 mE}{\pi}[<x>_{\bar{q}} + \frac{<x>_q}{3} + <\frac{xR\ 1}{>\ 2}]$$

One complication that makes the apparent simplicity of these expressions deceptive is that for different regions of E, x and y , the final state mass will differ. For a given neutrino energy we may be mostly below the threshold for production of hadrons possessing strange, charmed or bottom quarks while at a much higher energy these final states will all be allowed and have about the same phase space. The counting of quarks is, therefore, complicated by thresholds. The correct treatment of such thresholds is beyond the ken of the NQPM since it must depend on how the struck quarks evolve into hadrons. The simplest, and undoubtedly wrong, method of treating such thresholds is to simply "turn on" each new flavor as soon as there is enough energy to produce it. This method is potentially useful because it provides an upper limit on the contribution of massive quark channels since we ignore suppression due to limited phase space just above the threshold.

The contribution of the charm threshold can be deduced from dimuon production to be from 0 to 10% of the total cross section over the energy range 25 to 250 GeV. While the expected contribution from bottom production is very small, some caution is advised since attempts to calculate the production of like sign dimuons (partially from bottom production) fall short by two orders of magnitude [FI81,BA81,PH79,JO81].

The NQPM prediction for the y distribution is particularly simple when it comes to the sum and difference of neutrino and antineutrino cross sections. In these cases the y distribution depends on one parameter provided the contribution from R is small. The one parameter is the scale. This may be set by the total $\frac{\sigma^{\nu}+\sigma^{\bar{\nu}}}{E}$. The comparison between the NQPM form and the observed distribution appear in figure 5-11; the agreement is excellent.

The difference between neutrino and antineutrino y distribution is insensitive to thresholds and the value of $\frac{\sigma_L}{\sigma_T}$. Figure 5-12 demonstrates that for each new threshold that opens up for neutrinos, there will be a corresponding threshold that opens up for antineutrinos with an identical probability and y distribution (this assumes that valence quarks are not involved). The NQPM and scaling predict that this quantity will remain independent of energy above charm threshold.

There are several sources of deviation from this simple NQPM y dependence. QCD predicts that the moments of the non singlet structure functions

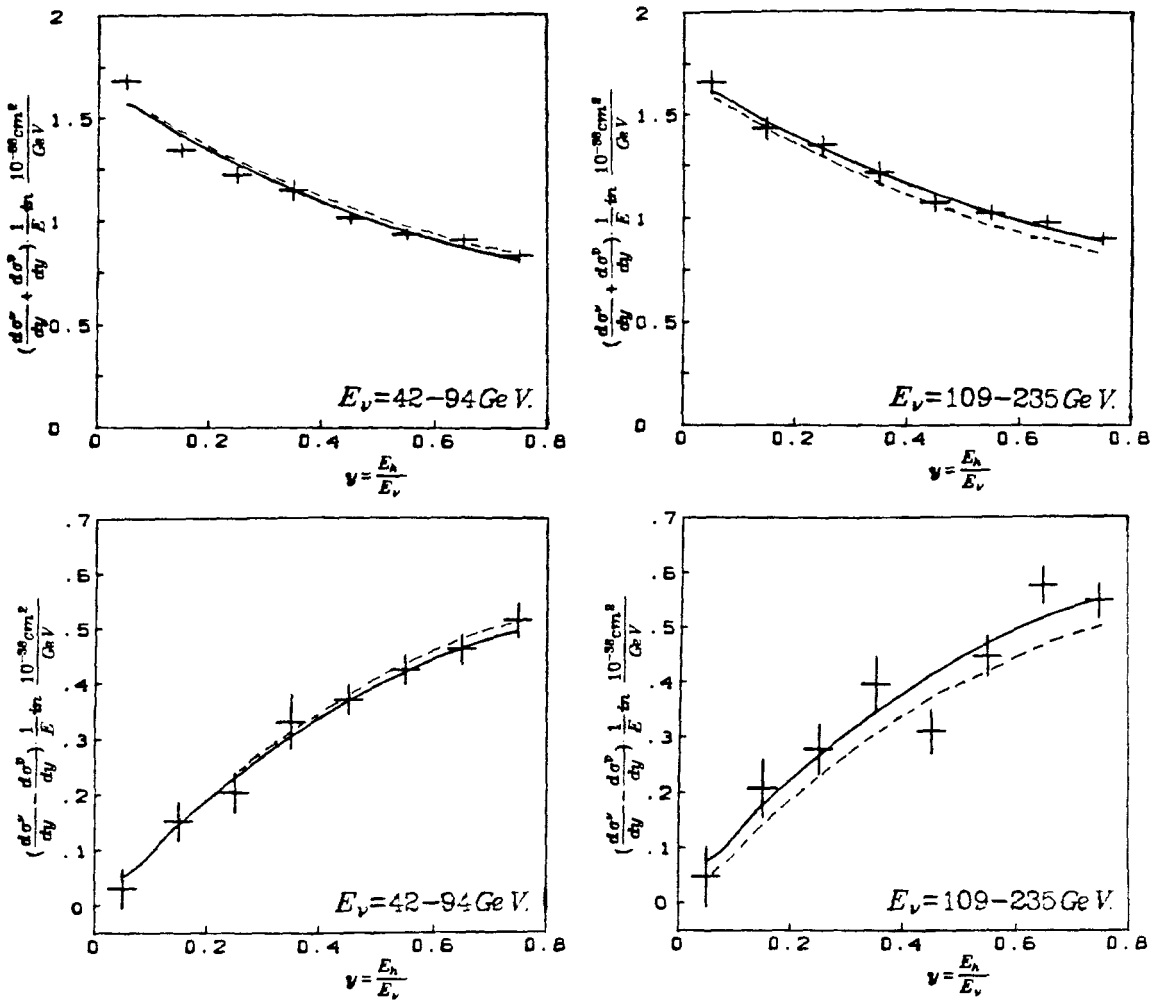

Figure 5-11: The sum and difference of neutrino and antineutrino y distributions. The solid lines are fits of the form expected in the NQPM with R=.1 . The dashed lines are what would be expected if the cross section slope was independent of energy.

massive quark production off of sea quarks by neutrinos

corresponding massive quark production by antineutrinos

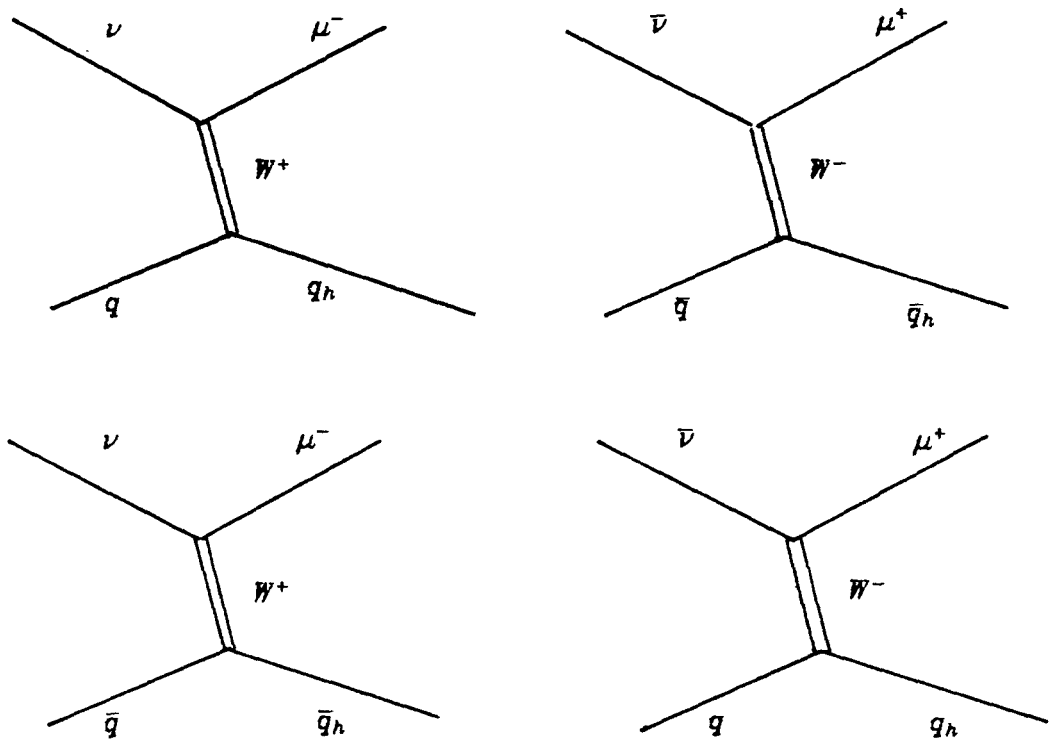

Figure 5-12: Type 1 (left hand side) and type 2 (right hand side) processes with equal probabilities for heavy quark production off of sea quarks.

(at fixed Q^2) should vary as $M_0\left[\frac{\alpha_s(Q_0^2)}{\alpha_s(Q^2)}\right]^{d_n}$ where the d_n are predicted by the theory and $\alpha_s \approx \alpha_s(Q_0^2)\frac{\ln(\frac{Q_0^2}{\Lambda^2})}{\ln(\frac{Q^2}{\Lambda^2})}$. It is a little difficult to predict how this translates into variation of the cross section versus neutrino energy since the prediction is valid only for large Q^2 and at fixed neutrino energy the cross section includes contributions from low Q^2. In order to account for this low Q^2 region, we can use the data to determine what fraction of events fall above some Q^2 value Q_0^2 above which we can trust the QCD prediction. A plot of the fraction of events above a Q^2 of 5 $\frac{GeV^2}{c^2}$ appears in figure 5-13 (corrections have been applied for smearing in order to account for event cross over). Armed with this factor, the ratio of events above and below $Q^2=5\frac{GeV^2}{c^2}$, we can predict the energy dependence of $\int xF_3 dx$. Using the x distribution and QCD fit of reference DE79a the expected energy dependence of $\int_0^1 xF_3 dx$ is plotted along with our data in figure 5-14.

5.3.2. Limits on the W Boson Mass

Another effect that will cause an energy dependence in the cross section for both ν and $\bar{\nu}$ is the decrease in cross section caused by a propagator effect. If we denote the cross section with a point like interaction ($M_W=\infty$)

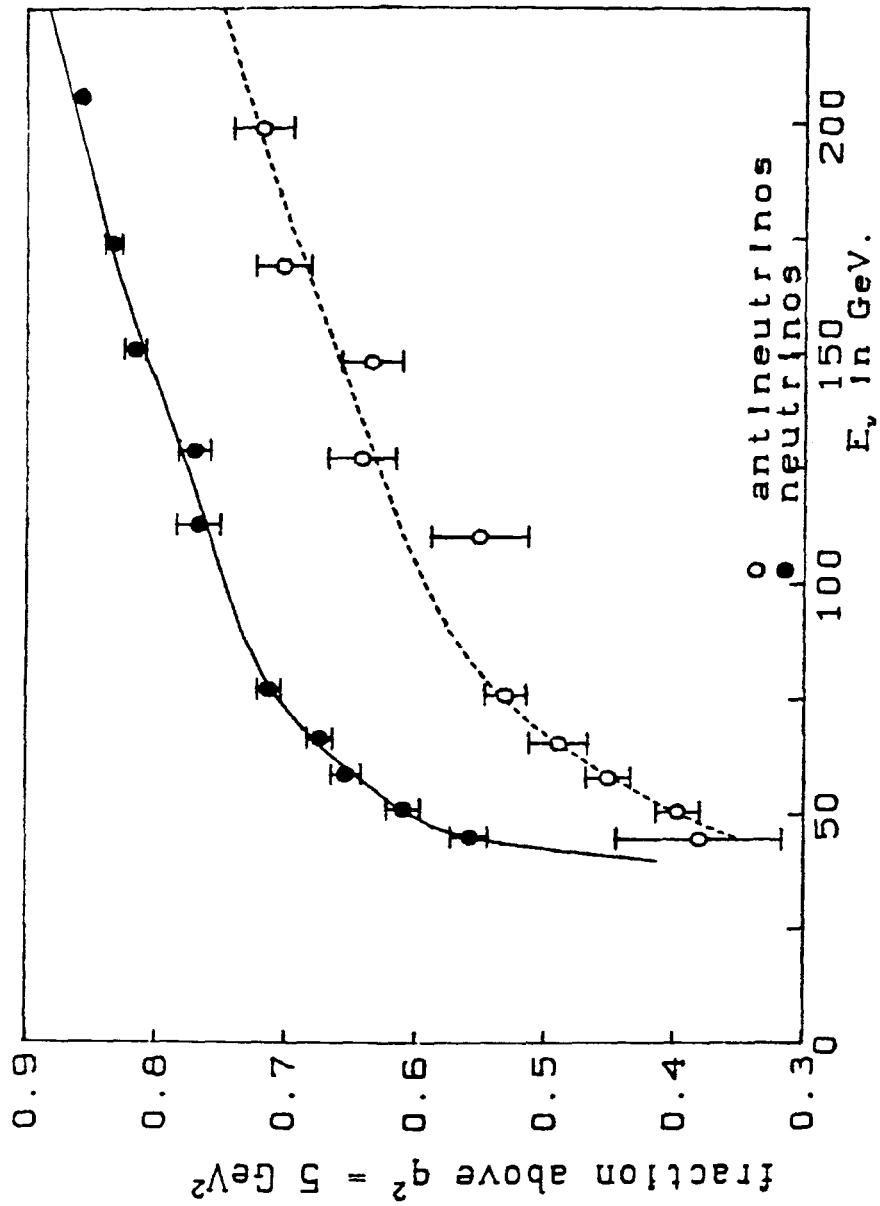

Figure 5-13: Fraction of events above Q^2=5GeV^2 used to make fixed lepton energy predictions from models whose low Q^2 predictions are not to be trusted (like QCD).

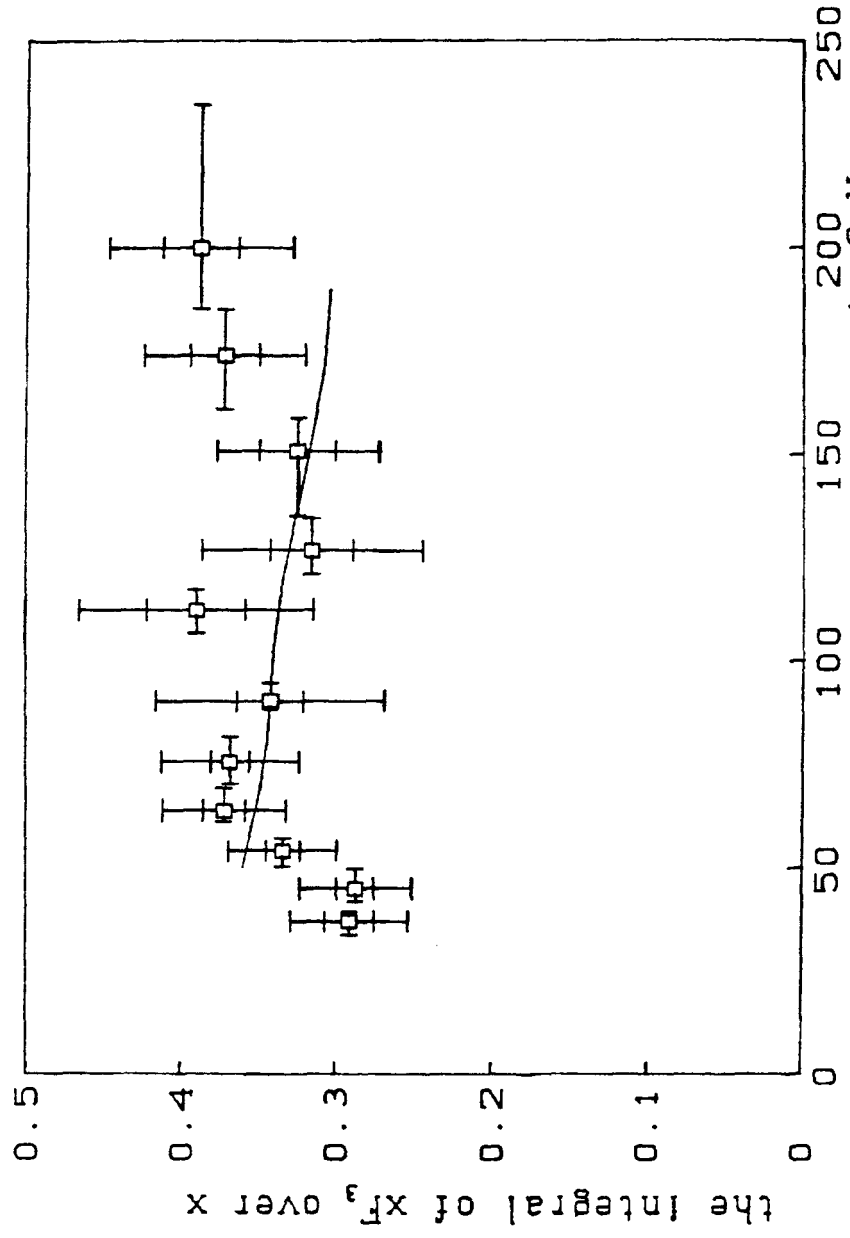

Figure 5-14: The behavior of $\int xF_3 dx$ expected from QCD (Λ_{LO}=.47GeV) using the parameters of reference GR79 (solid line) and from the total cross section measurements.

as σ_0 then:

$$\sigma^{\nu,\bar{\nu}}=\sigma_0{}^{\nu,\bar{\nu}}<\frac{1}{(1+\frac{Q^2}{M_W{}^2})^2}>$$

for $\frac{Q^2}{M_W{}^2}\ll 1$

$$\sigma^{\nu,\bar{\nu}}\approx\sigma_0{}^{\nu,\bar{\nu}}<(1-\frac{Q^2}{M_W{}^2})^2>$$

$$\sigma^{\nu,\bar{\nu}}\approx\sigma_0{}^{\nu,\bar{\nu}}<(1-\frac{2Q^2}{M_W{}^2})>=\sigma_0{}^{\nu,\bar{\nu}}(1-\frac{2}{M_W{}^2}<Q^2>)$$

$$\sigma^{\nu,\bar{\nu}}=\sigma_0{}^{\nu,\bar{\nu}}(1-\frac{2mE_\nu}{M_W{}^2}[\frac{<Q^2>}{mE_\nu}])$$

$$\sigma^{\nu}-\sigma^{\bar{\nu}}=(\sigma_0{}^{\nu}-\sigma_0{}^{\bar{\nu}})-\frac{2mE_\nu}{M_W{}^2}(\sigma_0{}^{\nu}\frac{<Q^2>_\nu}{mE_\nu}-\sigma_0{}^{\bar{\nu}}\frac{<Q^2>_{\bar{\nu}}}{mE_\nu})$$

$$\sigma^{\nu}-\sigma^{\bar{\nu}}=(\sigma_0{}^{\nu}-\sigma_0{}^{\bar{\nu}})-\alpha E_\nu(\sigma_0{}^{\nu}-\sigma_0{}^{\bar{\nu}})$$

$$\sigma^{\nu}-\sigma^{\bar{\nu}}=(\sigma_0{}^{\nu}-\sigma_0{}^{\bar{\nu}})(1-\alpha E_\nu)$$

A limit on the value of α translates to a limit on the W mass via the quantity $\frac{<Q^2>}{mE_\nu}$ which will differ for neutrinos and antineutrinos(we use .112 for neutrinos and .063 for antineutrinos). This gives a limit on the W mass of: $18GeV<M_W$ at the 90% confidence level. This limit is not particularly stringent however it is free from bias due to any rise in the cross section induced by thresholds.

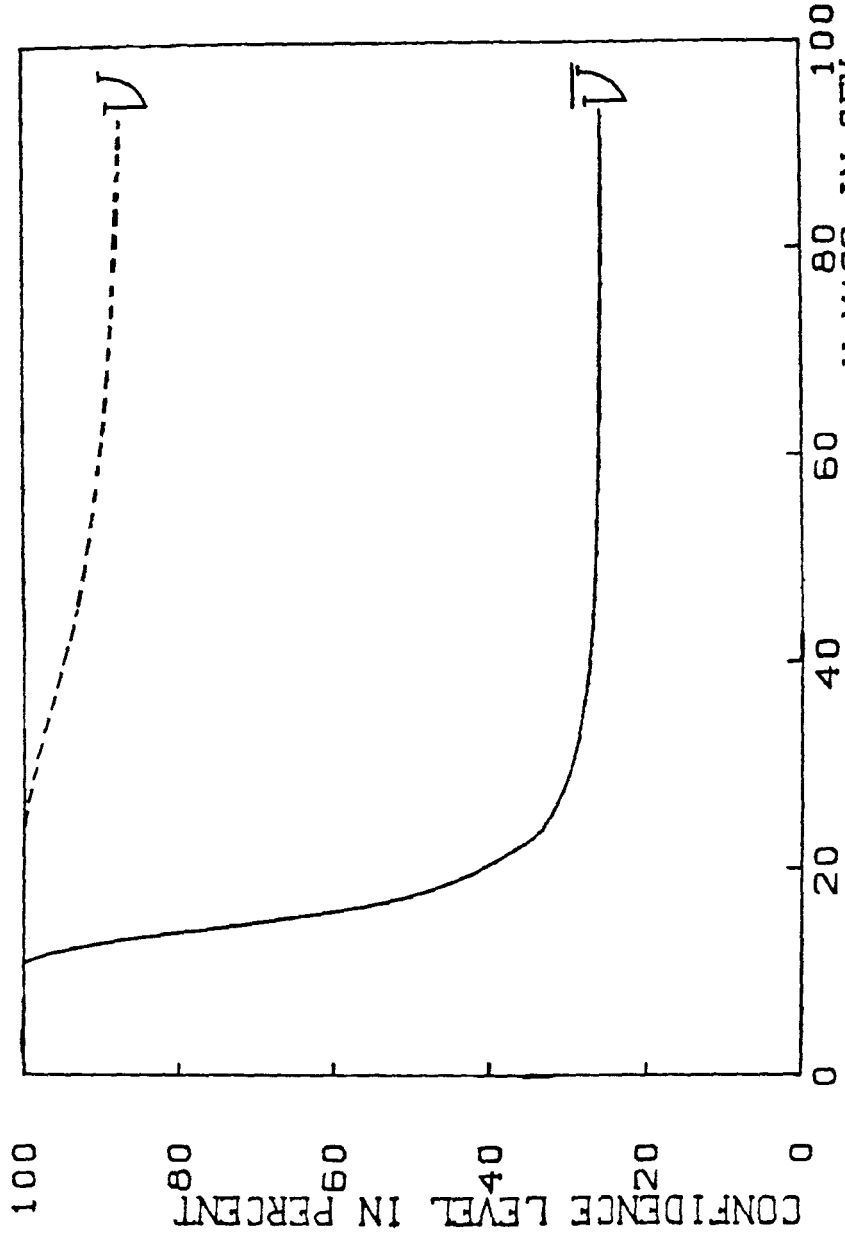

Figure 5-15: Confidence level versus W mass. Given the assumption that deviations of the cross section slope from energy independence are all induced by a W propogator effect, the confidence level versus W mass is plotted. Confidence level is defined as the probability that a subsequent experiment would obtain a smaller χ^2.

It is possible to extract a higher W mass limit from the neutrino cross section alone, since the neutrino cross section alone has smaller relative errors than $\frac{\sigma^{\nu}-\sigma^{\bar{\nu}}}{E}$. We should estimate and correct for any effects that arise from new particle production, since as the charm and bottom thresholds open up the cross section will rise. In the standard theory these effects are very small and typically the decrease in cross section due to QCD is expected to outstrip any new threshold and should not influence our conclusions. The data, however, seems more consistent with a rise in cross section slope as the energy increases. This rise is not expected in the standard model and leaves the data only marginally consistent with energy independent slope.

The interpretation of this rise being uncertain leaves the W mass limit obtained in this way equally uncertain. Given this warning the limit obtained from simply seeing how much of a propagator effect can be tolerated "assuming" that the cross section slope is independent of energy is plotted in figure 5-16.

5.3.3. Comparison with Electron and Muon Scattering

The sum of the neutrino and antineutrino cross sections yields the average x of the valence plus sea distributions in the nucleon. From before we have:

$$\int_0^1 \frac{F_2}{(1+R)}dx = 2(\langle x\rangle_q + \langle x\rangle_{\bar{q}}) = \frac{3(\sigma^{\nu}+\sigma^{\bar{\nu}})}{G^2 mE(4+3R)}$$

Keep in mind that we only sample the $d, \bar{u}, s, \bar{c}$ and b quarks with neutrinos and $\bar{d}, u, \bar{s}, c$ and $\bar{b}$ quarks with antineutrinos. To be complete we should have written the above as:

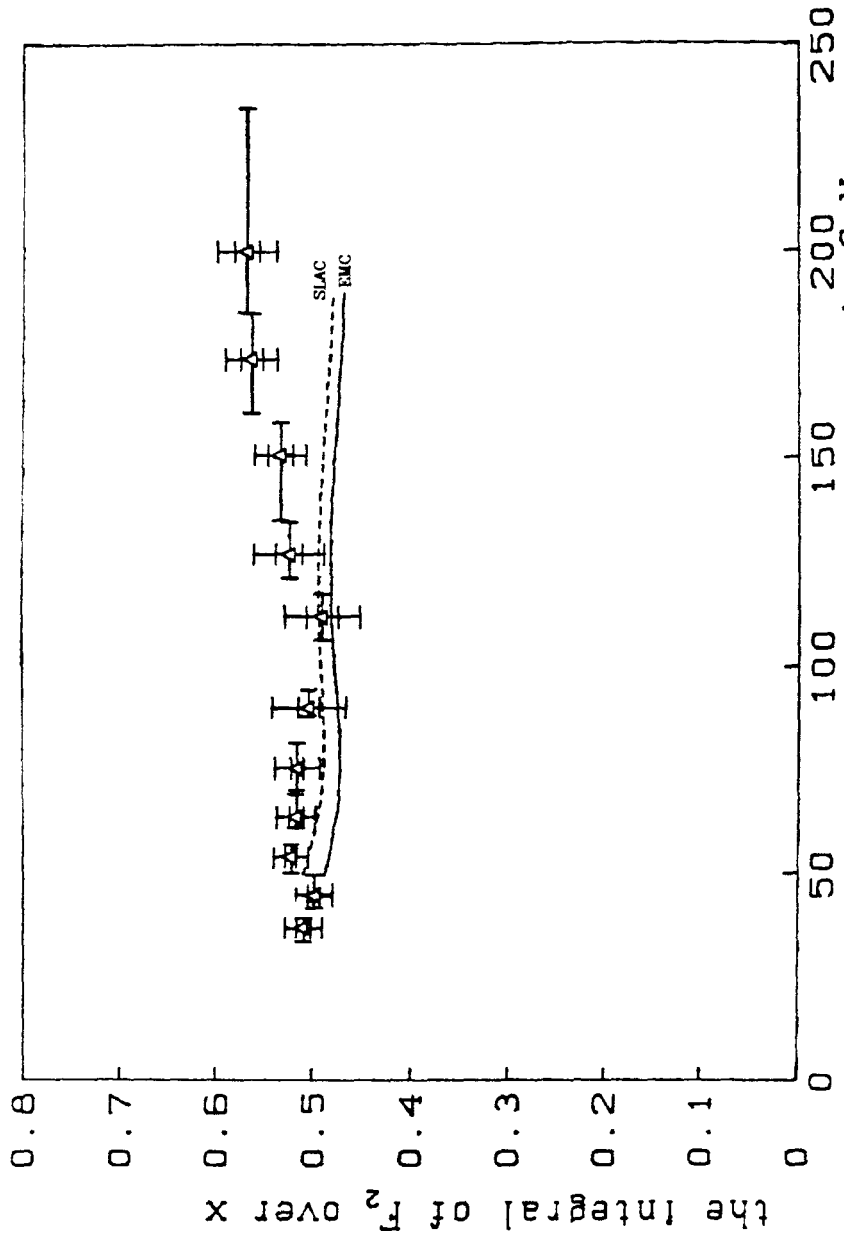

Figure 5-16: Comparison of electron and muon results with the total cross section sum. The curves indicate the value of the integral of F_2 over x obtained by integrating $F_2(x,Q^2)$ over x for the same Q^2 as neutrino interactions using models of F_2 derived from fits to ed(SLAC - [AB80]) and μFe(EMC - [AU81]) scattering . The data come from the sum of the neutrino and antineutrino cross sections.

$$\int_0^1 \frac{(F_2^{\nu}+F_2^{\bar{\nu}})}{2(1+R)}dx = 2\left(\frac{(\langle x\rangle_q^{\nu}+\langle x\rangle_q^{\bar{\nu}})}{2} + \frac{(\langle x\rangle_{\bar{q}}^{\nu}+\langle x\rangle_{\bar{q}}^{\bar{\nu}})}{2} \right)$$

$$\int_0^1 \frac{(F_2^{\nu}+F_2^{\bar{\nu}})}{2(1+R)}dx = \frac{3(\sigma^{\nu}+\sigma^{\bar{\nu}})}{G^2 mE(4+3R)}$$

Actually a small correction (~2%) should be applied to the above to compensate for the fact that $xF^{\nu}{}_3 \neq xF^{\bar{\nu}}{}_3$

From this we can see that, since all flavors are sampled by either neutrinos or antineutrinos, the average x for all quark and antiquark constituents is:

$$\langle x\rangle_{all} = \int_0^1 \frac{F_2^{\nu}+F_2^{\bar{\nu}}}{2(1+R)}dx = \frac{3(\sigma^{\nu}+\sigma^{\bar{\nu}})}{G^2 mE(4+3R)}$$

The same quantity is measured in electron and muon scattering (modulo a factor of the average squared quark charge, $\frac{5}{18}$). Several experiments have published parameterizations of F_2 which allow us to estimate the integral. To compare our results with theirs, the integral was performed over the same Q^2 region as the neutrino events for $Q^2 > 5 GeV^2$. A correction for the missing low Q^2 region was made using the ratio $\frac{\sigma^{\bar{\nu}}}{\sigma^{\nu}}$ as .499 (independent of energy) and the above ratio of high to low Q^2 events. The value of R quoted by each group was used to calculate a quantity proportional to $\sigma^{\nu}+\sigma^{\bar{\nu}}$, then the value of $\int_0^1 F_2 dx$ was obtained by using the above formula with $R = .1$. These results suggest that at high energy ($E_{\nu} > 150 GeV$) there is a difference between what is expected from electro and muo production data and what we obtain.

One possible difference is the contribution from the heavy quark sea (c,b,t...). For example, if the b quark were to couple via a Cabbibo type mixing with lighter quarks, then, since muo production does not change quark flavors, there would be no effect (i.e. the b quark sea may be very small). Neutrino

experiments, however, would see an anomalously large b production rate. If we use constraints put on the mixing by e^+e^- data [HI81] the effect on $\int_0^1 F_2 dx$ is quite small (see figure 5-16). Perhaps these guesses are incorrect, or it could be that the above method of comparison is too crude. It would be much better to compare the values of F_2 versus x and Q^2 directly for both types of experiments. A careful study of the dimuon production by neutrinos and muon scattering experiments might clarify this apparent discrepancy. It may also be that e^+e^- experiments studying heavy quark weak decays will contribute to our understanding of this difference.

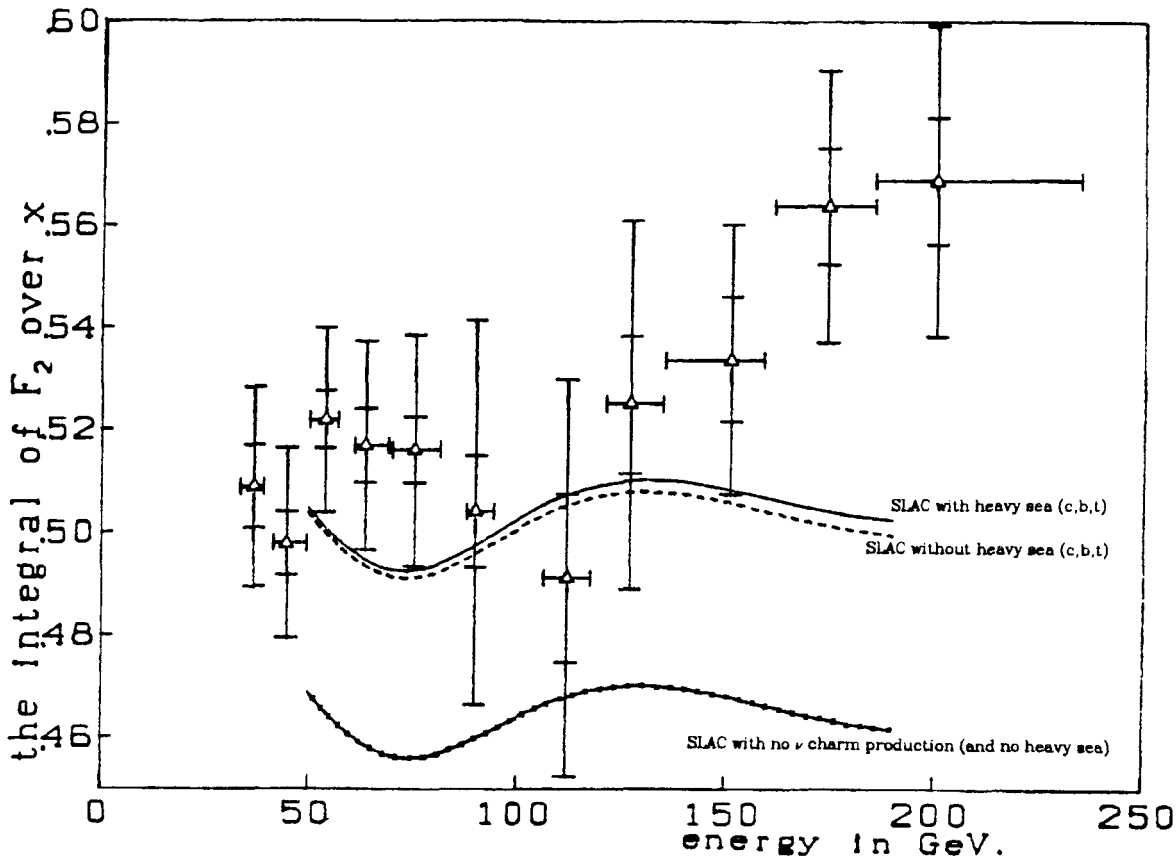

Figure 5-17: The affect of heavy quarks on $\int_0^1 F_2 dx$.

In order to illustrate the effect of heavy (c,b,t and beyond) quarks we show the effect of a generous c,t and b sea (two thirds of the s sea which is taken as suppressed by a third from the u and d sea) and "fast rescaling" or no suppression near threshold. Despite the small contribution from the heavy sea, charm production (off of s's and d's) does make an observable difference in $\int F_2 dx$ given these assumptions. The F_2 model used for this calculation is the x' scaling function reported in B079.

5.3.4. Neutrino Oscillations

An unsettled question in neutrino physics is whether the neutrino is massive. The assumption that neutrinos are massless has long been a theoretical prejudice, but the popularity of this idea is not due to any fundamental expectation. The early experiments designed to determine the mass of the electron type neutrino led to very small mass limits. These results plus the observation

that the three lepton families manifest similarities (which, however, do not include equal charged lepton masses), have led to the simplifying assumption that a "massless" electron neutrino can be generalized to massless neutrinos for all leptons. Recently, the arbitrariness of this prejudice has been driven home by two experiments which tend to favor a massive neutrino [RE80, LU80]. While these experiments have no direct bearing on our results (they have relevance to the ν_e), it is interesting to see what information about the ν_μ mass can be gleaned from our cross section results.

Let us assume that the neutrino produced in π decay is in state $|\nu,\vec{p}>$, $\vec{p}$ is the momentum , which is a superposition of n different massive neutrinos.

$$|\nu_\mu,\vec{p}=\sum_{j=1}^{n} U_{\mu j}\,|\nu_j,\vec{p}>$$

where $|\nu_j\vec{p}>$ is the eigenstate of mass with mass m_j

$U_{\mu j}$ is the μ,j^{th} element of a unitary matrix

(μ indexes the muon neutrino and any neutrinos it might mix with and j indexes the mass states).

For each massive state we will have $E_j \approx |\vec{p}| + \frac{m_j{}^2}{2|\vec{p}|}$. As time passes after the emission of the neutrino the various mass states begin to interfere with one another:

$$|\nu,\vec{p}>(t)=\sum_{j=1}^{n} U_{\mu j}\, e^{-k_\sigma x^\sigma}\,|\nu_j,\vec{p}>$$

$$|\nu,\vec{p}>(t)=e^{i(\frac{\vec{p}}{\hbar}\cdot\vec{r}-\frac{|\vec{p}|}{\hbar}\cdot t)}\sum U_{\mu j}\, e^{\frac{-itm_j{}^2}{\hbar 2|\vec{p}|}}\nu_j,\vec{p}>$$

$$|\nu,\vec{p}>(t)\approx e^{i(\frac{\vec{p}}{\hbar}\cdot\vec{r}-\frac{|\vec{p}|}{\hbar}\cdot t)}\sum U_{\mu j}\, e^{\frac{-itm_j{}^2}{\hbar c 2|\vec{p}|}}\nu_j,\vec{p}>$$

The amplitude for finding the neutrino in its original state is:

$$<\nu_\mu,\vec{p}\,|\,\nu,\vec{p}>(t)=e^{i(\frac{\vec{p}}{\hbar}\cdot\vec{r}-\frac{|\vec{p}|}{\hbar}\cdot t)}\sum_k U^*_{\mu k}\,U_{\mu k}\,e^{\frac{-iLm_k{}^2}{\hbar c\,2|\vec{p}|}}$$

The unitarity requirement in $U_{\mu j}$ gives us the constraint that $\sum_k U^*_{\mu k}\,U_{\mu k}=1$. The probability of finding a ν_μ at a distance L from the emission is then:

$$\mathbf{P}_{\nu_\mu}(L)=|\sum_k U^*_{\mu\nu}U_{\mu\nu}e^{\frac{-iLm_\mu{}^2}{2\hbar c\,|\vec{p}|}}|^2$$

Letting n = 3

$$\mathbf{P}_{\nu_\mu}(L)=\left|a_1 e^{\frac{-iLm_1{}^2}{2\hbar c\,|\vec{p}|}}+a_2 e^{\frac{-iLm_2{}^2}{2\hbar c\,|\vec{p}|}}+a_3 e^{\frac{-iLm_3{}^2}{2\hbar c\,|\vec{p}|}}\right|^2$$

$$\mathbf{P}_{\nu_\mu}(L)=a_1{}^2+a_2{}^2+a_3{}^2+2a_1a_2\cos(\frac{L(m_2{}^2-m_1{}^2)}{2\hbar c\,|\vec{p}|})$$

$$+2a_2a_3\cos(\frac{L(m_3{}^2-m_2{}^2)}{2\hbar c\,|\vec{p}|})+2a_1a_3\cos(\frac{L(m_3{}^2-m_1{}^2)}{2\hbar c\,|\vec{p}|})$$

where: $a_k\equiv U^*_{\mu k}\,U_{\mu k}$ which is real

$$\mathbf{P}_{\nu_\mu}(L)=1-4(a_1a_2\sin^2(\frac{L(m_2{}^2-m_1{}^2)}{4\hbar c\,|\vec{p}|})+a_2a_3\sin^2(\frac{L(m_3{}^2-m_2{}^2)}{4\hbar c\,|\vec{p}|})$$

$$a_1a_3\sin^2(\frac{L(m_3{}^2-m_1{}^2)}{4\hbar c\,|\vec{p}|}))$$

$$\frac{1}{4\hbar c} = 1.27\frac{GeV}{eV^2 \cdot km}$$

since: $a_1+a_2+a_3=1$ we may write this as:

$$P_{\nu_\mu}(L)=1-(\sin^4\Theta\sin^2\varphi\sin^2(\frac{L(m_2^2-m_1^2)}{4\hbar c\,|\vec{p}\,|}) + \sin^2 2\Theta(\sin^2\varphi\sin^2(\frac{L(m_3^2-m_2^2)}{4\hbar c\,|\vec{p}\,|})+\cos^2\varphi\sin^2(\frac{L(m_3^2-m_1^2)}{4\hbar c\,|\vec{p}\,|})))$$

In reality, we have to average these results over an energy spectrum and over the decay region. The effect of this averaging is demonstrated in figure 5-18.

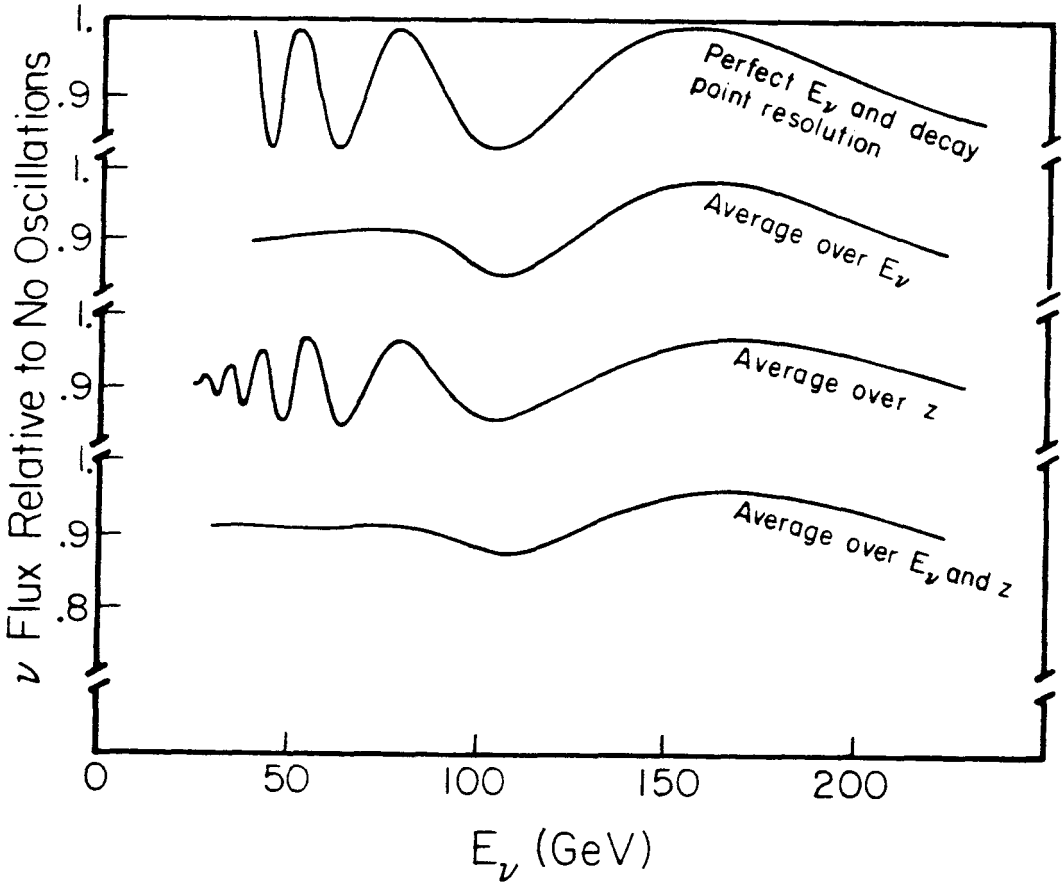

Figure 5-18: The effect of E and z averaging on neutrino oscillations. For the purpose of illustrating the effect of a finite decay path, and averaging over neutrinos of varying energies we have fixed $\Delta m^2=365ev^2$ and $\sin^2 2\theta = .17$ average over the energy spectrum and decay length typical to our experiment is depicted separately and together.

Since the high energy cross sections seem to exceed what would be expected from deep inelastic scattering of muons and electrons (see last section), the conventional view would suggest that the shape of the cross section versus energy (in particular the rise at high energy) could not result from neutrino oscillations. Oscillations can only deplete the number of muon neutrinos. A comparison of F_2 versus x and Q^2 should clarify this issue. The difference between results may arise in part from crudeness of the above comparison. In particular we have used a model which came from measurements over a limited range of x and Q^2 and extended it to include all x and Q^2 for events from neutrino interactions of a given neutrino energy. A direct comparison between datum at overlapping x and Q^2 is proceeding on the extraction of $F_2(x,Q^2)$ from our data, but in the meantime, given that we recognize the shortcomings of this approach, an attempt to see whether the energy dependence of the cross section slope can be fit by or can put limits on neutrino oscillations is in order.

The starting point will be the assumption that the neutrino and antineutrino cross section slopes $(\frac{\sigma^{\nu(\overline{\nu})}}{E})$ should be independent of energy, except from the effect of oscillations. Given this assumption a fit was performed to our data for oscillations between two (φ=0) neutrino types. The results are plotted in figure 5-19. The results include a best fit value and allowed regions of mass difference and mixing angles ($\sin^2(2\Theta)$ and $\Delta m^2=(m_3{}^2-m_2{}^2)$).

It should be emphasized that normalized neutrino cross section yield information about "inclusive" oscillations. Very precise limits exist for the rate at which muon neutrinos produce tau neutrinos and muon neutrinos produce electron neutrinos. Despite these limits it is still possible to envision the muon neutrino oscillating to types of neutrinos which do not participate in weak interactions (e.g. the muon neutrino might oscillate to a left handed muon antineutrino

which interacts very weakly; this process would violate lepton conservation by two units). Our data may be suggestive of neutrino oscillations, but are by no means conclusive. An experiment is being mounted at Fermilab to investigate this possibility further, by constructing a second detector midway between the present lab E apparatus and the end of the decay pipe.

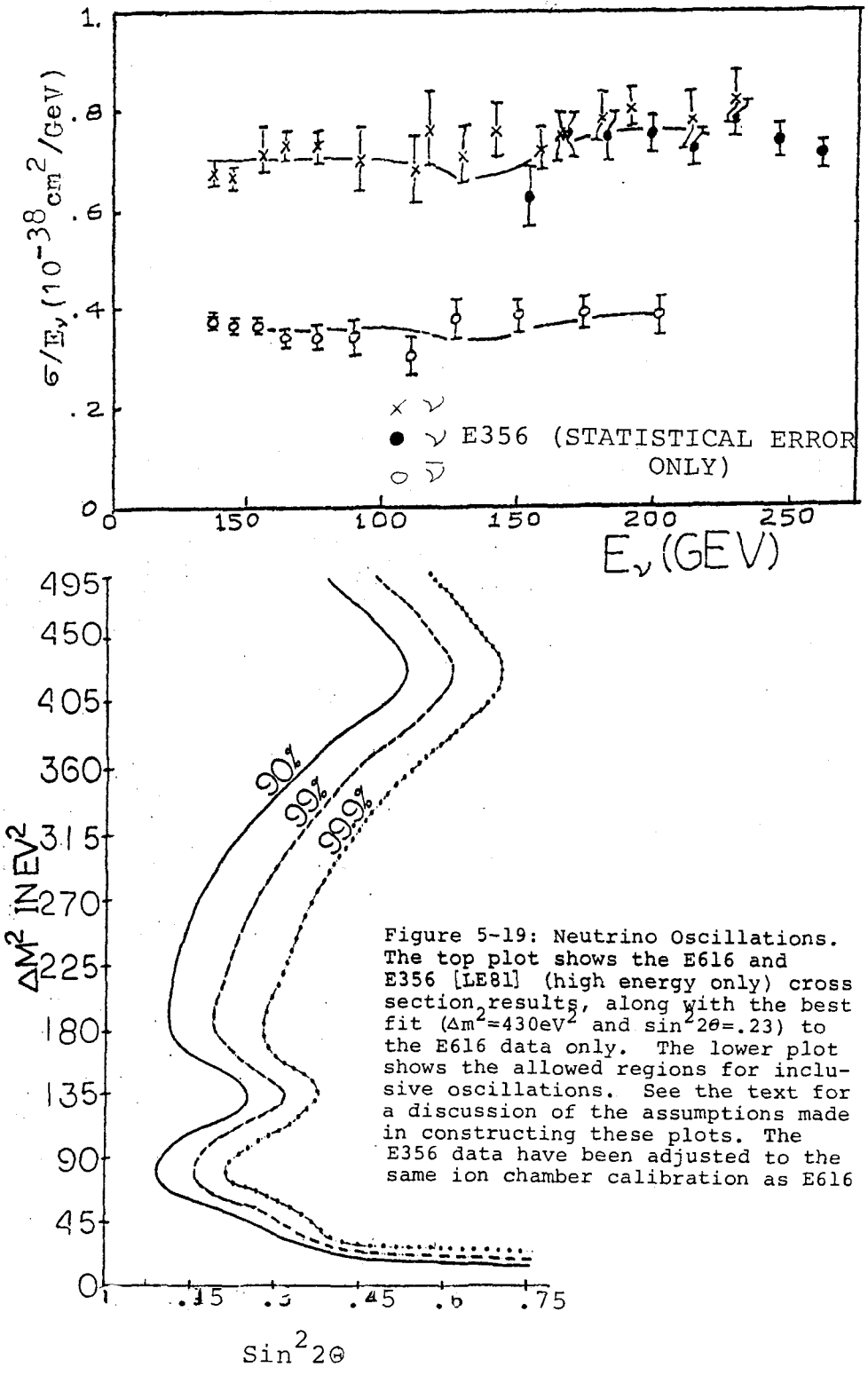

Figure 5-19: Neutrino Oscillations. The top plot shows the E616 and E356 [LE81] (high energy only) cross section results, along with the best fit (Δm^2=430eV^2 and $\sin^2 2\theta$=.23) to the E616 data only. The lower plot shows the allowed regions for inclusive oscillations. See the text for a discussion of the assumptions made in constructing these plots. The E356 data have been adjusted to the same ion chamber calibration as E616

Appendix 1 Evaluation of Systematic Errors

Any experiment is incomplete without a careful evaluation of how well each measurement has been made, in order to determine the overall accuracy of the final result. The neutrino cross section depends on knowledge of the neutrino flux and energy spectrum at the neutrino detector, an event count and the detector tonnage. Each quantity has been measured or, as in the case of neutrino flux and energy spectrum, can be calculated assuming only well understood decay kinematics and the properties of the secondary beam. In order to evaluate the accuracy of each quantity it was possible in several cases to compare multiple measurements of the same quantity done using completely different methods; by looking at the consistency of the independent methods it was possible to estimate a systematic component of the error or to gain confidence that the errors already included in each measurement were sufficient. This multiple measurement proved useful in determining the mean secondary momentum, secondary flux and in a sense was possible for the determination of the secondary beam angular divergence and momentum bite.

The event count depends on triggers and computer reconstruction. The muon trigger and the penetration trigger were constructed using independent electronic modules. Since these two triggers have a large overlap (most events with $E_h > 10$ GeV and $\Theta_\mu < .1$ satisfy both triggers), it was possible to evaluate the efficiency of the two triggers by comparing them. The efficiency of the triggers determined in this way was consistent with 100% to better than .5%, accordingly trigger inefficiencies were not considered to be a significant source of error.

One common element in both triggers was the veto which eliminated events originating upstream of the Lab E apparatus in the earth berm. This introduces some deadtime which is common to both triggers and has to be corrected for.

This deadtime can be measured by counting the number of times a trigger was in coincidence with the veto delayed by slightly more than an event gate width. The number of such coincidences was always under 2% of the muon trigger rate. Comparison of this rate for the penetration, muon triggers and straight through triggers suggests that the accuracy of this method is at the .5% level .

The reconstruction of events did result in some fraction of improperly analyzed events. This can result in both losses and gains. The overall loss or gain of events was probably less significant than the movement of events from the pion decay neutrino category to the kaon variety. Of the events examined, 1.1%±.5% would have been used as muon events but had incorrect momentum fits which resulted in more than a 10GeV error in the muon momentum. Less than a 10GeV error would not be significant since the cross over between pion and kaon decay neutrinos is at about 100GeV and the overlap due to resolution, worse than 10%, is negligible. The worst case crossover as a result of all 1.1% of the misfit events moving from pion to kaon category and vice versa is tabulated in table A1-1 versus energy setting. The error was estimated as one half of the range of this possible error and appears in table A1-1.

The total error on the event count was taken as the sum in quadrature of statistical,.5% for the veto deadtime correction,.5% for event losses, plus the error listed in table A1-1 for each setting and type of neutrino. This error is considered to be a prudent estimate and amounts to at most 50% statistical 50% systematic error and in general the error is dominated by the statistical contribution.

By far the largest uncertainties in the cross section arise from our ignorance of the properties of the secondary beam. In order to measure the cross section we must know the number of pions and kaons that decayed producing neutrinos. The number of pions and kaons is calculated from the

Table A1-1: Limits on Event Crossover Due to Misfits

Energy	Max. Loss	Max. Gain Pi's	Max. Gain Ka's	Error Pi's	Error Ka's
+250	1.1%	.8%	.9%	1.%	1.%
+200	1.1%	.5%	1.4%	.8%	1.3%
+168	1.1%	.4%	1.7%	.8%	1.4%
+140	1.1%	.2%	2.6%	.7%	1.9%
+120	1.1%	.2%	3.5%	.7%	2.3%
-120	1.1%	.1%	8.0%	.6%	4.6%
-140	1.1%	.1%	6.%	.6%	3.6%
-168	1.1%	.2%	5.2%	.7%	3.2%
-200	1.1%	.2%	5.6%	.7%	3.4%
-250	1.1%	.2%	5.4%	.7%	3.3%

product of the total number of secondaries, obtained from one or both of the ion chambers, and the fraction of pions or kaons to the total evaluated with the Cherenkov pressure curves.

The errors on the particle fractions come from uncertainties in corrections applied to the raw curves, and from unknown sources of instrumental error. The error due to corrections was estimated by varying these corrections within reasonable limits and observing the differences induced in the particle fractions.

During the course of the running duplicate pressure curves were taken at each energy. The stability of the particle fractions as a function of run at a given energy provided some indication of the level of instrumental errors. The errors on the particle fractions due to uncertainties in background subtraction, misalignment corrections and the overall error in the particle fractions are listed in table A1-2.

The Cherenkov counter (located 136m. from the end of the train) sees more than just the secondary particles coming out of the train. It also responds to decay products from the ka's and pi's. The decay products (mostly muons)yield a background which in part is indistiguishable from other backgrounds which are subtracted from the raw Cherenkov data. Since the exact amount that has been subtracted is unclear, the particle ratios were computed as a compromise between fully counting the decay products and not counting them at all, and the difference between the compromise and either extreme was considered the level of uncertainty. The particle ratios obtained in this way and the uncertainty is listed in table A1-3.

The total number of secondaries was measured using two ion chambers. The calibration (number of coulombs collected per particle) was done in several different ways and the independent methods afforded a check on each other.

In brief, the methods differed in how the number of particles were counted and what type of beam was used. The beams included the dichromatic secondary beam, 200 Gev. protons brought through the dichromatic train, a meson lab secondary beam and the n5 secondary beam. The devices used to measure particle fluxes were, an R.F. cavity, particle counting with scintillators, foil irradiation, and a beam current transformer. Table A1-4 lists the results of each calibration run along with the momentum and proton content of the beam.

Table A1-2: Errors on Cherenkov Areas

	background subtraction error			misalignment correction error			total error		
energy	pi's	ka's	protons	pi's	ka's	protons	pi's	ka's	protons
+250	1%	5%	3%	-	1.1%	1.2%	1%	5.1%	3.2%
+200	1%	4%	4%	-	1.1%	1.5%	1%	4.3%	4.3%
+168	1%	3%	5%	-	1.1%	2%	1%	3.2%	5.4%
+140	1%	4%	5%	-	1.2%	3.0%	1%	4.2%	5.8%
+120	1%	5%	8%	-	1.4%	4.2%	1%	5.2%	9%
-120	1%	5%	50%	-	1.4%	4.2%	1%	5.2%	50.%
-140	1%	4%	50%	-	1.2%	3%	1%	4.2%	50%
-168	1%	3%	50%	-	1.1%	2%	1%	3.6%	50%
-200	1%	4%	50%	-	1.1%	1.5%	1%	4.1%	50%
-250	1%	5%	-	-	1.1%	-	1%	5.1%	-

The ion chamber response did not depend on the secondary energy, but did depend on what the proton content of the beam was. Some of the ionization produced may come from low energy nuclear fragments resulting from secondary collisions in the ion chamber plates. This part of the ionization will depend on the nuclear cross section of the particles being monitored. Protons would be expected to produce more ionization via this mechanism than mesons, since their cross section is larger. The difference between a pure meson beam and a proton beam was 4.5%. The calibration of the ion chamber after adjusting to zero protons is listed in table A1-4.

Table A1-3: Pion and Kaon fractions

	fraction of total beam		uncertainty due to decays	
energy	pions	kaons	pions	kaons
+120	.5256±.022	.0526±.0034	.6%	.2%
+140	.4176±.015	.0472±.0026	.5%	.4%
+168	.2969±.011	.0371±.0019	.4%	.3%
+200	.1812±.0066	.0251±.0013	.3%	.1%
+250	.0718±.0026	.0118±.0007	.2%	.4%
-120	.876±.015	.0650±.0036	.5%	.1%
-140	.898±.012	.0607±.0028	.4%	.1%
-168	.920±.0098	.0560±.0021	.3%	.2%
-200	.934±.0088	.0434±.002	.2%	.2%
-250	.966±.0059	.0339±.0019	.1%	0%

Table A1-4:
Calibration of Ion Chambers (units=10^{-18} Coulombs/particle)

Response	Zero Protons	Proton Fraction	Energy
M2 secondary beam (particle counting), AVERAGE= 3.42±.05			
3.47±.050	3.42	.29	90GeV
3.45±.050	3.38	.53	140GeV
3.65±.050	3.54	.82	200GeV
3.57±.050	3.33	.97	300GeV
3.38±.050	-	0.00	-90GeV
3.39±.050	-	0.00	-200GeV
Dichromatic Secondary Beam (R.F. Cavity Monitor)			
Positive Settings: AVERAGE= 3.57±.17			
3.61±.17	3.54	.416	120GeV
3.67±.17	3.58	.534	140GeV
3.74±.17	3.62	.667	168GeV
3.72±.17	3.58	.794	200GeV
3.78±.17	3.62	.917	250GeV
3.67±.17	3.63	.250	90GeV
3.60±.17	3.44	1.000	200GeV
Negative Settings: AVERAGE= 3.32±.17			
3.46±.17	-	0.000	-250GeV
3.38±.17	-	0.000	-200GeV
3.31±.17	-	0.000	-168GeV
3.29±.17	-	0.000	-140GeV
3.24±.17	-	0.000	-120GeV
3.22±.17	-	0.000	-90GeV
Protons Through the Dichromatic Train (foil irradiation)			
3.375±.097	3.220	1.000	200GeV
Protons Through the Dichromatic Train (Beam Current Transformer)			
3.45±.22	3.29	1.000	200GeV
N5 Beam (Particle Counting)			
3.57±.17	-	0.000	-275GeV
GLOBAL AVERAGE= 3.40± .05 (adjusted to 0 protons)			

During the running of the experiment stability of the ion chambers was determined by comparing the two ion chambers to each other and to the beam current transformer that monitored the flux of protons on the production target. The monitoring was stable at the 2% level for positives and 5% for negatives. There was also an additional 3% uncertainty in carrying the normalization obtained in the calibration runs over to the negative running(induced by

changes made in the monitors between the negative running and the later positive and calibration runs). In total this amounts to a 2% error on the positive fluxes and a 5.8% error on the negative fluxes. The ion chamber calibration adds an additional 2.5% uncertainty to both positive and negative fluxes.

The Lab E apparatus could take only one trigger per beam spill; the relevant flux was the flux in the decay pipe prior to the first trigger. This "livetime" flux was obtained by taking the output of the ion chambers integrated over the whole spill and multiplying by the fraction of the protons on target prior to the first trigger to the total (as determined by the beam current transformer gated on the experimental livetime). An alternative way to determine the livetime was to count trigger ones throughout the spill and to compare that to the number taken as the first trigger in the spill (trigger one events). The root mean square difference between the two was 1.2% and this value was considered as the error (see table A1-5).

The last source of error came from ignorance of the exact beam parameters that go into the calculation of neutrino flux from secondary flux. The neutrino flux depends on the momentum, the momentum bite and angular divergence of the secondary beam. The dependence on momentum and momentum bite may be estimated by considering an ideal beam which has no angular divergence. The relevant quantity for calculating the slope of the cross section versus energy is the product of flux and energy of the neutrinos passing through an annular slice of the Lab E apparatus. For a collimated monoenergetic beam of secondaries with mass m_0 and decay length $c\tau$ (provided $L_D \ll c\tau$) we have:

Table A1-5:
Comparison of BCT and Trigger 1 Livetime

	livetime fraction	
energy	BCT	Trigger 1
+120	.694	.717
+140	.667	.684
+168	.656	.667
+200	.686	.697
+250	.709	.724
-120	.817	.812
-140	.821	.824
-168	.855	.860
-200	.875	.875
-250	.913	.901

$N_\nu E_\nu \approx \alpha E_\nu^3 \Delta R^2 / p_0$

Where $\alpha = m_0^3 \frac{L_D}{(c\tau L^2(m_0^2 - \mu^2)^2)}$

$\alpha = 7.49 \times 10^{-7} / (in^2 Gev)$ for pions

$\alpha = 5.57 \times 10^{-8} / (in^2 Gev)$ for kaons

R =the distance of the neutrino from beam center at Lab E

L_D=the decay pipe length

L=the average distance from Lab E to the decay point

μ=the muon mass

$$E_\nu \approx \frac{(m_0^2-\mu^2)}{p_0((R/L)^2+(m_0/p_0)^2)}$$

N_ν= the number of neutrinos per secondary

To estimate the sensitivity of this quantity on the momentum and momentum bite of the train we expand in a Taylor series around p_0. We get:

$$N_\nu E_\nu = N_0 E_0 (1+(3E_\nu \frac{((m_0/p_0)^2-(R/L)^2)}{(m_0^2-\mu^2)}-1/p_0)\delta p$$

$$+(6E_\nu^2 \frac{((m_0/p_0)^2-(R/L)^2)^2}{(m_0^2-\mu^2)^2}+3E_\nu \frac{(R/L)^2-2(m_0/p_0)^2}{(p_0(m_0^2-\mu^2))}+1/p_0^2)\sigma_p^2)$$

Where we have integrated over a momentum spectrum and dropped higher than second order terms in the expansion. Figure A1-1 shows the contribution of the first and second order terms versus $\delta p/p_0$ and σ_p/p_0, the fractional momentum shift and dispersion respectively.

The mean momentum of the beam is calculable given that the train elements are all measured precisely and that the production of secondaries is accurately modeled. Since the train elements cannot be accessed after installation, it is better to avoid a detailed calculation which depends on the validity of many parameters that cannot be directly measured. We have done this by using a measurement of the mean momentum (see section 2.4.7), but it should be noted that the results of a "Decay Turtle" calculation never differs by more than 2.5% from the values we used.

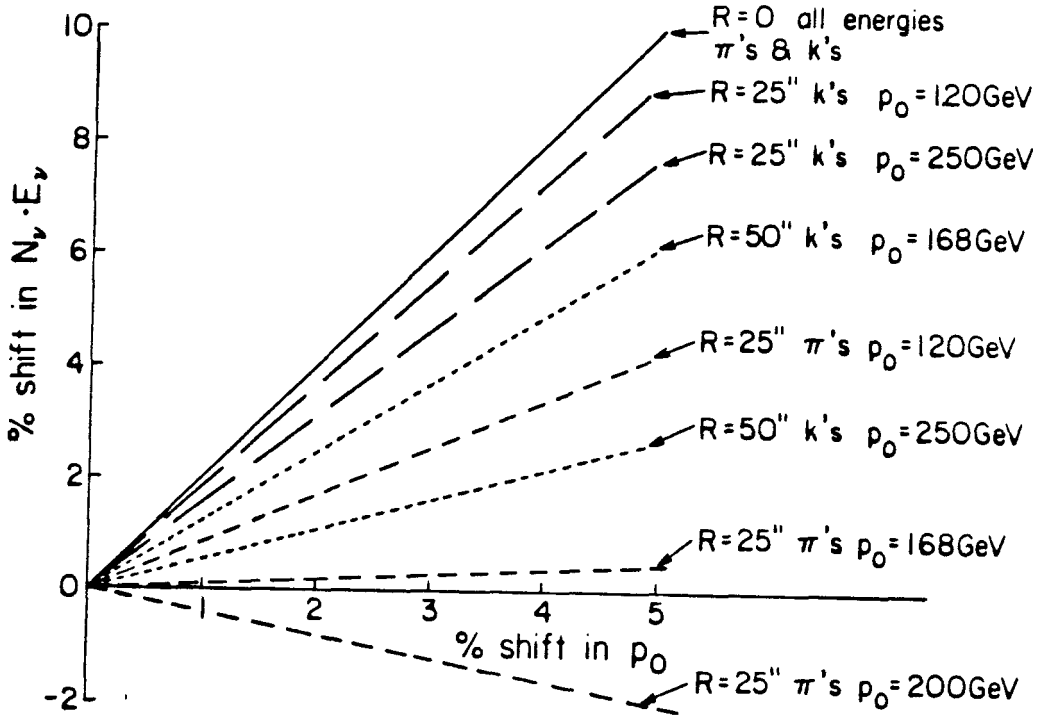

Figure a1-1a: The dependence of the flux times the energy of neutrinos on the momentum of the secondaries.

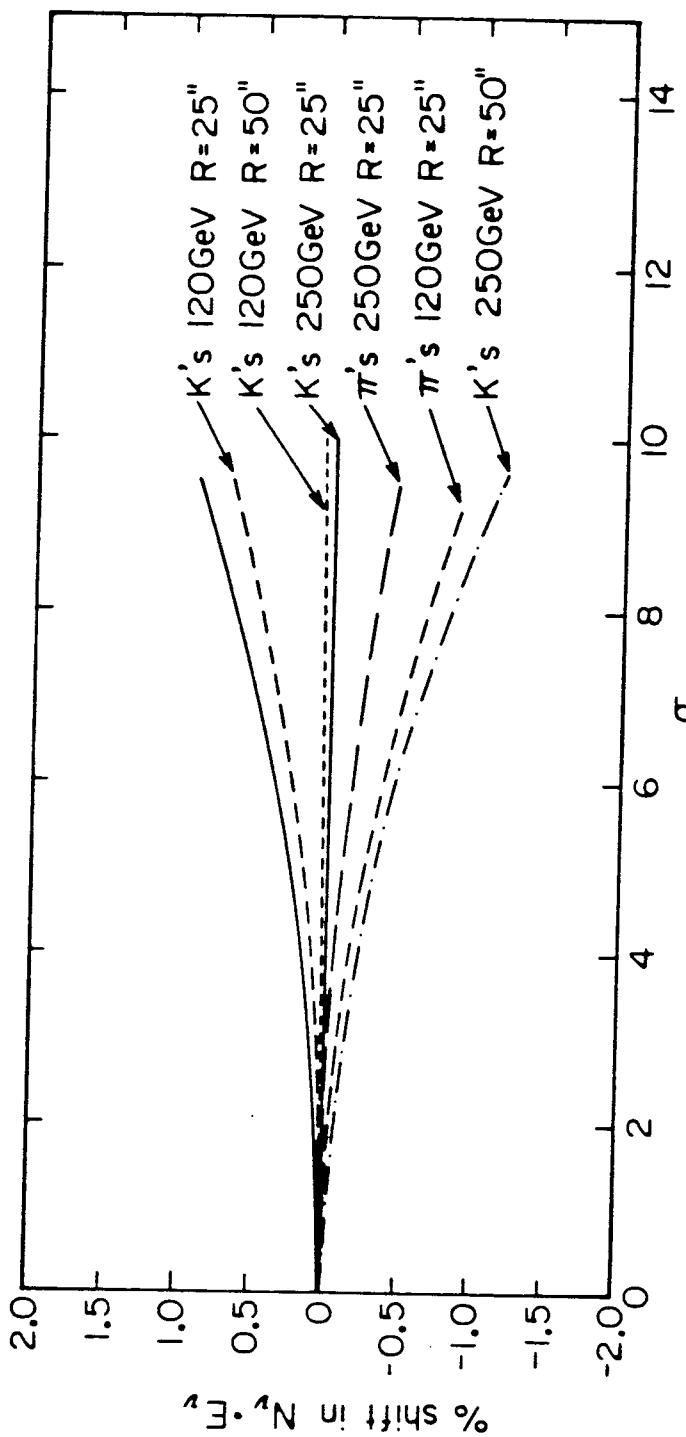

Figure a1-1b: The dependence of the flux times the energy of neutrinos on the momentum bite of the secondary beam.

Two methods have been used to determine the momentum of the secondary beam. The Cherenkov pressure curves act as an approximate momentum transform of the secondaries. The mean pressure of the pion and kaon part of the curve can be used to yield a mean momentum. For an ideal beam (with no angular dispersion) we have:

$$2\kappa\langle P\rangle - \frac{2(\Theta_2^4+(\Theta_1\Theta_2)^2+\Theta_1^4)}{3(\Theta_1^2+\Theta_2^2)} = \langle(m/p)^2\rangle$$

Where <P>=the average pressure of the peak

κ=4.375x10^{-8}±4.x10^{-10}/ *mm.Hg*. for He

$\Theta_1$andΘ_2=limits of the Cherenkov light accepted

The value of the angle term in the above expression would be .774 x10^{-6} for the counter used, however, the angular spread of the secondaries contributes to this quantity and so an effective value was obtained} by using the neutrino data to determine $\langle(m/p)^2\rangle$ for neutrinos from pion decay and this was fit versus the average pressure of the pion peak. The angular term calculated in this way was .764x10^{-6} with an r.m.s. of .05x10^{-6}. The r.m.s. reflects the kind of variation to be expected from the differences in angular dispersion due to production differences and was considered to be the level of uncertainty. Using this fit value and the observed pressure means the predicted shift from nominal of the beam predicted by the pressure averages is listed in table A1-6.

The other method of measuring the mean momentum (not independent in the case of pion neutrinos) is by comparing the total energy observed in interactions at Lab E with the expected total energy. For $R<<Lm_0/p_0$ the neutrino energy is directly proportional to the momentum of the decay meson. Using neutrino events with R<50" for neutrinos from kaon decay and R<10" for those from pion decay, the shift from nominal value of the mean momentum of pi's and ka's is listed in table A1-6. Note that an overall error of 2% was

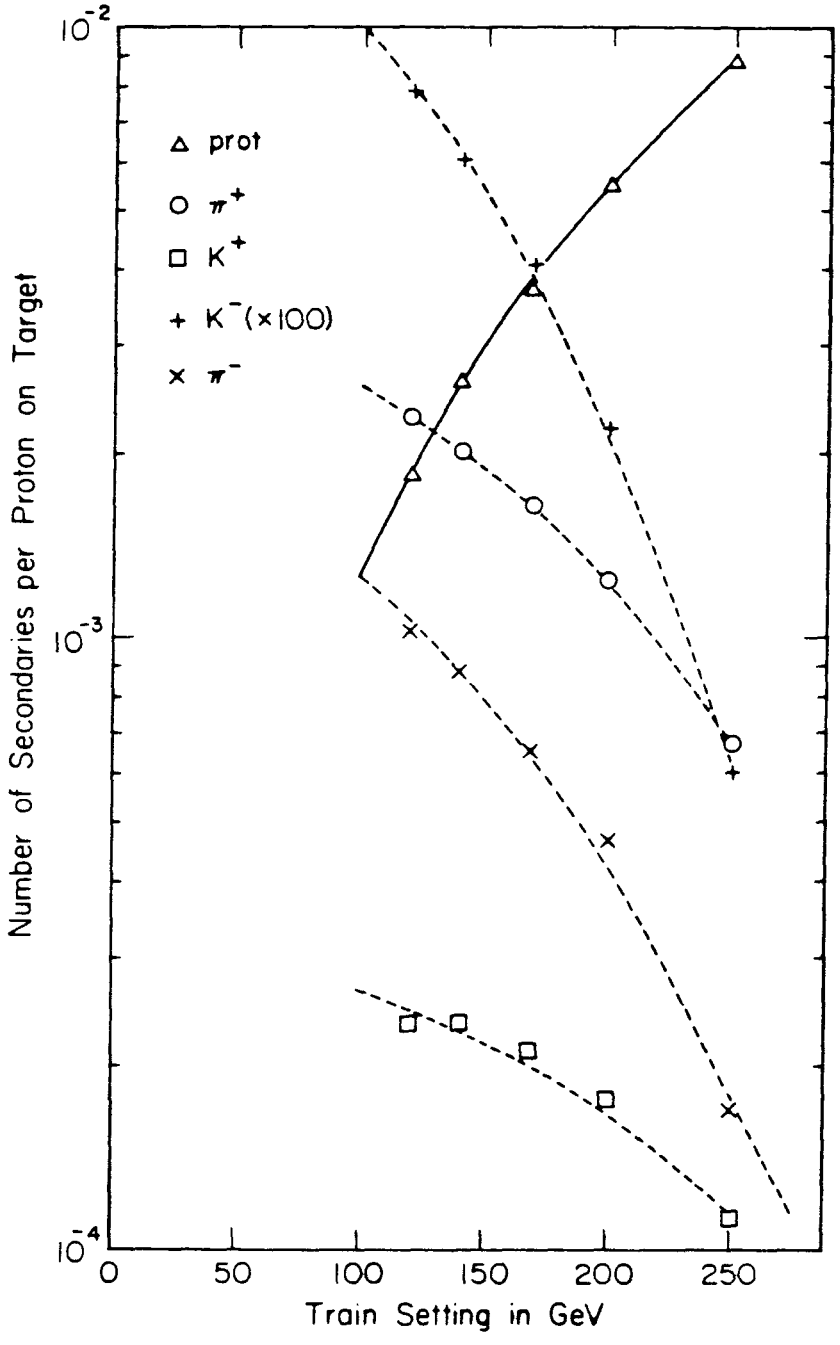

Figure a1-2: The product of transmission and production for the N30 train. The smooth curves are a simple paramaterization (see the text).

placed on the mean energy of the neutrinos measured this way. The neutrino energy required an acceptance correction and relied on the absolute calibration of the hadron energy and the muon momentum. By comparing low y to high y events it was found that this method was only good to about 2%.

Table A1-6: Shift from Nominal Beam Momentum

	Cherenkov Mean Pres.	E_ν		Value Used in M.C.	
energy	kaons	pions	kaons	pions	kaons
+120	1.4±.6	2.5±2.3	4.2±2.1%	-.4%	2%
+140	1.4±.7%	-2.2±2.2%	3.9±2.1%	-.6%	1.6%
+168	1.5±.8%	.3±2.1%	3.1±2.%	-1%	1.1%
+200	.1±1.%	-2.1±2.1%	1.3±2.%	-1.5%	.3%
+250	-1.5±1.%	-2.9±2.1%	-1.8±2.%	-2.5%	-1.2%
-120	-.4±.7%	-1.8±2.8%	-.2±2.3%	-1.3%	-.3%
-140	-1.1±.7%	.3±2.3%	-.4±2.1%	-1.6%	-.8%
-168	-2.2±.8%	-2.9±2.3%	-1±2.1%	-2.2%	-1.6%
-200	-2.2±.8%	-1.9±2.2%	-1.7±2.1%	-3%	-2.7%
-250	-4.2±.9%	-5.1±2.3%	-5.4±2.1%	-4.4%	-4.8%

The shape of the shift in beam energy may be estimated simply from the production dependence on nominal setting. The number of pi's ,ka's and protons passed by the train per unit proton on target is plotted in figure A1-2 versus nominal beam setting. Also plotted is a fit of the form $n(p_{set})=Ae^{-Bp_{set}^2}$; this fit typically agrees to better than 5% with the data. The average secondary momentum was not right on the nominal value for two reasons. Since our

understanding of the train is imperfect there may be uncertainties at the 1-2% level in exactly what the true nominal setting is. There is a difference between the nominal setting and the mean momentum in part because the particles being transported are not produced with a flat production spectrum. The fall or rise in the production spectrum causes the average momentum to differ from the central ray of the train. To estimate this effect we use the above fit.

Let: $G(p,\Omega)$=the production function for production of a particle with momentum p into solid angle Ω at the target

$\varepsilon(Q,\Omega)$=function of $Q=p-p_{set}$ and Ω which tells whether that particle will get through the train($\varepsilon=1$) or not($\varepsilon=0$)

$n(p_{set})$=the number of secondaries per proton on target

then we have

$$n(p_{set})=\int G(p_{set}+Q,\Omega)\varepsilon(Q,\Omega)dQd\Omega$$

$$\frac{dn}{dp_{set}}=\int \frac{\partial G}{\partial p}(p_{set}+Q,\Omega)\varepsilon(Q,\Omega)dQd\Omega$$

provided the momentum bite is small enough

$$G(p,\Omega)\approx G(p_{set},\Omega)+\frac{\partial G(p_{set},\Omega)}{\partial p_{set}}Q$$

$$\frac{dn}{dp_0}\approx\int \frac{\partial G}{\partial p_{set}}(p_{set},\Omega)\varepsilon dQd\Omega$$

$$n(<p>-p_{set})\approx\int QG(p_{set},\Omega)\varepsilon dQd\Omega+\int Q^2\frac{\partial G}{\partial p_{set}}(p_{set},\Omega)\varepsilon dQd\Omega$$

giving

$$\frac{(<p>-p_{set})}{p_{set}}\approx p_{set}(<Q^2>/p_{set}^2)\frac{dln(n)}{dp_{set}}$$

for the N30 train $\frac{<Q^2>}{p_{set}^2}\approx.00884$

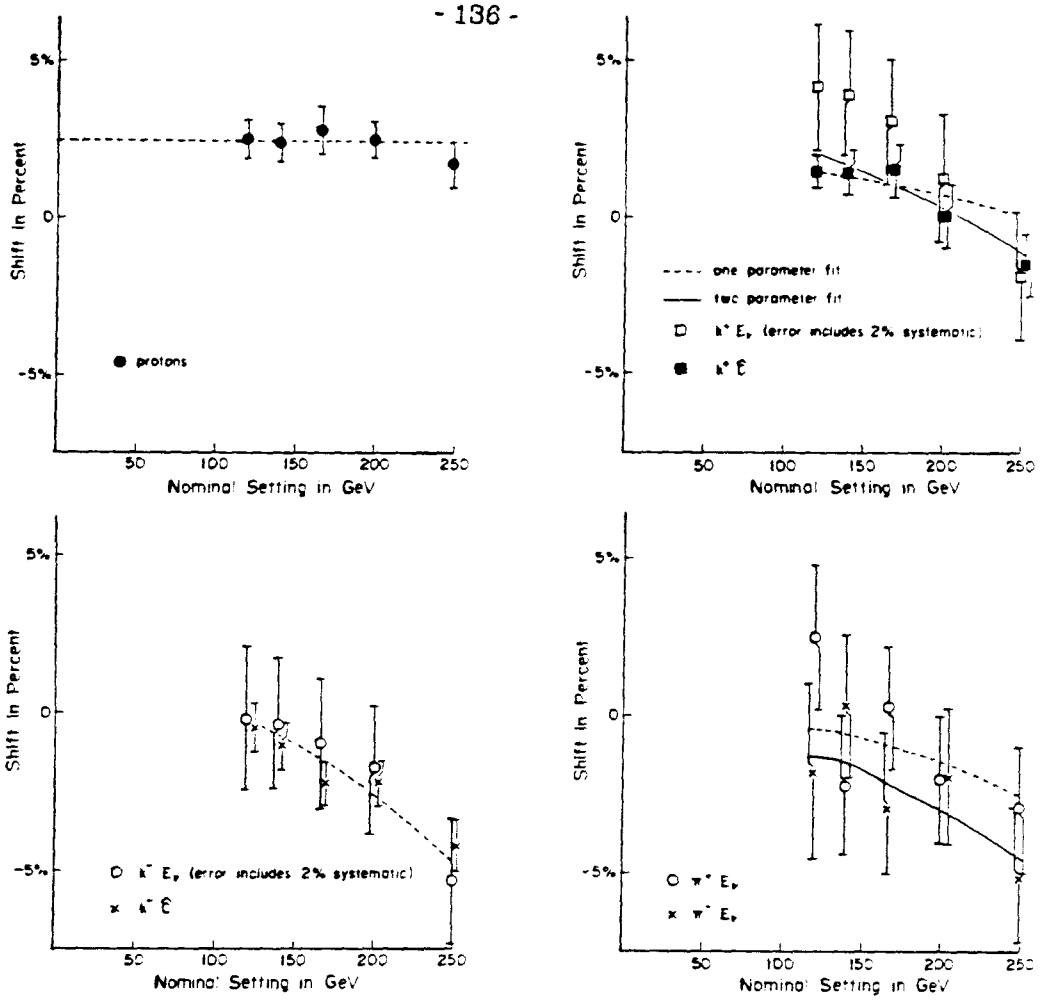

Figure a1-3: The shift from nominal of each particle types momentum. The points labeled E_ν are obtained by observing the total energy of neutrinos emmitted at "small" angles (see the text). The points labeled $\hat{C}$ come from the mean pressure of the Cherenkov peaks. The curves are fits discussed in the text. They were used to smooth the data and yield the shift used in the Monte Carlo flux calculation.

After adjusting the overall shift these forms agree well with both momentum measurements. For positive kaons, however, the 250 Gev. point falls low by 1.5% for both the Cherenkov and neutrino data. Since this method is sensitive to the derivative of the production with respect to p_{set} it may not agree at the end points. Instead of using this form to give the shift a two parameter fit of the form Ap_{set}^2+B was done for positive kaons. The two parameter fit agreed with the one parameter fit to within .5% except at 250 Gev. where they differed by 1%. The final values for the difference from nominal setting are quoted in table A1-4 and plots of the form predicted by production and the measured shifts appear in figure A1-3. The level of accuracy of this procedure was judged to be 2% for pions and 1% for kaons.

The variation of momentum bite of the beam from setting to setting is very small. The Monte Carlo prediction and the Cherenkov curves yield values for the kaons in a range 9.4%±.7%. This range (not an uncertainty) contributes to a variation in flux times energy at the level of .6% at most for this experiment. Because of the smallness of this variation the uncertainty in σ_p was not considered to be a significant source of error.

Finally the angular dispersion of the secondaries must be considered as an important beam parameter. The measurement of the the angular dispersion is crude. In the decay pipe the x and y projections of the beam intensity versus position are sampled by SWICs at two points. A check on the validity of the SWICs as profile monitors was obtained by using a movable scintillator to sample the beam at the expansion port. The agreement between the scintillator and the SWIC in the expansion port was good except for the tails of the distribution. The scintillator went to zero while the SWIC gave a signal for wires far from the beam center. This residual signal was considered to be unrelated to beam particles and only SWIC wires with more than 5% of the peak output were used to insure

that this background was not included in calculating widths.

In order to connect these profiles to an angular dispersion, consider a beam in free flight in the decay pipe. The number of secondaries in a swath along y at fixed x with angle x' determines the corresponding number of particles at a distance L down the decay pipe with position x+Lx'. If we consider the second moment and arrange our coordinate system with z down the average beam direction, we have:

$$\sigma_\theta^2 = \int x'^2 N(x,x')dxdx'$$

$$\sigma_x^2(z=0) = \int x^2 N_{z=0}(x,x')dxdx'$$

$$\sigma_x^2(z=L) = \int x^2 N_{z=L}(x,x')dxdx'$$

$$N_{z=L}(x,x') = N_{z=0}(x-Lx',x')$$

$$\sigma_x^2(z=L) = \int x^2 N_{z=0}(x-Lx',x')dxdx'$$

$$= \int (x+Lx')^2 N_{z=0}(x,x')dxdx' = \sigma_x^2(0) + 2L\int xx' N_{z=0}dxdx' + \sigma_\theta^2$$

If we have three profiles at different z locations it is possible to extract σ_θ^2, by solving the two independent equations for $\sigma_x^2(z=L,L')$ for the unknown integral in the above and for σ_θ^2. An accurate determination of σ_x^2 was only available for two points in the decay pipe. However,the aperture at the end of the train serves to put a limit on the size of the beam at the beginning of the decay pipe. Table A1-7 lists the angular dispersion as calculated by averaging the two extreme assumptions that the beam was uniform or a point at the end of the train. The error listed is that due to the uncertainty in size at the end of the train. The large size of the x aperture leaves a great deal of freedom for variation, but the y view uncertainty is very small. The Monte Carlo used to calculate neutrino flux was adjusted to midway between the SWIC estimates in the y view and the original Monte Carlo prediction and the error was considered to be the difference between the compromise value and the two estimates. For the x view

this was not possible but there was no indication of a systematic difference between Monte Carlo and profiles. The uncertainty in the x view was taken as 25% which is the root mean square deviation of the SWIC estimate from the Monte Carlo.

Table A1-7: Angular Dispersion of the Secondary Beam

energy	Dispersion in mr.(X)		Dispersion in mr.(Y)	
	SWICs	Monte Carlo	SWICs	Monte Carlo
-120	.129±.064	.161	.279±.003	.184
-140	.178±.122	.146	.241±.003	.185
-168	.081±.081	.132	.230±.004	.174
-200	no data	.152	no data	.196
-250	.164±.050	.156	.206±.004	.197

The error introduced by uncertainty in beam properties is summarized in table A1-8 (the error is presented for the cross section computed in radial bins from 0-25" and 25"-50"). The errors in this table are signed quantities showing the difference in the cross section for a plus one change in the beam quantity of the magnitude assessed as the error.

TABLE A1-8a: POSITIVE SETTING ERROR SUMMARY
(errors expressed as fraction of $\frac{\sigma}{E}$)

PION NEUTRINO EVENTS						
P_0 error	σ_{θ_x} error	σ_{θ_y} error	other syst. error	Statistical error	Total error	E_ν
-.030	.016	.033	.045	.021	.050	45.914
-.003	-.004	-.020	.045	.023	.051	34.152
-.028	.017	.005	.043	.018	.047	51.309
.004	-.008	-.002	.043	.022	.048	36.152
-.034	.006	.005	.041	.015	.043	58.644
.013	-.014	-.007	.041	.025	.048	38.388
-.017	.020	.027	.041	.013	.043	66.379
.003	-.029	-.045	.041	.021	.046	40.817
-.018	.017	.011	.042	.012	.044	76.228
.003	-.051	-.022	.042	.024	.049	43.982
KAON NEUTRINO EVENTS						
P_0 error	σ_{θ_x} error	σ_{θ_y} error	Other syst. error	Statistical error	Total error	E_ν
-.021	-.007	-.002	.072	.065	.097	116.924
-.024	-.010	-.039	.072	.051	.088	111.935
-.018	-.007	-.039	.063	.048	.080	135.877
-.030	-.026	-.004	.063	.033	.071	128.704
-.011	-.019	.033	.052	.036	.063	161.824
-.041	-.029	-.014	.052	.024	.058	149.686
-.015	-.008	-.007	.056	.027	.062	187.409
-.017	-.012	-.022	.056	.019	.059	169.355
-.019	.003	.002	.071	.020	.073	224.003
-.011	-.003	-.002	.071	.015	.072	195.376

TABLE A1-8b: NEGATIVE SETTING ERROR SUMMARY
(errors expressed as fraction of $\frac{\sigma}{E}$)

ERROR SUMMARY FOR PION NEUTRINO EVENTS

P_0 error	σ_{θ_x} error	σ_{θ_y} error	Other syst. error	Statistical error	Total error	E_ν
-.027	.009	.005	.066	.033	.074	44.886
-.005	.009	-.010	.066	.033	.074	33.770
-.025	.030	.019	.067	.026	.072	51.297
.001	-.016	-.009	.067	.030	.073	36.218
-.021	.025	.019	.066	.024	.070	57.782
.001	-.032	-.015	.066	.031	.073	38.249
-.016	.035	.049	.065	.022	.069	65.443
.006	-.045	-.056	.065	.034	.073	41.040
-.016	.035	.020	.065	.025	.070	74.751
-.010	-.110	-.052	.065	.052	.083	43.719

ERROR SUMMARY FOR KAON NEUTRINO EVENTS

P_0 error	σ_{θ_x} error	σ_{θ_y} error	Other syst. error	Statistical error	Total error	E_ν
-.010	-.001	-.066	.094	.130	.161	113.632
-.017	-.028	-.025	.094	.084	.126	109.320
-.015	-.011	-.051	.087	.094	.128	130.721
-.024	-.011	-.009	.087	.061	.106	124.047
-.015	-.029	-.029	.081	.084	.117	155.649
-.016	.018	-.000	.081	.054	.097	144.731
-.011	.016	-.013	.085	.083	.118	182.576
-.013	.006	.015	.085	.053	.100	165.875
-.005	.023	.015	.088	.085	.122	218.363
-.005	-.015	.005	.088	.063	.108	192.047

(THIS PAGE IS BLANK, DUE TO ERROR IN PAGINATION)

List of References

AB80: L. Abbott, et. al., Phys. Rev. D22 no. 3, 580 (1980).

AB81: H. Abramowicz et. al."A Measurement of the Ratio of Longitudinal and Transverse Structure Functions in Neutrino Interactions between 30 and 200 GeV.", CERN-EP/81-50, CERN (1981).

AL80: D. Allasia et. al., 20th Int. Conf. on High Energy Physics, Madison (1980).

AL77: G. Altarelli and G. Parisi, Nuc. Phys. B126, 298 (1977).

AR80: N. Armenise et. al. "Search for Neutrino Oscillation in 'Gargamelle' at SPS" CERN/EP 80-226 (1980).

AS78: A. Astratyan et. al. Phys. Lett. 105B,315 (1978).

AT80: H. Atherton et. al. "Precise Measurements of Particle Production by 400 GeV/c Protons on Beryllium Targets", CERN 80-07, CERN (1980).

AU74a: J. Aubert et. al. Phys. Rev. Lett. Vol. 33,1404 (1974).

AU74b: J. Augustin et. al. Phys. Rev. Lett. Vol. 33,1406 (1974).

AU81: J. Aubert et. al. "Measurement of the Nucleon Structure Function F_2 in Muon-Iron Interactions at 120, 250 and 280 GeV.", CERN-EP/ 81-85, CERN (1981).

BA75a: B. Barish et. al., Phys. Rev. Lett. Vol. 34, 538 (1975).

BA75b: B. Barish et. al., Phys. Rev. Lett. Vol. 35, 1316 (1975).

BA77a: B. Barish et. al., Phys. Rev. Lett. Vol. 36, 939 (1976). BA77b: B. Barish et. al., Phys. Rev. Lett. Vol. 38, 577 (1977).

BA77b: B. Barish et. al., Phys. Rev. Lett. Vol. 39, 981 (1977).

BA77c: B. Barish et. al., Phys. Rev. Lett. Vol. 39, 1595 (1977).

BA77d: B. Barish et. al., Phys. Rev. Lett. Vol. 39, 741 (1977).

BA78a: B. Barish et. al., Phys. Rev. Lett. Vol. 40, 1414 (1978).

BA78b: B. C. Barish et. al., IEEE Transactions on Nuclear Science, NS-25, 532 (1978).

BA81: B. Barish et. al. Phys Rev. Lett., Vol. 46 no. 24, 1555 (1981).

BE74: A. Benvenuti et. al. Phys. Rev. Lett. Vol. 32, 800 (1974).

BO79: A. Bodek et. al., Phys. Rev. D, Vol. 20, no. 7, 1471 (1979).

BO77: P. Bosetti et. al., Phys. Lett. 70B, 273 (1977).

BU78: A. Buras and K. Gaemers Nuc. Phys. B132, 249 (1978).

CL76: D. Cline et. al., Phys. Rev. Lett. Vol. 37, 252 (1976).

DE79a: J. de Groot et. al., Phys. Lett. 82B, 456 (1979).

DE79b: J. de Groot et. al., Particles and Fields 1, 143 (1979).

DE79c: A. de Rujula et. al. Nuc. Physics B154, 394 (1979).

ED76: D. Edwards and F. Sciulli "A Second Generation Narrow Band Neutrino Beam" TM-660, Fermi National Laboratory (1976).

ED81: B. Edwards and T. Gottschalk "Implications of Mass-Dependent Renormalization Group Parameters for Conventional QCD Phenomenology", CALT-68- 832, Caltech (1981).

EI81: F. Eisele, Proceedings of Neutrino '81, ed. by R. Cence, E. Ma, A. Roberts (Maui,Hawaii) I:279.

FE34: E. Fermi, Z. Phys. 88, 161 (1934).

FE58: R. Feynman and M. Gell-Mann, Phys. Rev. 109, 193 (1958).

FI78: R. Field "Applications of Quantum Chromodynamics" CALT-68-696 Caltech (1978).

FI81: H. Fisk "Production of Charm and New Particles in Neutrino-Nucleon Interactions" Conf-81/73-Exp, Fermi National Laboratory (1981).

FR81: P. Fritze et. al.,Proceedings of Neutrino '81, ed by R.J.Cence, E.Ma, A. Roberts (Maui,Hawaii)I:344.

GL70: S. Glashow, J. Iliopoulos and L. Maiani, Phys. Rev. D2, 1285 (1970).

GO79: B. Gordon et. al., Phys. Rev. D, Vol. 20, no. 11, 2645 (1979).

GR81: H. Grassler et. al. "Inclusive Neutral Strange Particle Production in νp Interactions", CERN/EP 81-56, CERN (1981).

HA73: F. Hasert et. al., Phys. Lett. 46B, 138 (1973).

HI81: D. Hitlin "Weak Decays of Strange and Heavy Quarks" Calt 68-814, Caltech (1981).

JO80: M. Jonker et. al., CERN EP/80-215, (1981).

JO81a: M. Jonker et. al. "Experimental Study of Opposite-sign and Same-sign Dimuon Events Production Wide-band Neutrino and Antineutrino Beams" EP/81- 95, CERN (1981).

JO81b: M. Jonker et. al. Phys. Lett. Vol. 102B, no. 1, 67 (1981).

KA81: B. Kayser "On the Quantum Mechanics of Neutrino Oscillation" SLAC-PUB-2685 (1981).

LE56: T. Lee and C. Yang, Phys. Rev. 104, 254 (1959).

LE77: W. Lee et. al., Phys. Rev. Lett. 38, 202 (1977).

LE81: J. Lee. "Measurement of ν N Charged Current Cross Sections from E_ν=25*GeV.* to E_ν=260*GeV.*" Ph. D. Thesis, Caltech (1981).

LE79: J. Leveille, Nuc. Physics B147, 147 (1979).

LI73: J. Litt and R. Meunier, Ann. Rev. of Nuc. Sci., V23, 1 (1973).

LU80: V. Lubimov et. al., Phys. Lett. 94B, 266 (1980).

ME78: F. Merritt et. al., Phys. Rev. D17, 2199 (1978).

MO81: J. Morfin et. al., Phys. Lett. 104B, 235 (1981).

OL81: S. Olsen, Physics in Collision: High Energy ee/ep/pp Interactions, conf. Blacksburg, Va. (1981).

PE64: V. Peterson, "A Monochromatic Neutrino Beam from a High Intensity 200BeV. Proton Synchrotron" LRL Report UCID-10028 (1964).

PH79: R. Phillips, Nuc. Physics B153, 475 (1979).

RE59: F. Reines and C. Cowan, Phys. Rev. 113, 273 (1959).

RE80: F. Reines, H. Sobel, E. Pasierb, Phys. Lett. 45, 1307 (1980).

SC70: F. Sciulli et. al."Neutrino Physics at Very High Energies" Fermilab Proposal 21, FNAL (1970).

SI81a: D. Silverman "Indications of Neutrino Oscillations from an Analysis of Reactor Experiments Performed at Different Distances" UCI Technical Report No. 81-35 (1981).

SI81b: D. Silverman and A. Soni "Neutrino Oscillations: A Review" UCLA/81/TEP/25 (1981).

WO78: J. Wotschack "Study of Current Reactions in Inclusive Deep Inelastic Neutrino Nucleon Interractions in the Energy Range 30-200 GeV." Ph. D. Thesis, Institut für Hochenergiephysik der Universität, Heidelberg, Germany (1978).

WE67: S. Weinberg, Phys. Rev. Lett. Vol. 19, 1264 (1967).

WU57: C. S. Wu et. al., Phys. Rev. 105, 1413 (1957).